# THE NANOSTRUCTURED SILICON FROM RICE HUSKS FOR HIGH PERFORMANCE Li-ION BATTERY ANODES: SYNTHESIS, CHARACTERIZATION AND ELECTROCHEMICAL PROPERTIES

SIGEI KIPKIRUI ENOCK, B.Ed (Sci)

REG. NO: I56/22808/2012

**A Thesis Submitted in Partial Fulfillment of the Requirements for the Award of the Degree of Master of Science (Chemistry) in the School of Pure and Applied Sciences of Kenyatta University**

**NOVEMBER, 2018**

## DECLARATION

This thesis is my original work and has not been presented for a degree in any other University or for any other award.

**Sigei Kipkirui Enock**

**Reg. No: I56/22808/2012**

Signature:…….. Date…….

We confirm that the work reported in this thesis was carried out by the candidate under our supervision.

**Dr. Eric Masika**

**Chemistry Department**

**Kenyatta University**

Signature**: …….....**Date**: …….....**

**Dr. Dickson M. Andala**

**Department of Physical Sciences**

**Multimedia University of Kenya**

Signature**: …….....**Date**: …….....**

## DEDICATION

This work is a special dedication to my dad Simion K. Malel, mum Mary Malel, my late grandmother Rusi C. Marisin, my brothers and sisters and all those who encouraged me to pursue this study to the end. You are God's gift to me. Without you, I could not have achieved this award.

## ACKNOWLEDGEMENTS

I recognize and appreciate the collective and individual hard work of my supervisors, Dr. Dickson M. Andala and Dr. Eric Masika in providing thorough academic guidance and support to this work. I am exceedingly thankful to Dr. Andala for his kind, consistent and constant educative guidance throughout my research and also grateful for the support he provided in the shipment of some chemicals and reagents from Durban, South Africa and air lifting of samples for further analysis in Binghamton University, NY, USA. I will also not forget Dr. Masika for his great input in enlightening me on correct and acceptable mode and format of thesis-writing as stipulated by the Kenyatta University as well as scrutinizing each and every piece in this work and giving appropriate directions as much as was necessary.

I sincerely want to thank Dr Fredrick Omenya, Binghamton University, NY, USA for assisting in carrying out electrochemical tests on the fabricated battery anodes. Many thanks to the officer in charge of Materials Testing and Research Division, State Department of Infrastructure, Ministry of Transport and Infrastructure, Republic of Kenya, for allowing me to carry out part of my study at their central laboratories. I'm also grateful to Kenyatta University Chemistry Department staff and laboratory technicians for their support during my research. Many regards to Mr. Oloo Christianos of Fine Arts for assisting me in the initial incineration of rice husks. My fellow colleague in the research field, Mr. John Hena who contributed a lot in sharing resources and research materials, I thank him very much. I wish to express my heartfelt gratitude to my dad Simion K Malel for his visionary guidance, advice and financial support to this study.

May God bless all those who made this masters course a success.

# TABLE OF CONTENTS

## LIST OF ABBREVIATIONS AND ACRONYMS

| | |
|---|---|
| b.d | Below detection limit |
| BSE | Backscattered electrons |
| CE | Coulombic Efficiency |
| CRH | Carbonised rice husks |
| CV | Cyclic Voltammetry |
| DTGS | Deuterated triglycine sulfate detector |
| EC | Ethylene Carbonate |
| EDX | Energy-dispersive x-ray fluorescence |
| FTIR | Fourier transform infrared spectroscopy |
| ICDD | International Center for Diffraction Data |
| ICL | Irreversible Capacity Loss |
| IE | Impacted Electrons |
| JCPDS | Joint Committee on Powder Diffraction Standards |
| LIB | Lithium ion battery technology |
| LRHA | Leached rice husk ash |
| MRR | Magnesiothermic Reduction Reaction |
| NMP | N-Methyl-2-Pyrrolidinone |
| PTRH | Pre-treated rice husks |
| PTRHA | Pre-treated rice husks ash |
| PVDF | Polyvinylidene Fluoride |
| RH | Rice husks |
| RRH | Raw rice husks |
| RRHA | Raw rice husks ash |
| SE | Secondary Electrons |
| SEI | Solid Electrolyte Interface |
| SEM | Scanning Electron Microscope |
| SiNPs | Silicon nanoparticles |
| VC | Vinylene Carbonate |
| WDX | Wavelength-dispersive spectrometers |
| WDXRF | Wavelength dispersive X- Ray Fluorescence |
| WRHA | White rice husks ash |
| XRD | X-Ray Diffraction |
| XRF | X- Ray Fluorescence |

## LIST OF TABLES

## LIST OF FIGURES

## ABSTRACT

Nanostructured silicon has attracted considerable attention as a promising anode material for next generation Lithium-ion batteries for applications in portable electronic devices and hybrid electric vehicles. This interest is mainly due to its large theoretical specific charge capacity of 4,200 mAh $g^{-1}$ that is ten times more than the theoretical specific charge capacity of conventional graphite anodes. This work exploits an alternative method of fabricating pure silicon nanoparticles (SiNPs) from rice husks (RHs), an abundant agricultural waste, produced at a rate of approximately $1.2 \times 10^8$ tons per year. The methods uses acid pre-treatment and subsequent combustion of RHs, followed by additional acid leaching of the rice husks ash obtained. To synthesize SiNPs, heat scavenger assisted magnesiothermic reduction of the rice husks originated silica was performed. The silica from rice husks (RHs) and the synthesized SiNPs were characterized by energy-dispersive X-ray (EDX) spectroscopy and FTIR spectroscopy, the morphology was determined using Scanning Electron Microscopy (SEM), while particle size and structure were probed by X-Ray Diffraction (XRD). Acid pre-treatment of RHs with 3M HCl for 12 hours followed by combustion at 600 $^oC$ for 5 hours yielded 22.50% ash of which 98.520 (±0.457) % was amorphous silica. Further acid-leaching of the silica with 2M HCl for 6 hours substantially decreased the level of metallic impurities present to achieve silica of high purity of approximately 99.046 (±0.451) %. Magnesiothermic reduction of this silica yielded SiNPs of high purity of approximately 98.794 (±0.335) % from EDX analysis. The recovered SiNPs used in fabricating Li-ion battery anodes in this study were highly crystalline with their XRD pattern readily indexed to that of pure silicon (JCPDS No. 27-1402). The crystallite size of 10 to 100 nm and porous nature of the recovered SiNPs exhibited superior electrochemical performance over commercially available graphite as Li-ion battery anodes, delivering a high reversible capacity of 2,732 mA $hg^{-1}$ which is seven times greater than the theoretical capacity of graphite anodes (372 mA $hg^{-1}$), with a high coulombic efficiency in first cycle and a long cycle life (97.20 % capacity retention over 16 cycles). Thus, the results obtained indicate that the prepared nanostructured silicon electrode is a promising anode material for high performance lithium-ion battery anode.

# CHAPTER ONE

# INTRODUCTION

## 1.1 Background Information

Rechargeable lithium ion batteries are critical to today's information-rich and mobile society (Teki *et al*., 2009). Currently they are one of the most popular types of battery used in portable electronic devices because of their flexible design and high energy density (Bruce *et al*., 2008). Despite their increasing use at the present time, there is great continued commercial interest in developing new and improved electrode materials for use in lithium ion batteries that would dramatically lead to higher energy capacity and longer cycle life (Teki *et al*., 2009).

Silicon is one of the most promising anode materials because it has the highest known theoretical specific charge capacity of 4,200 mAh $g^{-1}$and is the second most abundant element on earth (Teki *et al*., 2009). However, silicon anodes have limited applications because of the large volume change associated with lithium insertion and extraction (McDowell *et al*., 2013). This causes cracking and pulverization of the anode, leading to gradual loss of electrical contact and eventual fading of capacity (Teki *et al*., 2009). This challenge can potentially be overcomed by using silicon nanostructures that can impart facile strain relaxation thus, preventing electrode pulverization, maintain essential electrical contact and have more benefits of short lithium diffusion distances and increased mass transport (Szczech and Jin, 2011). Silicon nanostructures are also advantageous for a number of reasons, which include their ability to accommodate lithiation-induced strain without fracturing in addition to having a good cycle rate ability (McDowell *et al*., 2013).

The existing methods of producing SiNPs are complex, energy-intensive and costly. (Chen *et al*., 2010). These methods include vapor-phase reaction, sol-gel and thermal decomposition technique (Liu *et al*., 2013). However, their high cost of preparation has generally limited their wide application (Chen *et al*., 2010; Liu *et al*., 2013). Thus, alternative methods of fabrication are needed to produce cheap Si nanoparticles.

Many agricultural products and by-products such as palm oil, sugarcane bagasse, rice husk ash, wheat straw ash or wheat husks ash are considered potential raw materials for preparing high-value products (Shaikh and Shaikh, 2013). In most plant species and in particular those belonging to the Gramineae family, aqueous silicic acid, $Si(OH)_4$, is transported along the transpiration stream in the plant, where polymerization usually occurs as a result of the increased concentration of silicic acid due to transpiration (Chen *et al*., 2010). At the end of polymerization, silicon is thus deposited in cells and intercellular spaces also known as phytoliths (Chen *et al*., 2010). The phytoliths can thus be used as a cheap silica resource to prepare silicon nanoparticles (Chen *et al*., 2010).

Many investigations have shown that pure amorphous silica can be prepared from cheap rice husks, an agricultural byproduct whose major constituent are organic material and hydrated silicon (Chen *et al*., 2010). The use of rice husks has the benefit of producing valuable silica and also reducing disposal and pollution problems (Chen *et al*., 2010). For every five tonnes of rice harvested, one tonne of husks is produced, amounting to approximately $1.2 \times 10^8$ tonnes of rice husks per year across the globe (Liu *et al*., 2013). Thus, developing uses for this waste resource is in accordance with the global paradigm shift towards sustainable development (Liu *et al*.,

2013). When rice husks are incinerated, they generates rice husks ash of between 17 % to 20 % of which about 87 % to 93 % is silica together with other metallic oxide impurities depending on the source of the rice husks (Ugheoke and Mamat, 2012). In this study, amorphous silica extracted from the rice husks by controlled combustion and acid treatment was subjected to heat scavenger assisted magnesiothermic reduction to synthesize silicon nanoparticles, unlike the metallurgical-grade silicon which is made up of micron-sized crystal particles because of the melting of silicon during the carbothermic reduction process involving high temperatures (over 2000 $^{o}$C) which is way above 1410 $^{o}$C, the melting point of silicon. The synthesized silicon nanoparticles played a big role in enhancing the performance of lithium-ion batteries.

**1.2 Problem Statement and Justification**

The inevitable depletion of non-renewable sources of energy such as fossil fuels and the accompanying environmental issues, such as carbon (iv) oxide emissions which is a green house gas, has lead to greater focus on alternative environmentally green energy resources. These include solar energy, hydroelectric power and wind energy; however, most of them are basically periodic or intermittent. Electrochemical energy storage devices, such as batteries, are essential to solve this problem, since they can efficiently store electrical energy in chemicals and release it on demand.

Currently, lithium ion battery technology presents the highest energy density among all the rechargeable battery technologies and has dominated the market for portable electronic devices for decades (Teki *et al*., 2009). The main challenge facing commercial lithium-ion batteries is their insufficient capacity hence leading to a need for frequent charging. The development of new

and improved electrode materials capable of delivering higher energy density is thus of significant interest.

Silicon is one of the most promising materials for high performance lithium-ion battery anodes because it has the highest known theoretical specific charge capacity of 4200 mAh $g^{-1}$ and also is the second most abundant element on earth (Teki *et al*., 2009). Silicon anodes however have limited applications because of the large volume changes associated with the lithium insertion and extraction which causes cracking and pulverization of the anode (Teki *et al*., 2009). This leads to a gradual loss of electrical contact and eventual fading of capacity (Teki *et al*., 2009).

However, the application of silicon as an anode material in commercially available lithium-ion batteries has been limited by mechanical degradation and capacity decay that have typically prevented good cycling performance resulting in electrode failure (Wang and Kumta, 2010), (Wu and Cui, 2012) and (McDowell *et al*., 2013). Recent studies have shown that the reduction of the size of silicon to nanoscale in at least one dimension results in effective accommodation of the strain and can even prevent fracture of the electrode (Liu *et al*., 2013).

While many guidelines for fabricating high-performance nanostructured silicon anodes have been established, the existing methods for producing silicon nanoparticles (SiNPs) are still limited, complex, energy intensive and costly (Liu *et al*., 2013). Alternative methods are thus needed to produce SiNPs for fabrication of Li-ion battery anodes with comparable cost and scalability to that of graphite anodes. Rice husks, an abundant agricultural byproduct whose major constituents

are organic material and hydrated silicon, has the benefit of producing economically valuable, high grade and widely applicable SiNPs in addition to reducing disposal and pollution problems.

### 1.3 Hypotheses of the Study

i. There is no significant difference in structure and morphology between silicon nanoparticles derived from rice husks and commercially available metallurgical-grade silicon.

ii. There is no significant difference in the specific charge capacity of nanostructured silicon anodes derived from rice husks and commercially available graphite anodes.

### 1.4 Objectives

#### 1.4.1 General Objective

To synthesize and characterize silicon nanoparticles from rice husks in terms of morphology, physical and electrochemical properties to determine its suitability for high performance Li-ion battery anodes.

#### 1.4.2 Specific Objectives

i. To synthesize silicon nanoparticles from rice husks by combustion, heat scavenger assisted magnesiothermic reduction and acid leaching.

ii. To determine the morphology, elemental purity and structure of silicon nanoparticles derived from rice husks using SEM, EDX, FTIR and XRD.

iii. To quantify the specific charge capacity of nanostructured silicon anodes.

### 1.5 Significance and Anticipated Output

The study is geared towards providing documented information on the amounts of elemental silicon in rice husks available in Mwea region, Kenya and its suitability for high performance lithium-ion battery anodes. The findings from the study will also be a contribution to the efforts of large scale exploitation of valuable, low cost and functional silicon nanoparticles derived from agricultural byproducts through simple and energy efficient methods. The results of this work are also useful for scientists pursuing new synthetic routes for obtaining valuable and widely applicable silicon nanoparticles. This study is also pivotal in reducing disposal and pollution problems caused by continued accumulation of rice husks.

### 1.6 Scope and Limitations of the Study

The study analyzed the suitability of silicon nanoparticles derived from rice husks for use in high performance lithium-ion battery anodes. The levels of the silica and silicon nanoparticles derived from rice husks are influenced by a number of factors including farm practices and growing climatic conditions, which are however, not considered during the study. The stems and other portions of rice may contain some levels of silica and silicon nanoparticles, however, such were not accounted for in this study. The presence of other metallic impurities in silica during magnesiothermic reduction and chemistry of these elements may also have significant effect on the purity of silicon nanoparticles obtained, this was also not considered.

# CHAPTER TWO

# LITERATURE REVIEW

## 2.1 Lithium Ion Battery Technology

Lithium ion batteries are attractive energy storage devices with high gravimetric and volumetric capacity and the capability to deliver high rates of power (Szczech and Jin, 2011). Rechargeable lithium ion batteries have revolutionized portable electronic devices (Chan *et al*., 2008). They have become the dominant power source for mobile phones, laptops and digital cameras because of their superior energy density ( i.e the capability to store 2-3 times the energy per unit weight and volume compared with conventional rechargeable batteries) (Bruce *et al*., 2008). They are the technology of choice for future hybrid electric vehicles, which are essential to the reduction of carbon (iv) oxide emissions arising from transportation (Bruce *et al*., 2008).

Lithium-based rechargeable batteries were proposed first in the early 1960's and since then this battery technology has gone through several transformations (Teki *et al*., 2009). Initially, metallic lithium was used as the anode material but it posed serious safety hazards due to the dendritic lithium growth during cycling (Figure 2.1) *(*Teki *et al*., 2009). The dendritic growth of lithium metal during cycling can penetrate through the polymer separator to cause a short circuit between the negative and positive electrodes, which can initiate exothermic reactions between the electrodes and the highly flammable organic electrolyte (Wu *et al*., 2014). The excess heat released during these reactions quite often induces fire and even explosions (Chen, 2013; Wong *et al*., 2014; Wu *et al*., 2014).

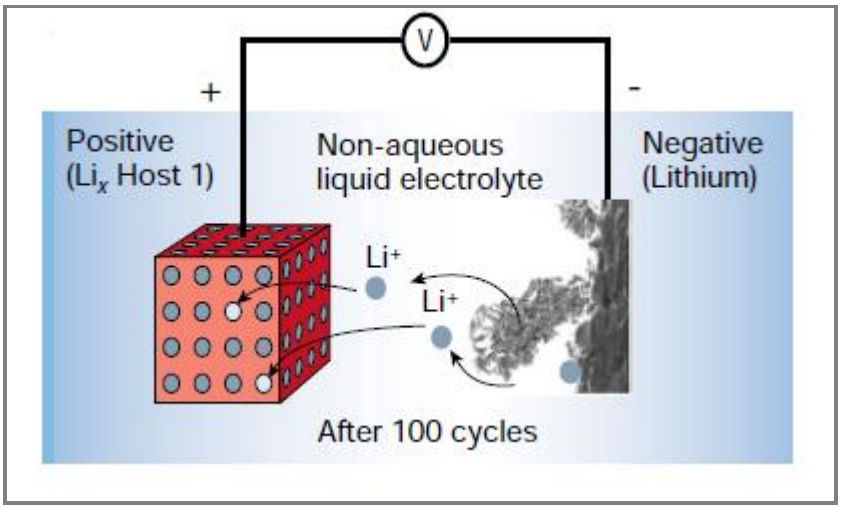


**Figure 2.1:** Rechargeable Li-metal battery; the image of the dendrite growth at the Li surface (Tarascon and Armand, 2001).

In the early 1990's, carbonaceous material was discovered as a highly reversible and low voltage lithium-ion intercalation and deintercalation anode, as it possesses unique properties (Chen, 2013). Combining safety features of these carbon anode and the high voltage $LiCoO_2$ cathode, the first lithium ion battery ($C/LiCoO_2$ cell) was commercialized in 1991, and currently dominates the market for portable electronic devices ( Teki *et al*., 2009; Chen, 2013). Lithium ion batteries technology has a higher energy density than most other types of rechargeable battery technologies because lithium is one of the most electropositive elements (-3.04 V versus standard hydrogen electrode) as well as the lightest electrochemically active metal (Teki *et al*., 2009). Thus for their weight or size they can store more energy than other rechargeable battery technologies (Teki *et al*., 2009).

In comparison to other well known rechargeable batteries, lithium-ion operates at a higher voltage, typically about 3.7 V for lithium-ion versus 1.2 V for nickel-metal hydride (NiMH) or nickel-cadmium (NiCd) (Teki *et al*., 2009). Moreover, when compared with other types of

rechargeable battery technologies, lithium-ion has a lower self-discharge rate (Teki *et al*., 2009). The comparison of the rechargeable battery technologies commercially available as a function of volumetric and specific energy densities is presented in figure 2.2; the arrows shown indicate the direction of development to reduce battery size and weight (Landi *et al*., 2009).

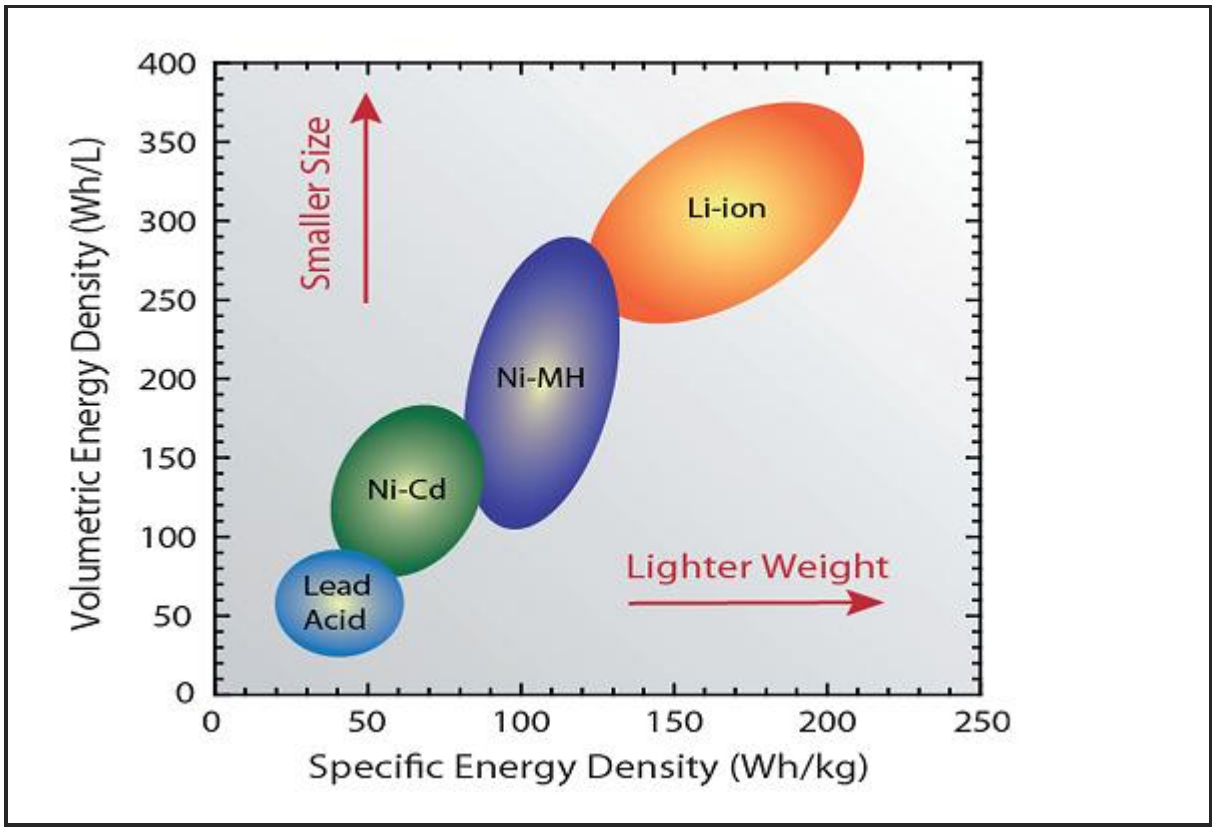


**Figure 2.2:** Rechargeable battery technologies as a function of volumetric and specific energy densities (Landi *et al*., 2009).

Lithium ion batteries consisting of one or more electrochemical cells connected in series or in parallel to achieve the desired current and voltage characteristics, are made up of a positive electrode (the cathode) and a negative electrode (the anode) (Szczech and Jin, 2011). The electrodes are separated from each other by a lithium ion permeable membrane and an electrolyte

that conducts the lithium ions (Szczech and Jin, 2011). Based on energy density considerations, lithium metal is one of the best anode material, because of its high inherent specific capacity (3860 mAh $g^{-1}$) (Szczech and Jin, 2011). However, present commercial challenges relates to its reactivity with the electrolyte (Landi *et al*., 2009), as well as the electroplating of dendritic lithium during charging (Figure 2.1**)**, which can result in short circuit, posing serious safety concerns for lithium metal anodes (Szczech and Jin, 2011). Commercially, the most popular material for use in fabricating the anode is graphite or carbon (Teki *et al*., 2009).

The cathode mainly falls into three categories namely, layered oxides such as $LiCoO_2$, transition metal phosphates such as $LiFePO_4$, or spinels such as $LiMn_2O_4$ (Teki *et al*., 2009). The electrolytes in lithium ion battery systems consists of lithium-salt, such as $LiPF_6$, $LiBF_4$, or $LiClO_4$, in an organic solvent such as alkene carbonates or mixtures of carbonates, amides, or imides (Teki *et al*., 2009). Besides the lithium salts, the electrolyte additives to the lithium ion batteries, such as vinylene carbonate (VC), 1,3-propane sultone (1,3-PS) and fluoroethylene carbonate (FEC) are usually used to improve the high temperature performance of lithium-ion batteries by forming stable and effective solid-electrolyte interface (SEI) film on the graphitic anode because these additives are generally more easily reduced than the electrolyte (Han *et al*., 2012). Among the above mentioned additives, vinylene carbonate (VC) can form a stable SEI on the graphite negative electrode and also improve the cycle performance of batteries (Han *et al*., 2012).

The choice of material for use in the anode, cathode and electrolyte combined with their physical, chemical, electronic and electrochemical attributes does affect the voltage, specific capacity, cycle

life and safety of a lithium-ion battery (Teki *et al*., 2009). Both the anode and cathode are generally materials into which the ionized lithium-ions can be inserted and extracted (Teki *et al*., 2009), because they are layered materials with interstitial spaces that are receptive to lithium-ion intercalation (Landi *et al*., 2009). The nature of the Li ion insertion and extraction do vary from electrochemical intercalation in the case of layered oxides and graphite which results in changes in the crystallographic and electronic structure to that of alloy formation in the case of silicon and tin (Teki *et al*., 2009).

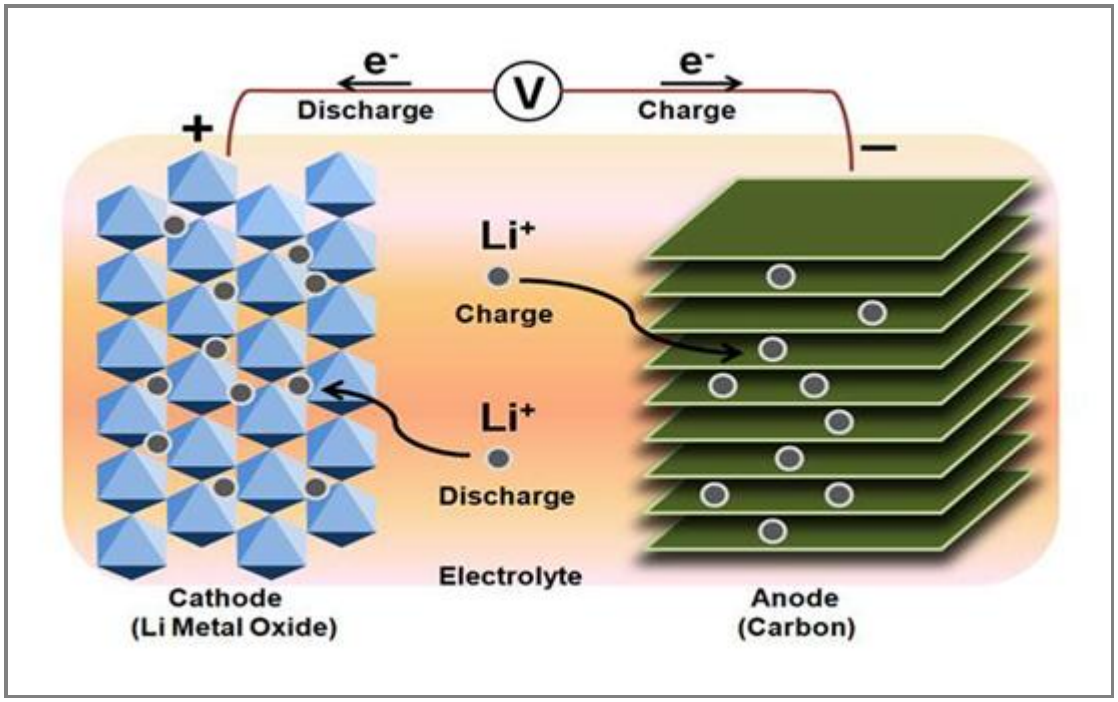


**Figure 2.3:** Schematic diagram of a conventional Li-ion battery showing the anode, cathode, and electrolyte (Teki *et al*., 2009).

The existing lithium ion battery (LIB) technology is based mainly on the combination of a carbon anode and a lithium metal oxide or phosphate cathode ($LiCoO_2$, $LiMn_2O_4$, $LiFePO_4$) **(**Figure 2.3) (Wu and Cui, 2012; McDowell *et al*., 2013). The overall performance of the anode and cathode is usually quantified in terms of the charge capacity per unit weight of the materials making up the

electrode (Teki *et al*., 2009). The relatively low capacity of the electrodes (370 mAh/g for graphitic carbon and 140-170 mAh/g for lithium metal oxide or phosphate) generally limits the total specific energy charge that can be delivered by the cell (Wu and Cui, 2012). Thus, the existing lithium ion battery technology (LIB) is currently reaching its limit in terms of energy density (per volume) and specific energy (per weight) (Wu and Cui, 2012).

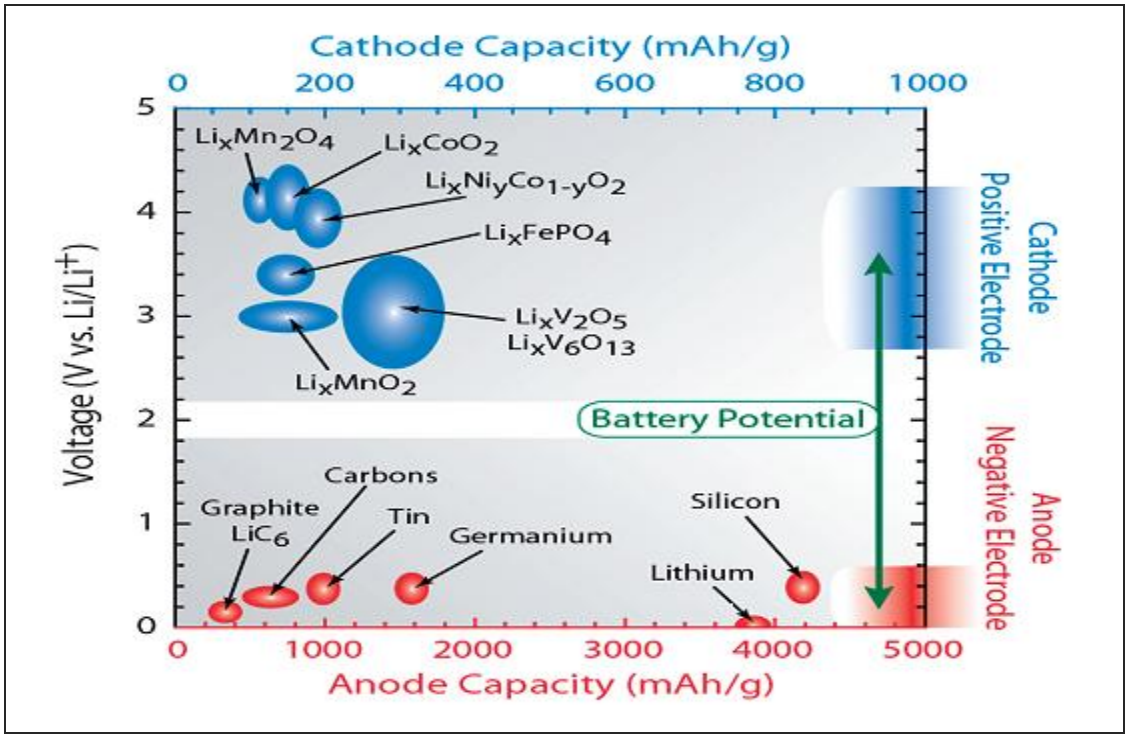


**Figure 2.4:** Lithium ion capacity and electrochemical reduction potentials with respect to lithium metal for conventional anode (red axis) and cathode materials (blue axis) (Landi *et al*., 2009).

From figure 2.4, the battery potential is obtained by finding the relative difference between the voltage of the selected positive electrode materials (blue ovals) and voltage of the corresponding negative electrode material (red ovals) (Landi *et al*., 2009). When such a cell is being charged, lithium-ions are extracted from the cathode and inserted into the anode, on being discharged, the lithium-ions are released by the "host" that is the anode and taken up again by the cathode (Guo *et*

*al*., 2008). The active material is able to store the lithium ion because of the simultaneous electron transport by the current collector to reduce the lithium ion at the active material ‘‘host’’ site (Landi *et al*., 2009).

The intercalation process is assisted by a necessary solid-electrolyte-interface (SEI) that usually forms on the surface of each electrode and which serves a critical role, namely to passivate the electrode surface from further solvent reduction and also act as a selective layer to allow only lithium ions to diffuse (Landi *et al*., 2009). The lithium ions are usually present in the electrolyte comprising a lithium salt, most often $LiPF_6$, solvated by a mixed solution of alkyl carbonates, such as ethylene carbonate (EC) and dimethyl carbonate (DMC) (Landi *et al*., 2009). The choice of electrolyte solvent used is critical to the formation of a stable SEI due to decomposition of both salt and solvent species leading to layered components like LiF and $LiCO_3$ (Landi *et al*., 2009).

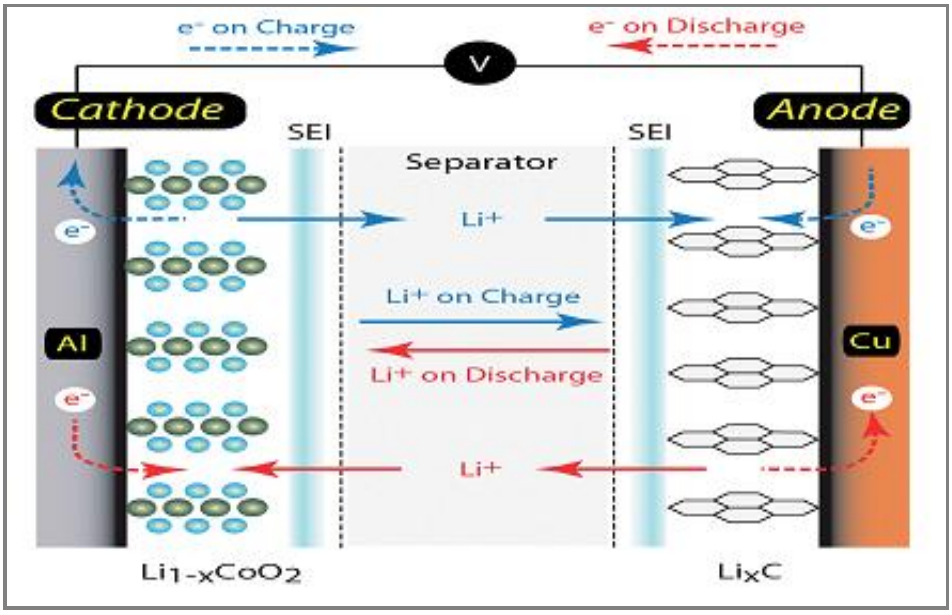


**Figure 2.5:** Schematic diagram illustrating the mechanism of operation for a lithium ion battery (Landi *et al*., 2009).

The schematic diagram (Figure 2.5) illustrates the mechanism of operation for a lithium ion battery, showing the movement of lithium-ions between electrodes (solid lines) and the electron transport through the complete electrical circuit (dashed lines) during charging (blue) and discharging (red) states (Landi *et al*., 2009). In commercial Li-ion batteries, where the positive electrode materials are metal oxides or phosphates (such as $LiCoO_2$ , $LiMnO_2$ , or $LiFePO_4$ ) and the negative electrode is graphite, both the positive and negative electrode materials react with Li via an intercalation mechanism (McDowell *et al*., 2013).

Intercalation mechanism involves Li ions or atoms residing in interstitial sites within the host lattice and thus the insertion and extraction of Li results in small strains and minimal irreversible structural changes in the host material (McDowell *et al*., 2013). The intercalation mechanism can result in good capacity retention over many cycles, but the specific charge capacity of these materials is relatively low due to the limited number of intercalation sites for Li ions within the host lattice (McDowell *et al*., 2013).

In contrast, negative electrode materials such as Sn, Ge, and Si react with Li via a different mechanism (McDowell *et al*., 2013). Li forms alloys with these materials, which involves breaking the bonds between host atoms hence causing dramatic structural changes in the process (McDowell *et al*., 2013). Since the atomic framework of the host does not constrain the reaction, anode materials that form alloys usually have much higher specific capacity than intercalation electrode materials (McDowell *et al*., 2013). For instance, the equilibrium Li-Si alloy with the highest Li concentration is the $Li_{22}$ $Si_5$ phase, which is much more Li-rich than fully-lithiated graphite ($LiC_6$ ) (McDowell *et al*., 2013).

In terms of theoretical specific charge capacity, the Li-Si alloy phase can attain 4200 mAh $g^{-1}$ while graphite exhibits only 372 mAh $g^{-1}$ (Table 2.1) (McDowell *et al*., 2013). The theoretical specific capacities for other alloying anodes such as Sn Ge and, are also very high (994 mAh $g^{-1}$ and 1623 mAh $g^{-1}$, respectively) (McDowell *et al*., 2013). Since the theoretical capacity of graphite (372 $mAhg^{-1}$) is low compared to other possible anode materials, such as the lithium alloys of silicon or tin, limiting the power density (Szczech and Jin, 2011). Development of high capacity anodes capable of sustaining high power rates is therefore necessary (Szczech and Jin, 2011). Among the many candidates of alloying anode materials, Si is considered one of the most promising because of its exceptionally high theoretical specific charge capacity, its abundance in the earth's crust and the benefits of a well-developed industrial infrastructure for manufacturing (McDowell *et al*., 2013).

**Table 2.1: Comparison of Various Anode Materials** (all the capacity numbers are based on materials in the delithiated state except lithium metal) (Wu and Cui, 2012).

| **Materials** | **Li** | **C** | **$Li_4Ti_5O_{12}$** | **Si** | **Sn** | **Sb** | **Al** | **Mg** |
|---|---|---|---|---|---|---|---|---|
| Density ($g/cm^3$) | 0.53 | 2.25 | 3.5 | 2.3 | 7.3 | 6.7 | 2.7 | 1.3 |
| Lithiated phase | Li | $LiC_6$ | $Li_7Ti_5O_{12}$ | $Li_{4.4}Si$ | $Li_{4.4}Sn$ | $Li_3Sb$ | LiAl | $Li_3Mg$ |
| Theoretical specific capacity (mAh/g) | 3862 | 372 | 175 | 4200 | 994 | 660 | 993 | 3350 |
| Volume change (%) | 100 | 12 | 1 | 420 | 260 | 200 | 96 | 100 |
| Potential versus Li (V) | 0 | 0.05 | 1.6 | 0.4 | 0.6 | 0.9 | 0.3 | 0.1 |

### 2.2 Silicon as a Li-ion Battery Anode

Silicon is among some of the most promising materials for fabricating Li-ion battery anodes because it has the highest known theoretical specific charge capacity of 4200 mAh $g^{-1}$, this is greater than ten times the specific charge of the existing graphite anodes (372 mAh $g^{-1}$), and

various other oxide and nitride materials (Teki *et al*., 2009; Park *et al*., 2009). Moreover silicon has a low discharge potential (~ 370 mV vs. $Li/Li^+$), thus making it suitable for use in high-power applications when paired with commercially available cathode materials such as $LiCoO_2$ or $LiMn_2O_4$ (Teki *et al*., 2009). It is also non-toxic and thus considerable attention has been given to the use of silicon as a lithium ion battery anode material ( Teki *et al*., 2009; Szczech and Jin, 2011).

During the reaction of silicon with lithium, silicon is known to incorporate 4.4 lithium atoms per every silicon atom (Table 2.1) (Park *et al*., 2009), thus creating an alloy with high electrochemical capacity (Szczech and Jin, 2011). The lithiation process in silicon anodes results in the formation of $Li_{12}Si_7$, $Li_{14}Si_6$, $Li_{13}Si_4$, and $Li_{22}Si_5$ alloys (Kasavajjula *et al*., 2007). The alloy phase in the Li-Si system containing maximum lithium is $Li_{22}Si_5$ (Wang and Kumta, 2010). Just like graphite, the discharge curve of silicon also displays a long plateau over much of its discharge, thus delivering a stable voltage during cycling (Szczech and Jin, 2011). Moreover silicon does not suffer from solvent co-intercalation, this presents an additional advantage over graphite (Szczech and Jin, 2011).

However, the large number of lithium atoms that can be intercalated into silicon anode materials results in huge volume changes (approximately 310 % volume change for a fully lithiated silicon anode) (McDowell *et al*., 2013). Such large structural and volumetric changes during lithium insertion and extraction often results in rapid capacity decay with cycling (McDowell *et al*., 2013). This is mainly due to fracture or mechanical decrepitation of particles and irreversible side

reactions with the organic electrolyte that are aggravated by the huge volume changes (McDowell *et al*., 2013).

One mechanism through which mechanical fracture is thought to cause rapid capacity decay is through electrical isolation of fragments of the fractured active material (Figure 2.6 and Figure 2.7) thus, the commercial application of silicon as an anode material in the common lithium-ion batteries has been limited by mechanical degradation and capacity decay that have typically prevented good cycling performance resulting in electrode failure (Wang and Kumta, 2010; Wu and Cui, 2012; McDowell *et al*., 2013).

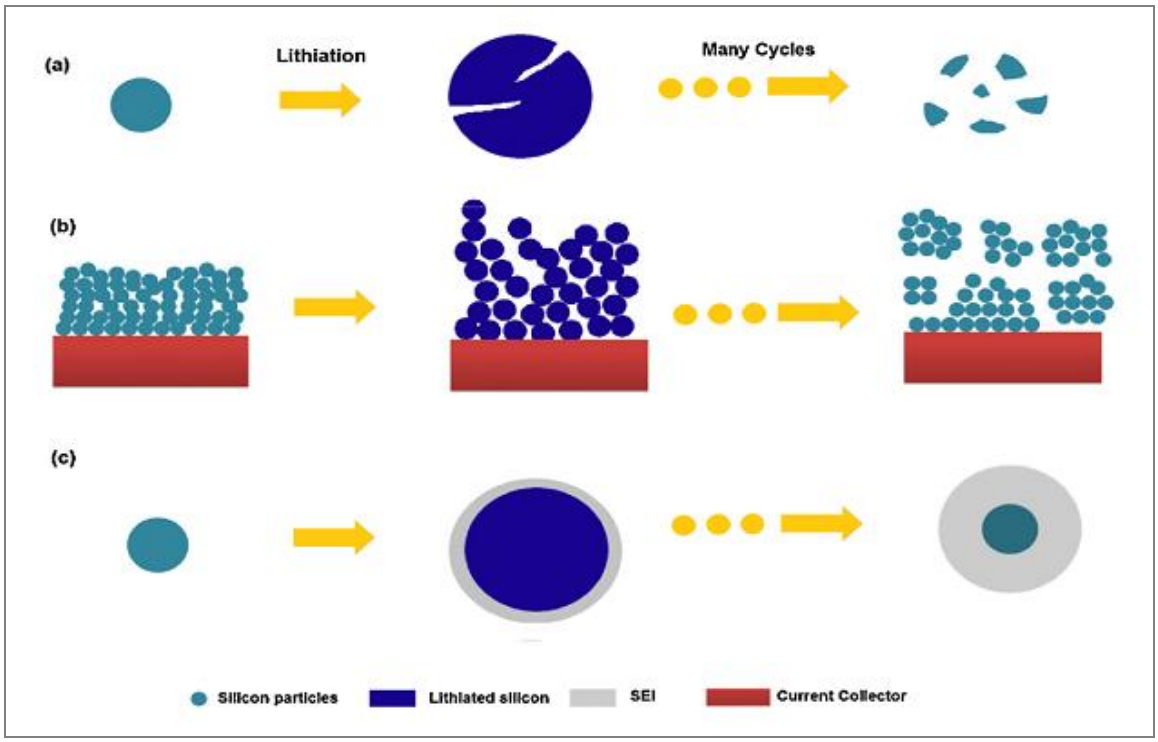


**Figure 2.6:** Si electrode failure mechanisms: (a) Material pulverization. (b) Morphology and volume change of the entire Si electrode. (c) Continuous SEI growth (Wu and Cui, 2012).

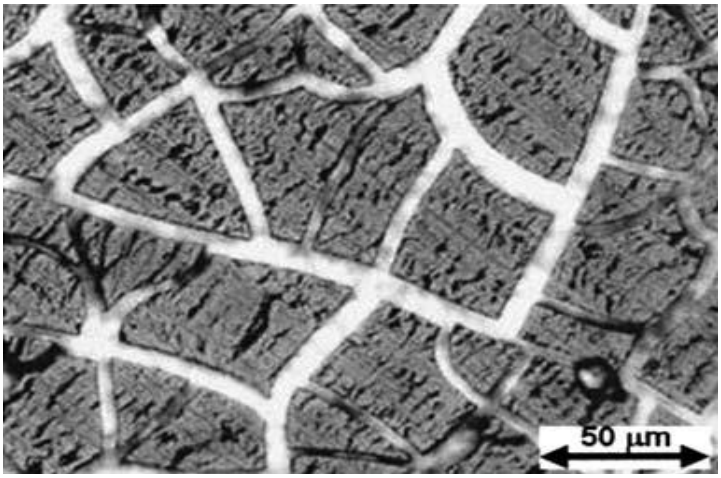


**Figure 2.7:** Optical micrograph of a cracked thin silicon film after lithiation and delithiation (Szczech and Jin, 2011).

Preventing mechanical degradation and reducing significantly the side reactions in silicon anodes during electrochemical lithium insertion and extraction is thus, critical in an effort towards utilizing their high specific charge capacity for high energy density and longer lasting Li-ion batteries (McDowell *et al*., 2013). This challenge can potentially be overcome by using silicon nanostructures that can impart facile strain relaxation thus preventing electrode pulverization, maintain essential electrical contact and have more benefits of short lithium diffusion distances and increased mass transport (Szczech and Jin, 2011). Silicon nanostructures are also advantageous for a number of reasons, which include their ability to accommodate lithiation-induced strain without fracturing on top of having a good cycle rate ability (McDowell *et al*., 2013).

### 2.3 Nanostructured Silicon as a Li-ion Battery Anode

The development of nanostructured silicon electrodes to overcome the limitations of bulk crystalline expansion can be achieved by either decreasing the size of the semiconductor particles

to the nanoscale or through the introduction of other functional nanomaterials (Landi *et al*., 2009). It has been shown previously that reducing a material's particle size to nanoscale dimensions (less than 100 nm) can change the crystal structure and may even modify the mechanism of volumetric expansion during lithium insertion (Landi *et al*., 2009). This is because nanoscale dimensions allows quick stress relaxation, thus making the nanoparticles more resistant to fracture than the bulk crystals (Szczech and Jin, 2011).

Nanostructured materials can play a big role in enhancing the performance of lithium-ion batteries, because in nanoscale dimensions the distances over which lithium ions diffuse is dramatically reduced, hence, such nanostructured materials can quickly absorb and store large number of Li-ions without causing any degradation in the electrode (Guo *et al*., 2008). The nanoparticles also possess large surface areas, short distance of diffusion and fast rates of diffusion along their many grain boundaries (Guo *et al*., 2008). The enhanced capacities, high cycle rate performance and capacity retention capabilities of many common lithium storage systems have been found to benefit from nanoscale effects (Guo *et al*., 2008).

**2.4 Sources of Silicon Nanoparticles**

Silicon nanoparticles can be obtained using various methods which include; vapor-phase reaction, sol-gel and thermal decomposition technique, but their wide application has been limited by its high cost of preparation (Chen *et al*., 2010; Liou and Wu, 2010). Bulk silicon crystals are usually produced for use in industrial applications by carbothermic reduction of silica, which requires temperatures over 2000 $^{o}$C which is way above 1410 $^{o}$C, the melting point of silicon, thus metallurgical-grade silicon is made up of micron-sized crystal particles whose purity is $\sim$ 98 %

(Liu *et al*., 2013). The particle size are big because of the melting of silicon during the carbothermic reduction process involving high temperatures (Liu *et al*., 2013). Unlike the metallurgical-grade silicon, economically viable and high grade nano-sized silicon can be obtained from rice husks (D. Singh *et al*., 2008).

Amorphous silica can be obtained from rice husks by simply burning the husks under appropriate conditions (D. Singh *et al*., 2008). Wheat, which also belongs to the Gramineae family (Chen *et al*., 2010), is abundantly available, renewable and currently used in some limited applications (Zhang *et al*., 2012). It is only second to rice husks in the amount of silica it contains (Chen *et al*., 2010). In their ashes the silica content is over 90 % by mass with minor amounts of metallic impurities, making it one of the most economical source of nano-sized silica (Chen *et al*., 2010). The silica extracted from rice husks or wheat can be subjected to heat scavenger assisted magnesiothermic reduction to synthesize silicon nanoparticles (Liu *et al*., 2013).

**2.5 Rice Husks as a Source of Amorphous Silica**

The extraction of functional nano-sized silica from rice husks is a simple process compared to other conventional techniques of production such as vapor-phase reaction and sol-gel process (Rafiee *et al*., 2012). Dusts and other adhering solid impurities can be removed by thoroughly rinsing rice husks with distilled water (Yuvakkumar, *et al*., 2012). Silica of varying purity can be produced by direct incineration of rice husks with or without the use of pre-treatments (Ugheoke and Mamat, 2012). Incineration of rice husks generates 17 % to 20 % ash, of which about 87 % to 93 % is silica with minor metallic oxide impurities depending on the source of the husks, such

high percentage of silica content found intermingling with plant fibers is quite rare in nature (Ugheoke and Mamat, 2012).

The percentage purity and colour of the ash obtained is influenced by the amount of the various metallic ions and unburned carbon respectively (Ghosh and Bhattacherjee, 2013). Controlled incineration of rice husks after removal of these metallic ions can yield white silica of high purity (Ghosh and Bhattacherjee, 2013). To obtain high purity silica from rice husks three main pre-treatment methods have generally been employed, these are; acid leaching, basic pre-treatment and microbiological pre-treatment usually in combination with some acids (Ugheoke and Mamat, 2012). Before other value adding processes such as incineration begin different kinds of acids, both mineral and organic, have been reported to be used to pre-treat rice husks (Ugheoke and Mamat, 2012). However, HCl has proved to be the most efficient in the removal of metallic impurities from the rice husks and thus is by far the most widely used (Ugheoke and Mamat, 2012).

The structural nature of the silica obtained from rice husks is independent of the methods of purification but mainly dependent on the temperature of incineration used (Ugheoke and Mamat, 2012). For instance, incinerating at a temperature of about 300 $^{o}$C to 450 $^{o}$C only transforms raw rice husks to carbonised rice husks ash, whereas; an incineration temperature of between 500 $^{o}$C to 650 $^{o}$C produces white or grey ash, depending on holding/soaking time, that is the duration for which the incineration is allowed to take place at the stated temperature range (Ugheoke and Mamat, 2012). Silica obtained at a temperature of incineration of about 500 $^{o}$C to 650 $^{o}$C with incineration holding/soaking time of 2½ hours to 6 hours is considered ideal for obtaining white

amorphous silica while crystallinity begins to set in when the temperature of incineration increases beyond 700 $^{o}$C (Ugheoke and Mamat, 2012).

**2.6 Synthesis of Silicon Nanoparticles**

Silicon nanoparticles can be obtained directly by magnesiothermic reduction of silica, however, the massive heat released from such exothermic reaction can collapse the architectures of the silica precursors and agglomerate as-synthesized silicon nano-domains into large crystals (Luo *et al*., 2013). The nanoporous domains of silica can thus be preserved during the magnesiothermic reduction reaction (MRR) with the assistance of a low cost heat scavenger (NaCl) (Luo *et al*., 2013). The heat released in this exothermic reaction is scavenged by the fusion of NaCl and thus, effectively preventing the structure collapse and aggregation of the silicon domains (Luo *et al*., 2013).

**2.7 Characterization of Silica and Silicon Nanoparticles**

Characterization of nano-sized silica and silicon nanoparticles derived from rice husks can be performed using various equipment and methods of analysis. The major chemical groups present in silica can be identified by FTIR (Okoronkwo *et al*., 2013). An elemental mapping analysis on silica samples can be done using energy-dispersive X-ray spectroscopy (EDX) (Chen *et al*., 2012; Quercia *et al*., 2013). Structural properties of the silicon powder produced can be studied using X-ray diffraction (XRD) (Odo *et al*., 2012).

### 2.7.1 Fourier Transform Infrared (FTIR) Spectroscopy.

Fourier transform infrared (FTIR) spectroscopy is a physico-chemical method of analysis which is based on the measurement of vibrations of a molecule excited by IR radiation at a specific wavelength range (Davis and Mauer, 2010). Figure 2.8 presents a general schematic diagram of an FTIR spectrometer. The IR source emits radiation that is passed through an interferometer, usually a Michelson interferometer with a beam splitter (a semi-reflecting film usually made of KBr), a fixed mirror, and a moving mirror (Davis and Mauer, 2010). The interferometer uses interference patterns to make accurate measurements of the wavelength of light (Davis and Mauer, 2010). When IR radiation is passed through a sample, some radiation is absorbed and the rest is transmitted to the detector (Davis and Mauer, 2010).

The detector measures the total Interferogram from all the different IR wavelengths (Davis and Mauer, 2010). A mathematical function called Fourier transform converts the interferogram (an intensity versus time spectrum) into an IR spectrum (an intensity versus frequency spectrum) (Davis and Mauer, 2010). Most mid-IR analyses are performed with a DTGS (deuterated triglycine sulfate) detector due to its ease of use and high sensitivity (Davis and Mauer, 2010). When sample measurements must be made at high speed, the mercury cadmium telluride (MCT) detector is used which is 4-10 times more sensitive than the DTGS detector (Davis and Mauer, 2010).

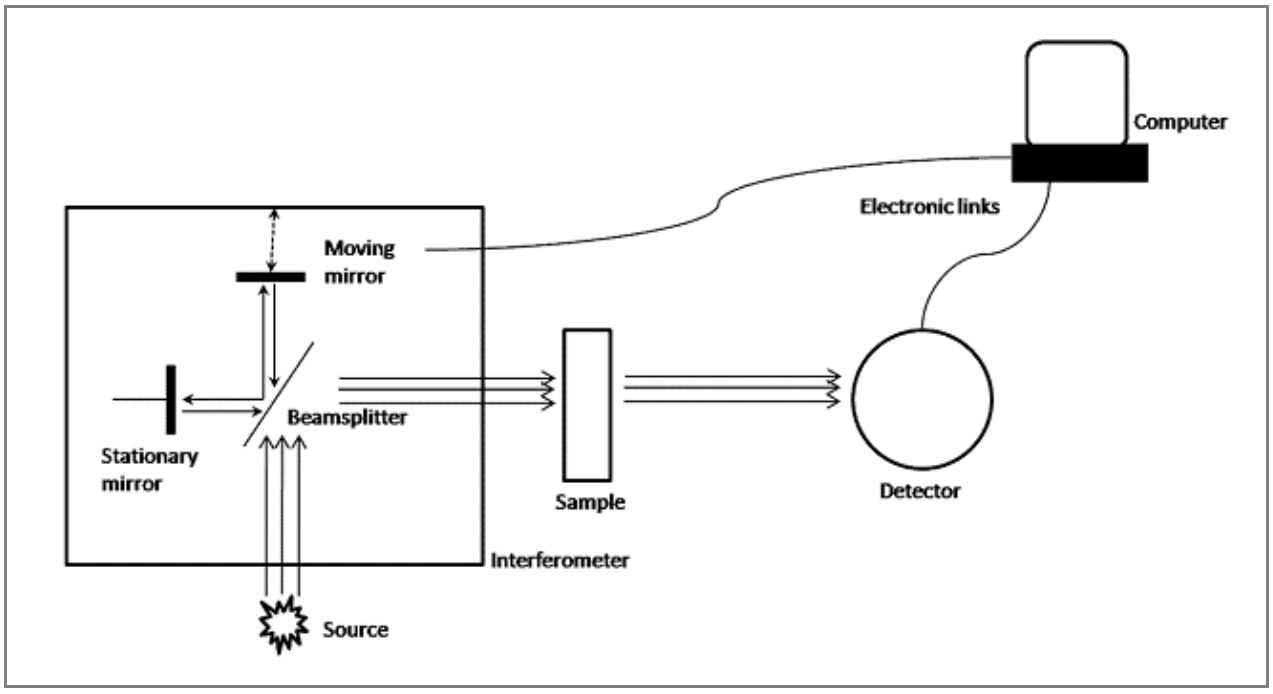


**Figure 2.8:** A schematic diagram showing the basic components of an FTIR spectrometer (Davis and Mauer, 2010).

The infrared (IR) region (10 $cm^{-1}$ - 14000 $cm^{-1}$) of the electromagnetic spectrum is divided into three regions: the near-, mid-, and far-IR (Davis and Mauer, 2010). The Mid-infrared region (400 $cm^{-1}$ - 4000 $cm^{-1}$) is the most commonly used region for analysis since all molecules possess characteristic absorbance frequencies and primary molecular vibrations in this range (Davis and Mauer, 2010). Mid-infrared spectroscopy methods are based on studying the interaction of IR radiation with samples (Davis and Mauer, 2010). As infrared radiation is passed through a sample, specific wavelengths are absorbed causing chemical bonds in the material to undergo vibrations such as bending, stretching and contracting (Davis and Mauer, 2010).

### 2.7.2 Energy Dispersive X-ray Fluorescence (EDX)

X-ray spectroscopy is one of the most sensitive, nondestructive analytical techniques for chemical analysis, providing both qualitative and quantitative compositional information of virtually any

material (Wollman *et al*., 1997; Chen *et al*., 2008). It is widely used for environmental, industrial, pharmaceutical, forensic and scientific research applications to determine the presence or absence and in some cases measure the concentration of elemental constituents or contaminants (Chen *et al*., 2008). The fluorescing atoms can be excited by energetic electrons, ions, or photons (Chen *et al*., 2008).

In energy dispersive X-ray (EDX) analysis, the incident electron beam excites an electron in an inner shell, causing its ejection and the formation of an electron hole in the electronic structure of the atom (Rao and Biswas, 2009). An electron from a higher-energy (outer) shell fills the hole in the electronic structure and the difference in energy between the higher-energy shell and the lower-energy shell is released as X-rays (Rao and Biswas, 2009). Electron holes might be generated in all electronic states, here the K and L shell; the electron hole in the K shell might be filled by an electron from the L or the M shell, leading to Kα or Kβ radiation, respectively (Figure 2.9) (Krumeick, 2011). A vacancy in the L shell can be filled by an electron from the M shell generating Lα radiation (Krumeick, 2011).

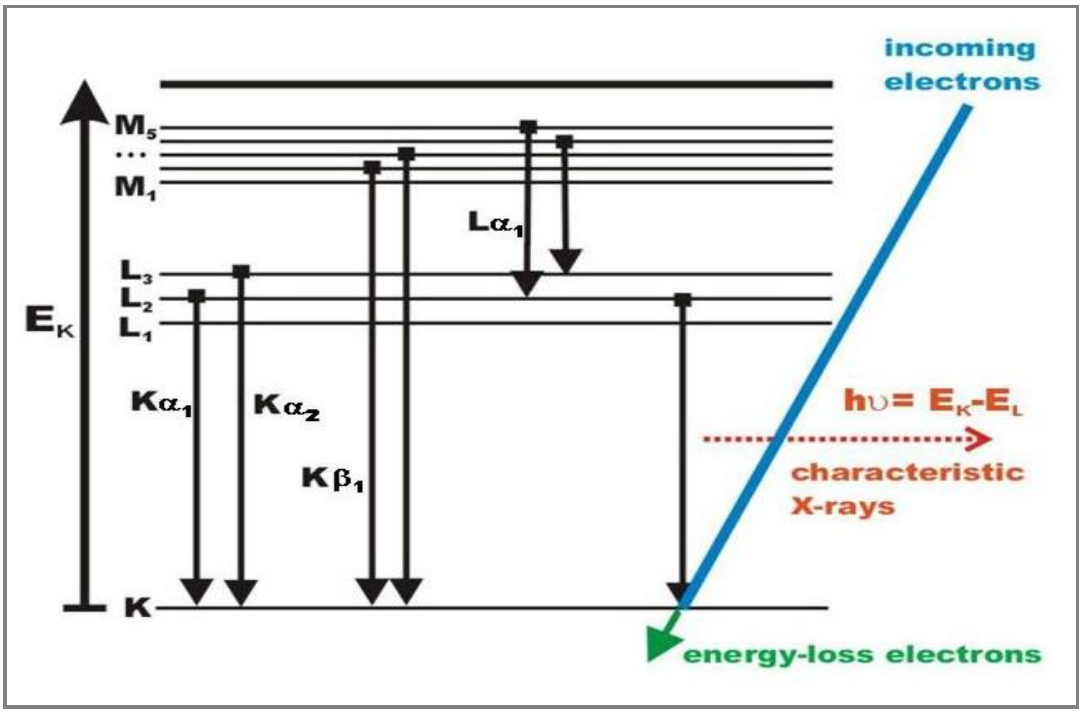


**Figure 2.9:** Possible electron transitions generating X-rays (Krumeick, 2011).

The fluorescent X-rays are in general measured by two types of detection systems: energy dispersive detection (EDXRF) and wavelength dispersive detection (WDXRF) (Chen *et al*., 2008). Thus, two types of X-ray spectrometers are currently used for X-ray microanalysis, wavelength-dispersive (WD) and energy-dispersive (ED) spectrometers (Wollman *et al*., 1997). In EDXRF systems, the emitted X-rays are detected by their energies, whereas in wavelength-dispersive X-ray fluorescence (WDXRF) systems, the *physical* equivalent to energy, the wavelength of the characteristic photon is measured (Wobrauschek *et al*., 2006). This statement can be explained by the simple relation expressed in equation 2.1;

$E = hv$, but $\lambda.v = c$; Implying $E = hc/\lambda$, thus $E\ (keV) = 1.2396/\lambda\ (nm)$ (2.1)

Where $E$ is energy of the X-rays, $v$ is velocity of the photon, $c$ is the speed of light and $\lambda$ represents wavelength of the incident X-ray beam (Wobrauschek *et al*., 2006).

WDXRF utilizes the properties of single crystals to diffract X-rays of a specific wavelength under a specific angle (Bragg's law) and the intensity of the diffracted radiation is counted by a simple radiation counter e.g. Geiger–Muller counter (Wobrauschek *et al*., 2006). As characteristic radiation for one element has a fixed well-defined value of λ only at specific angles, a high intensity of the refracted radiation is measured (Wobrauschek *et al*., 2006). So using a goniometer with the Bragg crystal as the dispersive element in its center and a detector at the circumference, a continuous rotation will result in intensive peaks whenever the condition of Bragg's law (Equation 2.5) is fulfilled (Wobrauschek *et al*., 2006). By continuous rotation of the detector from 0° to 180° angle 2$\theta$, while the crystal is in position $\theta$, collects the photons reflected (Wobrauschek *et al*., 2006). This sequential measurement leads to a spectrum ''intensity versus wavelength'' allowing determination of elements and concentration in the sample because the intensity is proportional to the concentration of the respective element (Wobrauschek *et al*., 2006).

In the case of EDXRF, the detector crystal, made of lithium-drifted silicon Si(Li) or hyperpure Ge germanium takes on two tasks namely; dispersion according to the energy and counting of the photons of individual energy (Wobrauschek *et al*., 2006). This collection process results in a spectrum ''intensity versus energy'' of the characteristic radiation emitted from the sample (Wobrauschek *et al*., 2006). Conventional EDXRF has the advantages of moderate cost and the possibility of determining simultaneously a wide range of elements, as well as the possibility of automatic running; no dissolution step is required prior to analysis (Spolnik *et al*., 2005). These features lead to energy-dispersive x-ray fluorescence being convenient for analysis of samples in this study.

### 2.7.3 X-Ray Diffraction (XRD) Spectrometry

X-ray Diffraction (XRD) is one of the primary techniques used by solid state chemists and mineralogists to examine the physico-chemical make-up of unknown materials (Theivasanthi and Alagar, 2010). In XRD, a monochromatic X-ray beam is focused on sample material to resolve structural information in the crystal lattice (Rasel Das *et al*., 2014). When X-ray falls over a crystal sample, it diffracts in a pattern characteristic to its structure (Chauhan and Chauhan, 2014). Usually, the materials are composed of repeating uniform atomic planes which make up their crystal (Rasel Das *et al*., 2014).

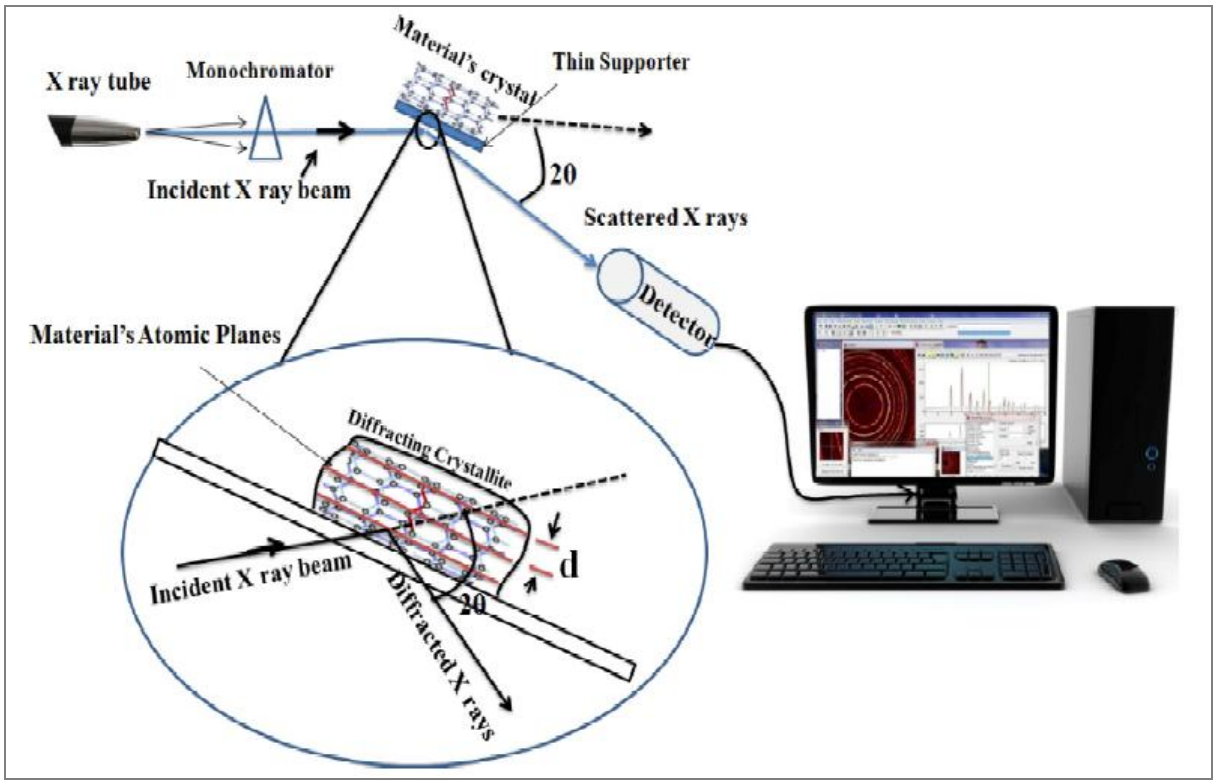


**Figure 2.10:** Schematic diagram of basic principle of XRD (Rasel Das *et al*., 2014).

Typically, polychromatic X-rays are produced in a special tube called cathode-ray tube (figure 2.10), under vacuum atmosphere (Rasel Das *et al*., 2014). Application of 15 - 60 kilovolts current

within the tube gives electrons which hit a Cr, Fe, Co, Cu, Mo or Ag anode from which X-ray beams are generated (Rasel Das *et al*., 2014). Filtering polychromatic X-rays through a monochromator produces monochromatic radiation which hits onto the material atomic planes, separating the diffracted, transmitted and absorbed rays (Rasel Das *et al*., 2014). The produced X-rays are then collimated and directed onto a powder sample having diameter <10 μm (Rasel Das *et al*., 2014). Interactions between the incident X-ray beam and the sample produce intense reflected X-rays by constructive interference when conditions satisfy Bragg's Law (Equation 2.5) (Chauhan and Chauhan, 2014).

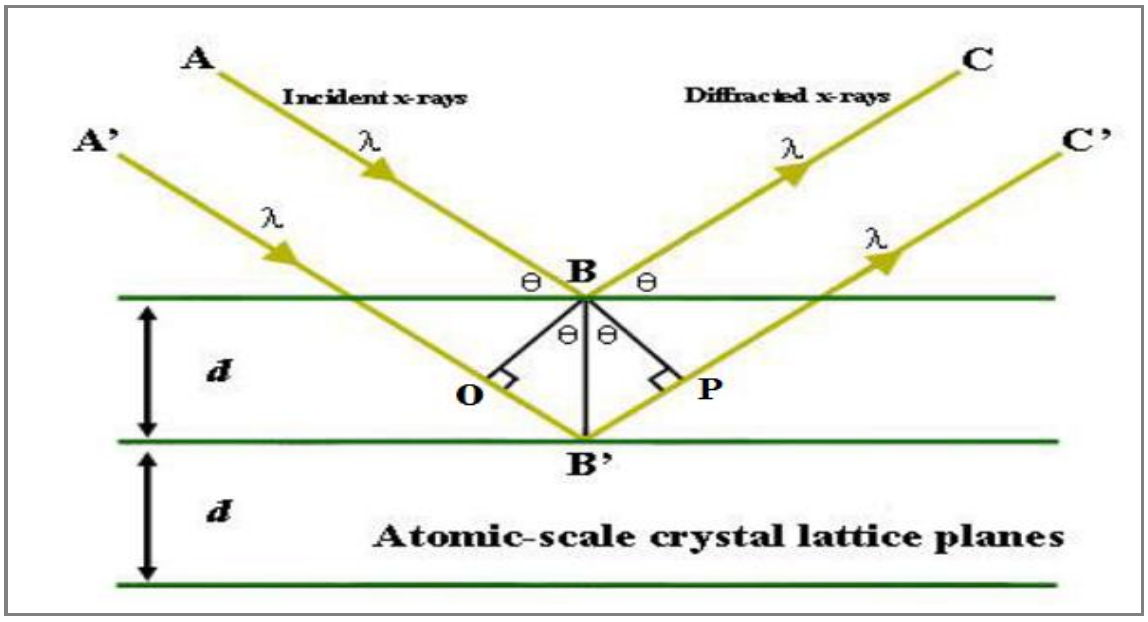


**Figure 2.11:** Bragg's representation of the diffraction condition as the reflection of X-rays by lattice planes (Khondker and Lakhani, 2015).

Bragg's law can be derived using reflection geometry and trigonometry (Khondker and Lakhani, 2015). Constructive interference occurs when the differences in the travel path of the incident X-rays is equal to an integer multiple of the wavelength (Chauhan and Chauhan, 2014). In figure 2.11, incident rays A and A' are parallel and in phase up until A strikes the first plane at point B,

while A' continues to the next plane and is scattered by the atom B' (Khondker and Lakhani, 2015). If the two beams are to resume travelling in phase and parallel as C and C', the second beam must travel the extra distance marked on either side of B' by the right angle to point B' (let us call these points O and P), both while incident and after being scattered (Khondker and Lakhani, 2015).

If the phases of the two beams are to remain the same upon exit, then this extra distance must be an integral multiple (n) of wavelength (λ) (Khondker and Lakhani, 2015).

Therefore; $n \lambda = OB' + PB'$ (2.2)

To find OB' and PB', we can apply basic trigonometry (Khondker and Lakhani, 2015). Noting that "d" is the hypotenuse of the right triangles BOB' and BPB', we can say that;

$OB' = d \sin \theta$ (2.3)

Since OB' = PB', we can therefore state;

$n \lambda = 2\ OB'$ (2.4)

Substituting equation (2.3) into equation (2.4) yields Bragg's law (Equation 2.5), (Khondker and Lakhani, 2015).

$n \lambda = 2d \sin \theta$ (2.5)

Where *n* is an integer defining order of diffracted beam, λ represents wavelength of the incident X-ray beam, *d* marks the distance between near atomic planes or *d*-spacing and $\theta$ represents the angle of the incident X-ray (Rasel Das *et al*., 2014).

Bragg's law thus, describes the general relationship between the wavelength of the incident X-rays, the angle of incident beam and the spacing between the crystal lattice planes of atoms (Chauhan and Chauhan, 2014). The *d*-spacing of the set of planes generating a diffraction peak

may be easily calculated from observed diffraction angles, provided the wavelength is known, using the Bragg equation (Lavina *et al*., 2014). Changeover of diffracted patterns into *d*-spacings allows recognition of the unknown sample (Rasel Das *et al*., 2014).

Materials are typically identified by comparing the diffracted pattern beams with many reference patterns stored in the Joint Committee on Powder Diffraction Standards (JCPDS) library (Rasel Das *et al*., 2014). The most commonly used database for identification of crystal structures is the Joint Committee on Powder Diffraction Standards–International Center for Diffraction Data (JCPDS-ICDD) system (Rao and Biswas, 2009).

Inspection of Bragg's law (Equation 2.5) reveals that each unique *d*-spacing will diffract different wavelengths at their own unique diffraction angles (Jenkins, 2006). Thus, if a pattern were measured using an X-ray beam containing two wavelengths, the observed pattern would, in fact, be two patterns (one for each wavelength) superimposed on one another, and clearly will be more difficult to interpret than a diffractogram from a single wavelength (Jenkins, 2006). Thus, the basic purpose of the monochromatization of the X-ray radiation is to obtain an experimental pattern from a single, unique wavelength (Jenkins, 2006).

### 2.7.4 Particle Size Analysis

X-ray diffraction is one of the convenient methods for determining the mean size of nano crystallites in nano crystalline bulk materials (Monshi *et al*., 2012). XRD has a good potential for the analysis of nanostructures, because the shape and width of reflections yield information about the substructure of the materials (sizes of crystallites, microstrain of a lattice and dislocation

structures) (Dorofeev *et al*., 2012). Scherrer's equation was developed in 1918, to calculate the nano crystallite size by XRD radiation of wavelength $\lambda$ (nm) from measuring full width at half maximum of peaks ($\beta$) in radians located at any $2\theta$ in the pattern (Monshi *et al*., 2012).

From Scherrer's equation (2.6); the average crystallite size, *D*, is expressed as:

$$D = \frac{K\lambda}{\beta . Cos\theta} \qquad (2.6)$$

Where $\beta$ is the peak width of the diffraction peak profile at half maximum height resulting from small crystallite size in radians, $\lambda$ is the X-ray wavelength in nanometer (nm) and *K* is a constant related to crystallite shape, can be 0.62 - 2.08 and is usually taken as about 0.89 or 0.94 for Full Width Half Maximum (FWHM) of spherical crystals with cubic unit cells (Monshi *et al*., 2012; Yuvakkumar *et al*., 2012). The value of $\beta$ in $2\theta$ axis of diffraction profile must be in radians (Monshi *et al*., 2012). The $\theta$ can be in degrees or radians (Monshi *et al*., 2012).

### 2.7.5 Electron Microscopy (EM)

#### 2.7.5.1 Introduction to Electron Microscopy

The two basic types of electron microscopes (EM) are the transmission electron microscope (TEM) and the scanning electron microscope (SEM) (Stadtländer, 2007). SEM generates an image with the help of secondary electrons that gives a viewer the impression of three dimensions, while TEM projects electrons through an ultrathin slice of the specimen and produces a two dimensional image (Stadtländer, 2007). Depending on the instrument used, specimens can be magnified roughly by between 10 and 100,000 times in scanning electron microscopes and 500 to 500,000 times in transmission electron microscopes (Stadtländer, 2007). The relatively high magnification range of both basic types of EM allows investigators to examine specimens with

much greater detail than in those examined by light microscope (LM) which uses visible light as a source of illumination and optical (glass) lenses to magnify specimens in the range of approximately 10 to 1,000 times their original size, makes electron microscopes extremely valuable tools for the ultra-structural examination of any kind of object, but in particular for specimens of very small size (Stadtländer, 2007). At present, scanning electron microscopy is heavily used in the pursuit of better understanding of nanomaterials, because of the recent significant improvements in SEM for imaging, diffraction and analysis of elements in terms of spatial resolution and sensitivities (Suga *et al*., 2014).

**2.7.5.2 The basic Principles of SEM**

The scanning electron microscope (SEM) uses electrons to form an image. A beam of electrons is produced in an electron gun at the top of the microscope and follows a vertical path through the column of the microscope, making its way through electromagnetic lenses which focus and direct the beam down towards the sample. The beam then passes through pairs of scanning coils or pairs of deflector plates in the electron column typically, which deflect the beam in the x and y planes so that it scans over a rectangular area of the sample surface (Figure 2.12).

The scanning electron microscope thus, scans a high-energy electron beam across the surface of a specimen and measures one of a number of signals resulting from the interaction between the beam and specimen (Stutzman, 2004). The interaction between the sample and the electron probe (impacted electrons i.e., IE) produces various types of emissions, which are captured by different detectors placed in appropriate positions (Suga *et al*., 2014). These are mainly secondary

electrons, with energies of a few tens of electron-volts (eV), high-energy electrons backscattered from the primary beam and characteristic X-rays (Bogner *et al*., 2007).

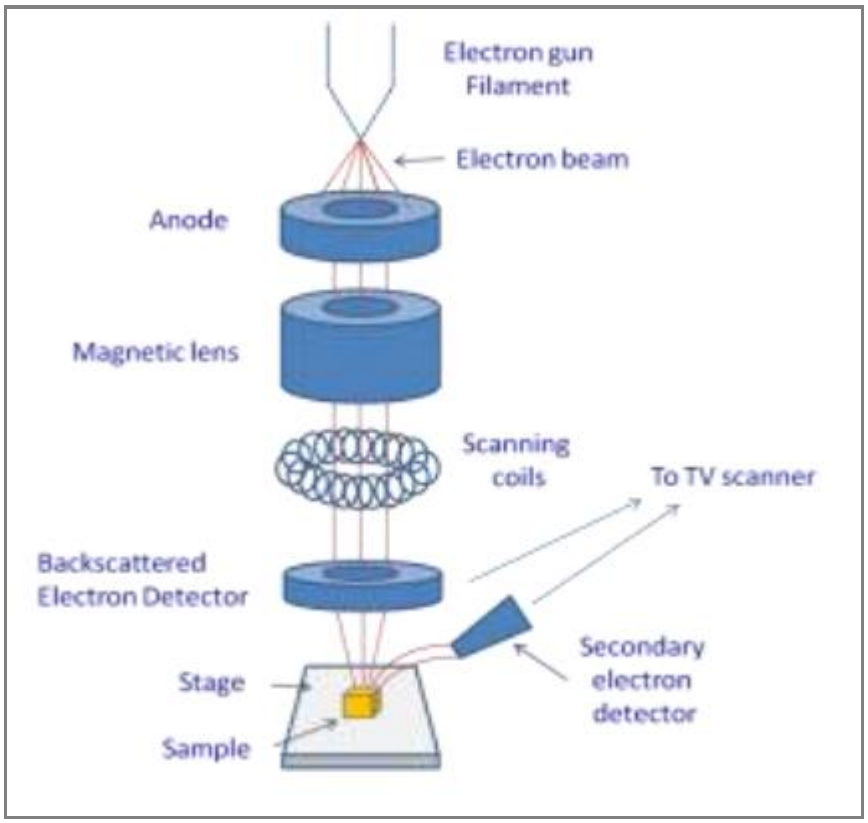


**Figure 2.12:** Schematic diagram of a Scanning electron microscope (Cortadellas *et al*., 2012)

When interacting with the sample, the electrons are affected by both elastic scattering, due to the electrostatic interaction with atomic nuclei and also inelastic scattering, due to the interaction with the atomic electrons (Dinescu *et al*., 2013). Elastic scattering is an interaction process which results in the direction of the basic electrons changing without any obvious energy loss (Dinescu *et al*., 2013). Since the electron beam leaves the sample (process called "backscattering"), the elastic scattering can give important information for the SEM image (Dinescu *et al*., 2013). Since the ratio between the number of backscattered electrons (BSE) and the number of basic electrons

depends on the atomic number (linear for a small Z), the image obtained by using the BSE signal offers information mainly about the composition of the sample, but it can also offer information about its topography (Dinescu *et al*., 2013).

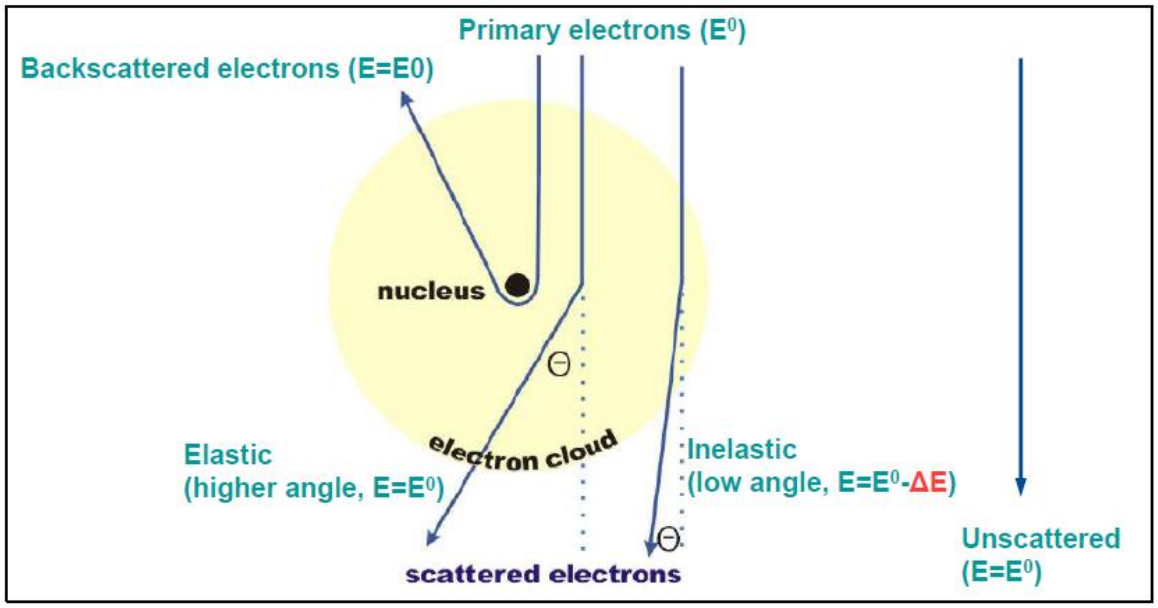


**Figure 2.13:** Interaction of electrons with an atom (Krumeick, 2011).

Inelastic scattering is an interaction process which results in basic electrons losing energy and transferring it to the sample atoms differently (Dinescu *et al*., 2013). A small part of the kinetic energy may escape as secondary electrons, useful for creating an image, X-rays for analyzing the elemental composition of the sample (Dinescu *et al*., 2013). According to the law of conservation of energy which is applied to this process, the basic electrons transfer their energy to the electrons from the atoms in the sample (Dinescu *et al*., 2013). If these are weakly held to the nucleus, they leave the atom and move into the solid as secondary electrons (SE) (Dinescu *et al*., 2013). In their movement, they interact with other atoms, gradually losing their kinetic energy (Dinescu *et al*., 2013). Most of them stop within the interaction volume (Dinescu *et al*., 2013). The ones which

were generated at a small depth near the surface may escape into vacuum (Dinescu *et al*., 2013). That is why the image obtained by using the SE signal offers information about the structure (topography) of the surface of the sample (Dinescu *et al*., 2013). It should be noted that inelastically scattered electrons lead to a variety of processes like heating, radiation and electron emission (Krumeick, 2011).

Morphological/topological-contrast and elemental composition information are separately obtained by selecting specific types of emitted electrons, known as secondary electrons (SEs - with energies smaller than 50 eV) and backscattered electrons (BSEs - with energies larger than 50 eV), respectively (Figure 2.14) (Suga *et al*., 2014). Backscattered electrons are high-energy electrons (>50 eV) that have undergone multiple elastic scattering events within the specimen (Stutzman, 2004). The greater energy results in a larger interaction volume and lower spatial resolution compared to the secondary electron image (Stutzman, 2004). Contrast is generated by the different phases relative to their average atomic number (Stutzman, 2004). This is observed by the differential brightness in the image (Stutzman, 2004).

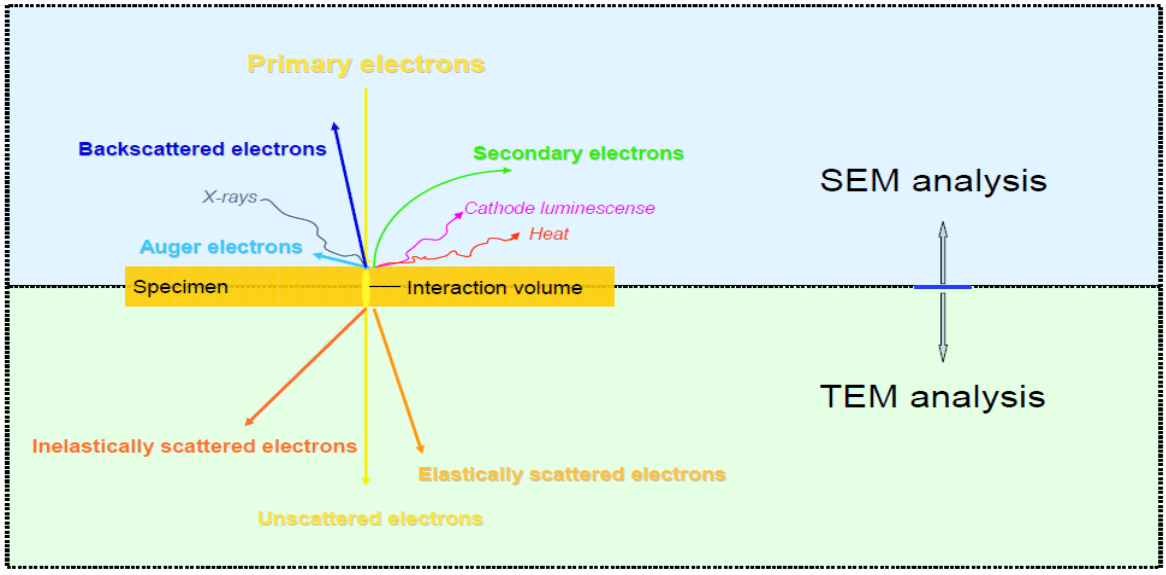


**Figure 2.14:** Interaction of electrons with specimen/matter; induced radiation and emission (Kaech, 2013).

Elemental composition information is obtained through the detection of characteristic X-rays using an X-ray detector (Suga *et al*., 2014). If an electron leaves an atom, it enters an excited state and the de-excitation of this atom can be done in various ways for example, if the electron was from an outer-shell, the de-excitation results in the emission of a photon which can be in the visible range, this effect is called cathodoluminescence whereas, if the electron was from an inner-shell, the de-excitation can result with characteristic X-rays emission, or an Auger electron emission (Dinescu *et al*., 2013). The analysis of these signals can give quantitative and quality information on the composition of the sample (Dinescu *et al*., 2013).

# CHAPTER THREE

# MATERIALS AND METHODS

## 3.1 Research Design

Experimental research design was used in this study. From three rice mills in Mwea region, Kirinyaga County, Kenya, rice husks samples were purposely obtained. Laboratory procedures were followed for the extraction of silica by combustion and acid leaching. To synthesize SiNPs heat scavenger assisted magnesiothermic reduction of the silica obtained was carried out in a modified closed reactor. The synthesized SiNPs were then used to fabricate high performance Li-ion battery anodes. The extracted silica, synthesized SiNPs and the fabricated Li-ion battery anodes were characterized in terms of morphology, physical and electrochemical properties by SEM, EDX, FTIR, XRD and a Biologic VMP3 multichannel Potentiostat to determine its suitability for high performance Li-ion battery anodes.

## 3.2 Sampling Procedure and Pretreatment

Rice husks were randomly sampled from three rice mills in Mwea region, Kirinyaga County, Kenya. From each miller, one bag of ten kilograms of rice husks were collected, labeled and transported to Kenyatta University where a uniform mixture of these rice husks from the three millers was prepared for use. Random sampling was used because the millers obtain their rice from different farmers spread throughout the rice fields. The samples were washed with distilled water to remove dust and other adhering particles, oven dried at 110 °C for 12 hours, stored in plastic bags and designated as raw rice husks (RRH) ready for use. A sample of 700.0 g of the raw rice husks (RRH) was accurately weighed and refluxed with 500 ml of 3 M HCl solution in a 1000 ml Erlenmeyer flask for 1 hour and then left soaked in the acid solution for 11 hours to leach

metallic ions present. The pre-treated rice husks samples were collected by filtration, washed with distilled water before being oven dried at 110 °C for 24 hours. These samples were then designated as pre-treated rice husks (PTRH).

### 3.3 Chemicals and Reagents

The description of the chemicals and reagents used in this study is presented in table 3.1.

**Table 3.1: Descriptions of the Chemicals and Reagents Used.**

| Name | Company | Grade | Concentration or Assay |
|---|---|---|---|
| Aluminium foil | Aldrich | Not provided | Not provided |
| Carbon black | Signa-Aldrich | High purity | 99.95% |
| Copper foil | Aldrich | Not provided | Not provided |
| Ethylene Carbonate (EC) | Aldrich | Not provided | 98% |
| Hydrochloric acid | Loba Chemie | High purity | 36.5-38.0% |
| Lithium Cobalt Oxide **(**$LiCoO_2$), | Aldrich | Not provided | 99.8% |
| Lithium hexafluorophosphate ($LiPF_6$) | Aldrich | Not provided | 99.99% |
| Magnesium powder | Loba Chemie | Not provided | 99.0% |
| N-Methyl-2-Pyrrolidinone (NMP), | Sigma-Aldrich | Reagent plus | 99% |
| Polypropylene (separator) | Sigma-Aldrich | Not provided | Not provided |
| Polyvinylidene Fluoride (PVDF) | Aldrich | Not provided | Not provided |
| Sodium chloride | Sigma-Aldrich | ACS reagent | 99.0% |
| Vinylene Carbonate (VC) | Aldrich | Not provided | 97% |

### 3.4 Cleaning of Apparatus

Plastic and glassware apparatus were cleaned with liquid detergent, soaked in dilute nitric acid for 24 hours and rinsed with distilled water. Glassware was oven dried at 105 $^{o}$C while, plastic apparatus were air dried in a rack.

### 3.5 Extraction of Silica

To investigate the effect of acid pre-treatment on the silica content of rice husks ash obtained, 100.0 g samples of RRH were incinerated in a programmable muffle furnace to obtain raw rice husks ash (RRHA). The sample was incinerated with a ramp rate of 10 °C per minute and held at 600 °C for 5 hours, left overnight to cool in the furnace and then weighed using an analytical balance (model: Shimadzu ATX224), stored in a polythene bag and designated as raw rice husks ash (RRHA). At the same time a 100.0 g sample of pre-treated rice husks (PTRH) was also incinerated in the programmable muffle furnace to obtain pre-treated rice husks ash (PTRHA). The sample was incinerated with a ramp rate of 10 °C per minute and held at a temperature of 600 °C and for 5 hours, left overnight to cool in the furnace and then weighed using an analytical balance (model: Shimadzu ATX224), stored in a polythene bags and designated as pre-treated rice husks ash (PTRHA).

To investigate the effect of further acid leaching on the quality of pre-treated rice husks ash (PTRHA) obtained, 15.0 g sample of the PTRHA obtained by incinerating PTRH at 600 °C was subjected to further acid leaching by refluxing with 250 ml of 2 M HCl solution in a 500 ml Erlenmeyer flask for 1 hour then left soaked in the acid for 5 hours to leach the metallic ions inside. The leached rice husks ash was collected by filtration, washed with distilled water before being oven dried at 110 °C for 24 hours. This sample was then weighed using an analytical balance (model: Shimadzu ATX224), stored in a polythene bag and designated as leached rice husks ash (LRHA).

To further investigate the effect of thermal treatment on the silica content of pre-treated rice husks, samples of pre-treated rice husks were incinerated in a programmable muffle furnace to obtain pre-treated rice husks ash (PTRHA) samples. The samples was incinerated with a ramp rate of 10 °C per minute and held at varying temperatures of 600 °C, 700 °C, 800 °C, 900 and 1000 °C and for 5 hours, left overnight to cool in the furnace and weighed using an analytical balance (model: Shimadzu ATX224), stored in polythene bags and designated as pre-treated rice husks ash (PTRHA) samples.

**3.6 Synthesis of Silicon nanoparticles**

Silicon nanoparticles were prepared via a modified magnesiothermic reduction reaction (Luo *et al*., (2013). 9.0 g of the extracted silica sample was dispersed into an aqueous solution of sodium chloride under stirring at room temperature (Silica/NaCl: 1/10 % weight). The resultant mixture was heated to 60 $^{o}$C under vigorous stirring and then oven dried at 150 $^{o}$C to evaporate water. The silica/NaCl powder mixture (27.5 g) and 2.5 g of Mg powder were ground in a crucible and the resultant mixture Silica/NaCl/Mg (1/10/1 % weight/weight) transferred into a stainless steel modified closed reactor (appendix vi). The Silica/NaCl/Mg mixture in the modified closed reactor was incinerated in a programmable muffle furnace with a ramp rate of 10 $^{o}$C per minute for 1 hour and the temperature finally held at 650 $^{o}$C for 2 hours and left overnight in the furnace to cool.

After the temperature in the muffle furnace had dropped to room temperature, the samples obtained were immersed in water where the soluble sodium chloride filtrate was separated from the insoluble Si/MgO residue. This sodium chloride was recycled by drying the filtrate. The Si/MgO residues were then immersed in 1 M HCl solution for 6 hours to remove MgO. The

silicon nanoparticles residue obtained was washed with ethanol and oven-dried at a temperature of 60 $^{o}$C for 12 hours overnight. The silicon nanoparticles obtained were weighed using an analytical balance (model: Shimadzu ATX224) after cooling to room temperature, stored in a polythene bag and designated as silicon nanoparticles (SiNPs) ready for use.

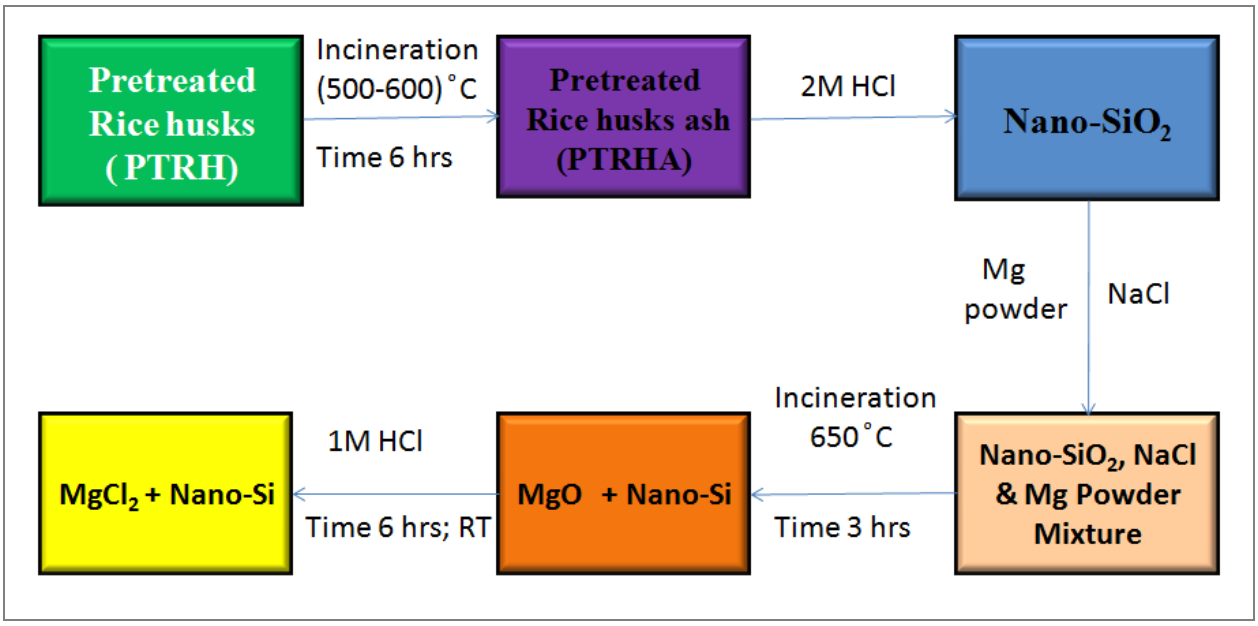


**Key:** RT - Room temperature, hrs - Hours

**Figure 3.1:** Schematic diagram for the synthesis of Silicon nanoparticles.

### 3.7 Electrode and Cell Fabrication

To prepare electrodes, a mixture of 65 % wt/wt SiNPs, 20 % wt/wt carbon black and 15 % wt/wt polyvinylidene fluoride was thoroughly ground to form homogeneous, black powder. The slurry containing this mixture in 1-methyl-2-pyrrolidinone was tightly rolled-pressed onto a 10 µm thin copper foil and dried. The SiNPs mass loading was typically 0.10 to 0.20 mg/cm$^2$. Prior to the cells being fabricated; the prepared electrodes were heated in a vacuum oven at 60 $^{o}$C for 2 hours. Coin type cells were fabricated inside an argon-filled glove box with the SiNPs as the working

electrode, Lithium Cobalt Oxide **(**$LiCoO_2$) foil as a counter electrode and polypropylene soaked in an electrolyte as a separator. The electrolyte was 1.0 M Lithium hexafluorophosphate ($LiPF_6$) in 1: 1 wt/wt Ethylene Carbonate. In order to improve cycling stability 1 % volume of vinylene carbonate was added to the Lithium hexafluorophosphate electrolyte. Cyclic voltammetry and electrochemical impedance spectroscopy measurements were done on a $VMP_2$ Biologic multichannel potentiostat.

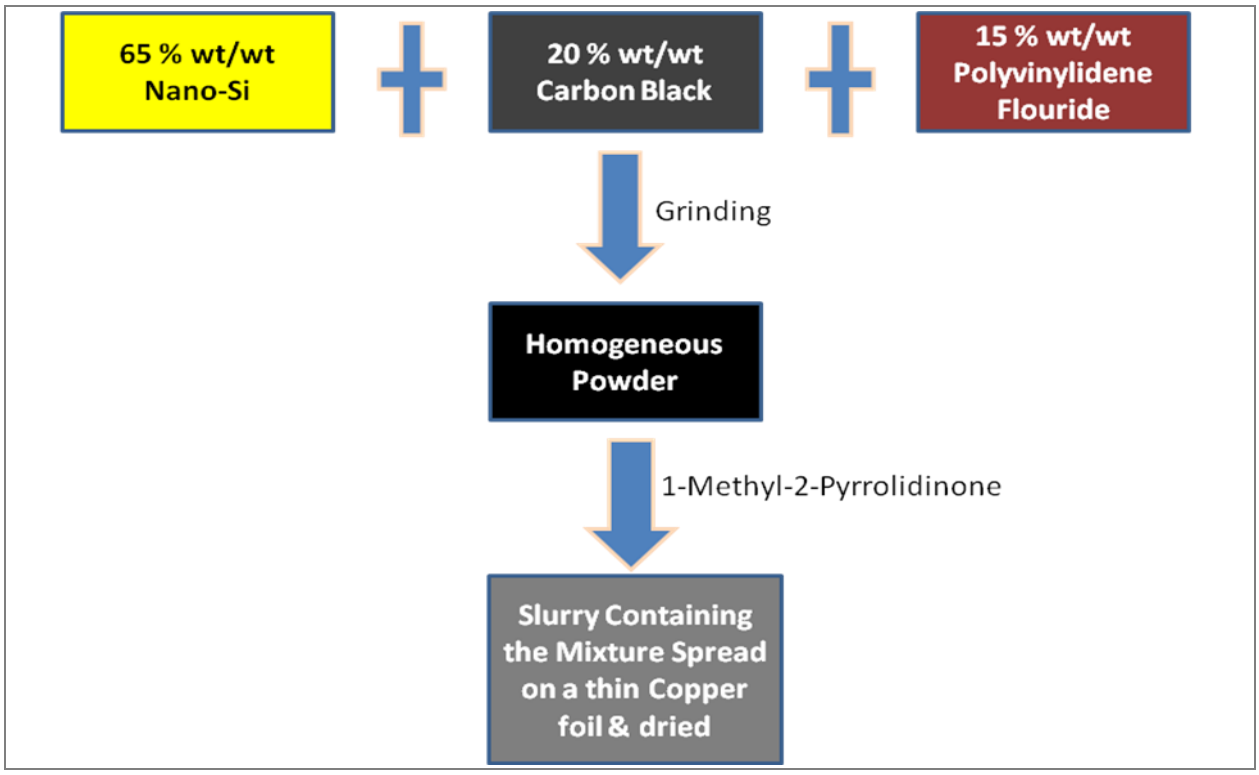


**Key:** %wt/wt – percent weight per weight

**Figure 3.2:** Schematic diagram for the fabrication of electrodes.

### 3.8 Physical and Chemical Measurements

#### 3.8.1 Fourier Transform Infrared (FTIR) Spectroscopy.

The major functional groups present in the extracted silica were identified by FTIR. The potassium bromide pressed disc technique was used to prepare samples for FTIR analysis. The most convenient method to prepare samples for FTIR spectroscopic analysis was to mix the sample with potassium bromide (KBr) and place the KBr/sample mixture into a dye under pressure to form a pellet (Djomgoue and Njopwouo, 2013). Approximately 1.2 mg of the extracted silica was mixed with 100.0 mg of KBr ground, pressed and dried. The pellets formed for this experiment were prepared using a screw press. The FTIR spectra were recorded in the range 400 $cm^{-1}$ to 4000 $cm^{-1}$, using a Shimadzu Fourier Transform Infrared Spectrophotometer (FTIR-8400s Model) and the results presented in figure 4.3 and appendix i.

#### 3.8.2 Energy Dispersive X-ray (EDX) Spectrometry.

EDX spectroscopy was used to determine the elemental composition of the extracted silica and the synthesized SiNPs. The samples were filled onto empty sample cups holders and placed in the appropriate slot in the Energy-dispersive X-ray (EDX) Spectrometer (Shimadzu 800HS Model) (appendix ii). Each sample was analyzed in triplicates and the results expressed as oxides presented in table 4.2, 4.3 and 4.4.

#### 3.8.3 X-Ray Diffraction (XRD) Analysis.

The structure of extracted silica and the synthesized SiNPs were characterized using X-Ray Diffraction (XRD. Samples were freeze dried for at least 12 hours before grinding to fine powder using mortar and pestle and transferred to an appropriate labeled glass bottle. The powdered

samples from the labeled sample bottle were then placed to fill an empty steel sample holder where any excess powder from the sample holder edges was removed and the sample carefully placed in the appropriate XRD slot. X-ray diffraction (XRD) patterns of the samples were obtained using a philips X'Pert (40 kV, 30 mA) X-ray diffractometer (Philips, Amsterdam, The Netherlands) (appendix iv). Scans were taken with $2\theta$ degree and a counting time of 1.00 s using a Cu-kα radiation source (λ=1.542 Å ) and a nickel filter. The diffraction angle was scanned from 10˚ to 60˚ $2\theta$ with a step size of 0.003. Each sample was analyzed in triplicates and the results obtained presented in figure 4.4, 4.5 and 4.12.

### 3.8.4 Scanning Electron Microscopy (SEM) Analysis

The morphology and structure of the synthesized SiNPs was analysed using scanning electron microscopy. A small amount of the synthesized SiNPs were placed on sample holders and loaded into SEM chamber to conduct material characterization studies. Carbon tapes were used for mounting the SiNPs samples. The scanning electron microscopy analysis was done on samples of extracted silica and the synthesized SiNPs using a Shimadzu SSX-550 model microscope (appendix v). The scanning electron microscope images a sample by scanning it with a high energy beam of electrons. The electrons interact with the atoms making up the sample thus producing signals that contains information about the sample's surface topography, elemental composition and other properties such as conductivity (KS and Pushpa, 2012). All the images were obtained under 15 kV at various amplifications and presented in figure 4.6, 4.7, 4.8, 4.12 and 4.15.

### 3.9 Electrochemical Measurements

To test the electrochemical properties, 10 coin-type cells were assembled in an argon-filled glove box. The cells were assembled by sandwiching separators (polypropylene) with the SiNPs electrodes (working electrodes) and lithium Cobalt oxide **(**$LiCoO_2$) (counter electrode). The electrochemical testing of the fabricated electrode was conducted primarily by galvanostatic measurements using VMP3 Multichannel Potentiostat (Biologic) whereas cyclic voltammetry measurements was done using a multi-channel battery tester (appendix vii, Neware multi-channel battery tester, China) in the potential range of 0.01 - 2.00 V at a scan rate of 0.5 mV $s^{-1}$.

#### 3.9.1 Cyclic Voltammetry

Cyclic voltammograms of the fabricated nanostructured silicon anodes were recorded on a Biologic VMP3 electrochemistry workstation (appendix viii). Cyclic voltammetry can give important information about the nature of the electrochemical alloying reactions that occur in the electrode. The voltage cutoffs were 0.01V and 2.00 V versus $Li/Li^+$. At certain voltages, peaks would be observed in the current response which could be attributed to specific electrochemical reactions that generate this current response. Thus, by studying the CV plot it was possible to identify the materials which alloys with lithium since different materials alloy with lithium at different electrochemical potentials. Cyclic voltammogram of the synthesized Li-ion battery anode cycled from 2.00 V to 0.01 V versus Li/Li+ at a scan rate of 0.5 mV s-1 is presented in figure 4.16.

#### 3.9.2 Charge/Discharge Cycling Test

The ass-assembled coin-type cells were cycled with a constant current density (200 mA/g) within fixed voltage limits of 0.01 V to 2.00 V at a scan rate of 0.5 mV $s^{-1}$. A multi-channel battery tester

(appendix vii, Neware multi-channel battery tester, China) was used for this test. The magnitude of the constant current was calculated based on the silicon content in each electrode. The specific capacity was calculated based on the mass of SiNPs. The charge and discharge rate was calculated with the theoretical specific charge capacity of silicon assumed to be 4200 mAh/g. The Coulombic efficiency was then calculated as $C_{dealloy}/C_{alloy}$, where $C_{dealloy}$ and $C_{alloy}$ are the capacity of the anode during lithium extraction and lithium insertion respectively. The specific charge capacity of the fabricated Li-ion battery anode is presented in figure 4.17.

# CHAPTER FOUR

# RESULTS AND DISCUSSION

## 4.1 Extraction of Silica.

Incineration of raw rice husks (RRH) and acid pre-treated rice husks (PTRH) samples at 600 $^{o}$C for 5 hours produced 24.20 % and 24.19 % of raw rice husks ash (RRHA) and pretreated rice husks ash (PTRHA) respectively (Table 4.1).

**Table 4.1:** Amount of Ash obtained from Rice Husks Incinerated at 600 $^{o}$C for 5 hours.

| Rice Husks Ash | Ash content (% wt ) |
|---|---|
| RRHA | 24.20 |
| PTRHA | 24.19 |

**Key:** RRHA - Raw Rice Husks Ash; PTRHA - Pretreated Rice Husks Ash.

An elemental analysis of the rice husks ash produced was done using Energy Dispersive X-ray (EDX) spectroscopy. The percentage of pure silica in RRHA and PTRHA was 95.962 (±0.454) % and 98.520 (±0.457) % respectively (Table 4.2). The main impurities present in this rice husks ash expressed as oxides were Mn, Ca, Fe, Zn, K, Rb and S. This proves that rice plants have naturally developed a process for the production of high-purity silica in their rice husks (Jung *et al*., 2013). This kind of substantially high percentage of silica intermingling with plant fibers is quite rare in nature (Ugheoke and Mamat, 2012). This findings are in agreement with the work of Ghosh and Bhattacherjee, (2013); who reported that rice husks on incineration yields 14 % to 20 % ash of which 80 % to 95 % constitutes silica in crystalline form with minor amounts of metallic elements. Silica purity of over 95 % resulting from the incineration alone is substantially higher than those of the other silica sources, such as diatomaceous earth, bentonite and quartz, which are prepared by similar procedures (Jung *et al*., 2013).

**Table 4.2: Elemental analysis of RRHA, PTRHA and LRHA samples by Energy-Dispersive X-ray (EDX) spectroscopy.**

| Component (oxides) | RRHA (% wt) | PTRHA (% wt) | LRHA (% wt) |
|---|---|---|---|
| **$SiO_2$** | 95.962 (±0.454) | 98.520 (±0.457) | 99.046 (±0.451) |
| **$K_2O$** | 1.231 (±0.014) | b.d | b.d |
| **$Na_2O$** | b.d | b.d | b.d |
| **MgO** | b.d | b.d | b.d |
| **$Fe_2O_3$** | 0.187 (±0.004) | 0.142 (±0.004) | 0.113 (±0.003) |
| **MnO** | 0.297 (±0.005) | b.d | b.d |
| **CaO** | 1.359 (±0.012) | 0.217 (±0.006) | 0.222 (±0.017) |
| **$Al_2O_3$** | b.d | b.d | b.d |
| **ZnO** | 0.013 (±0.001) | b.d | b.d |
| **$SO_3$** | 0.943 (±0.031) | 1.120 (±0.032) | 0.619 (±0.028) |
| **$Rb_2O$** | 0.008 (±0.000) | b.d | b.d |
| **$Co_2O_3$** | b.d | b.d | b.d |
| **$Sc_2O_3$** | b.d | b.d | b.d |
| **$Cr_2O_3$** | b.d | b.d | b.d |

**Key:** **b.d**-Below Detection Limit, **RRHA**-Raw Rice Husks Ash, **PTRHA**-Pre-Treated Rice Husks Ash, **LRHA**-Leached Rice Husks Ash, **% wt**-Percentage Weight.

Acid pre-treatment process of raw rice husks (RRH) with 3M HCl solution for 12 hours before incineration at 600 °C substantially decreased the amount of impurities present in pre-treated rice husks (PTRHA) to obtain silica whose percentage purity was 98.520 (±0.457) %. Further acid-leaching of the PTRHA samples with 2M HCl solution for 3 hours substantially decreased the level of the impurities present in the resultant leached rice husks ash (LRHA) samples. The percentage of pure silica in the LRHA samples was approximately 99.046 (±0.451) %. This decrease in impurities may be as a result of metals dissolving in the acidic solution and their subsequent removal by water washing and filtration. These results thus, show that acid pre-treatment of raw rice husks and further acid leaching of pre-treated rice husks ash samples was highly effective in reducing the concentration of metallic impurities present in rice husks and the

pre-treated rice husks ash respectively, to obtain highly pure silica. The decreased amount of impurities mainly results from the chemical reaction between acid and metals, where the reacted metals are leached from the acidic solution during the subsequent water washing and filtration (Liou and Wu, 2010; Rafiee *et al*., 2012).

The colour of PTRHA and LRHA was white (Figure 4.1: (b) and (c)). This is specifically because in processes where there has been significant leaching of the alkali metal oxides, especially the oxide of potassium, the brightness and whiteness of silica obtained increases (Ugheoke and Mamat, 2012). The alkali oxides promotes the surface melting of silica, thus entrapping carbon within the silica (Ugheoke and Mamat, 2012). The more this residual carbon is entrapped, the darker the color of the silica obtained (Ugheoke and Mamat, 2012).

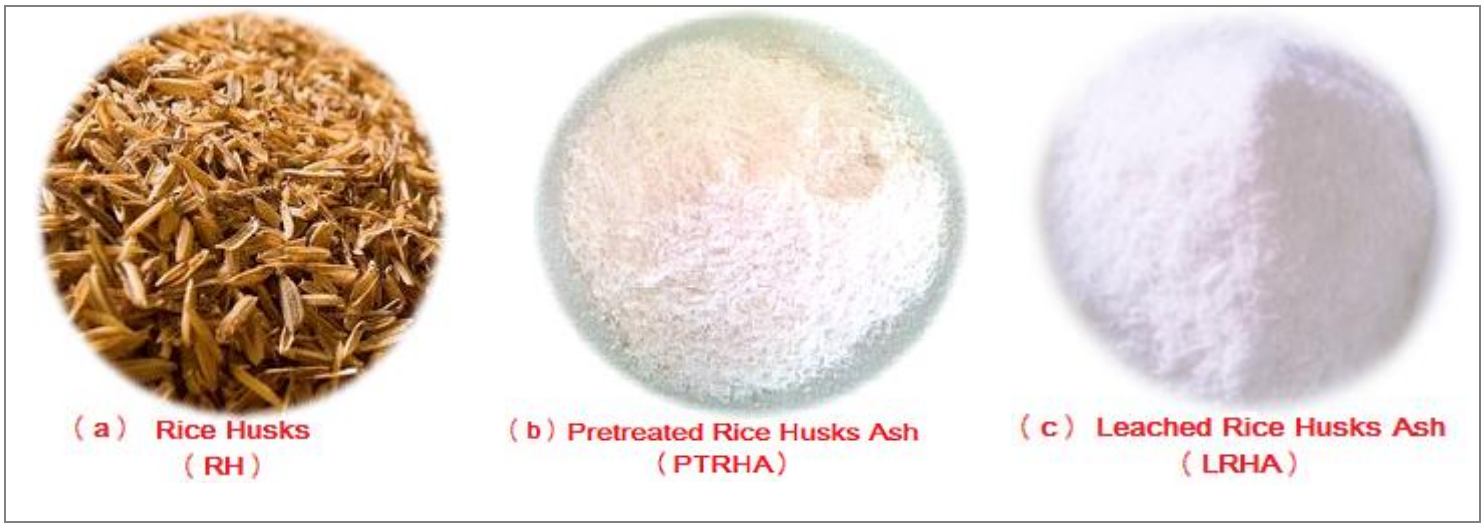


**Figure 4.1:** Rice Husks (a); Pre-treated Rice Husks Ash (b); Leached Rice Husks Ash (c).

**4.2 Effect of Incineration Temperature on the Percentage Purity of silica Obtained.**

The effect of incineration temperature on the quality of rice husks ash obtained was investigated by incinerating pre-treated rice husks (PTRH) samples at temperatures of 500 °C, 600 °C, 700 °C, 800 °C, 900 °C and 1000 °C for 5 hours. The colour of pre-treated rice husks ash (PTRHA) obtained at incineration temperature of 500 °C was grey, whereas that obtained at an incineration temperature of between 600 °C to 1000 °C was white (Figure 4.2). This findings is consistent with the observation noted by Ghosh and Bhattacherjee (2013); who reported that amorphous white silica (low-carbon) ash is obtained at incineration temperatures of above 500°C. Gu *et al*., (2013) also reported that the temperature of incineration is the most important determinant of the whiteness and silica content of the silica obtained.


**Figure 4.2:** Carbonised Rice Husks (a); Completely Incinerated Rice Husks (b).

## 4.3 Physical and Chemical Measurements of the Extracted Silica

### 4.3.1 Elemental Analysis

The chemical composition of PTRHA samples incinerated at temperatures of 600 °C, 700 °C, 800 °C, 900 °C and 1000 °C for 5 hours were analyzed using Energy-Dispersive X-ray (EDX) spectroscopy. The PTRHA samples obtained at a temperature of incineration of between 600 °C and 1000 °C were mainly composed of $SiO_2$, $K_2O$, $Fe_2O_3$, CaO and $SO_3$ with the major component of these PTRHA ashes being $SiO_2$ constituting over 98 % (Table 4.3). From the results it was noted that there is a slight decrease in the amount of inorganic impurities with increase in the temperature of incineration. This decrease in the amount of inorganic impurities in the rice husks ash with increase in temperature of combustion could probably be because some of the metals such as potassium were carried out with the volatiles during thermal decomposition. There being no significant change in the percentage purity of silica obtained by incinerating pre-treated rice husks at a temperature range of between 600 °C to 1000 °C the working temperature for the extraction of silica from rice husks was set at 600 °C.

**Table 4.3: Elemental analysis by Energy-Dispersive X-ray (EDX) spectroscopy of PTRHA samples incinerated at varying temperatures for 5 hours.**

| Component (oxides) | PTRHA-600 °C (%wt) | PTRHA-700 °C (%wt) | PTRHA-800 °C (%wt) | PTRHA-900 °C (%wt) | PTRHA-1000 °C (% wt) |
|---|---|---|---|---|---|
| **$SiO_2$** | 98.520 (±0.457) | 98.644 (±0.441) | 98.795 (±0.440) | 98.563 (±0.301) | 98.570 (±0.446) |
| **$K_2O$** | b.d | 0.089 (±0.089) | b.d | 0.127 (±0.007) | b.d |
| **$Na_2O$** | b.d | b.d | b.d | b.d | b.d |
| **MgO** | b.d | b.d | b.d | b.d | b.d |
| **$Fe_2O_3$** | 0.142 (±0.142) | b.d | 0.202 (±0.004) | b.d | 0.123 (±0.004) |
| **MnO** | b.d | b.d | b.d | b.d | b.d |
| **CaO** | 0.217 (±0.006) | 0.295 (±0.006) | 0.258 (±0.017) | 0.545 (±0.008) | 0.209 (±0.006) |
| **$Al_2O_3$** | b.d | b.d | b.d | b.d | b.d |
| **ZnO** | b.d | b.d | b.d | b.d | b.d |
| **$SO_3$** | 1.120 (±0.032) | 0.971 (±0.030) | 0.746 (±0.028) | 0.766 (±0.018) | 1.098 (±0.033) |
| **$Rb_2O$** | b.d | b.d | b.d | b.d | b.d |
| **$Co_2O_3$** | b.d | b.d | b.d | b.d | b.d |
| **$Sc_2O_3$** | b.d | b.d | b.d | b.d | b.d |

**Key: b.d**-Below Detection Limit, **PTRHA**-Pre-treated Rice Husks Ash, **%wt**-Percentage Weight.

### 4.3.2 FTIR Spectrophotometry

The major functional groups present in the silica extracted were identified by FTIR Spectrophotometry. The FTIR spectra of these rice husks ash samples were recorded in the range of between 400 $cm^{-1}$ and 4000 $cm^{-1}$. The FTIR spectrum of silica obtained by incineration of pre-treated rice husks at 1000 °C (Figure 4.3), shows bands at 470.6 $cm^{-1}$, 802.3 $cm^{-1}$, 1101.3 $cm^{-1}$, 1515.9 $cm^{-1}$, 1651.0 $cm^{-1}$, 2376.1 $cm^{-1}$, 3469.7 $cm^{-1}$, 3745.5 $cm^{-1}$, 3813.0 $cm^{-1}$ and 3855.4 $cm^{-1}$.

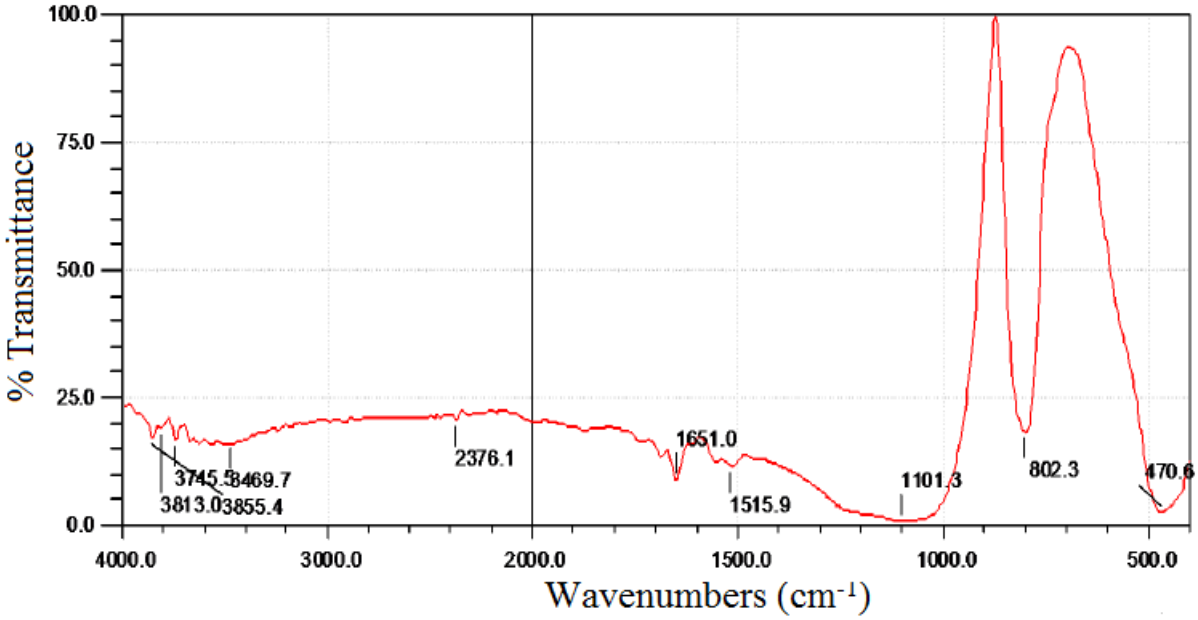


**Figure 4.3:** FTIR Spectrum of nano-silica Prepared at 1000 °C.

The band at 470.6 $cm^{-1}$ is due to a network O-Si-O bending vibration modes ( Javed *et al*., 2011; Rafiee *et al*., 2012; Okoronkwo *et al*., 2013). This confirms the formation of amorphous silica (Javed *et al*., 2011). The band at 1101.3$cm^{-1}$ is associated with the Si-O-Si (siloxane bonds) asymmetric stretching vibration, while the band at 802.3 $cm^{-1}$has been assigned to the network Si-O-Si symmetric bond stretching vibration ( Chen *et al*., 2010; Rafiee *et al*., 2012; Okoronkwo *et al*., 2013). A small band around 1,650 $cm^{-1}$ is assigned to the bending vibration of water molecules (O-H bending vibration) bound to the silica matrix (Chen *et al*., 2010; Rafiee *et al*., 2012). The small bands at 3410 $cm^{-1}$to 3470 $cm^{-1}$ is due to the stretching vibration of the O-H bond from the silanol groups (Si-OH) because of the adsorbed water molecules on the silica surface ( Rafiee *et al*., 2012; Okoronkwo *et al*., 2013). The absence of peaks between 2,800 $cm^{-1}$ and 3,000 $cm^{-1}$, implies that there is no original organic compounds in the silica after controlled combustion and extraction (Rafiee *et al*., 2012). The FTIR spectra's of rice husks ash obtained by

incineration at 600 °C, 700 °C, 800 °C and 900 °C (Appendix I); showed no noticeable changes in the position of the main peaks (470.6 $cm^{-1}$, 802.3 $cm^{-1}$ and 1101.3 $cm^{-1}$) from this of rice husks ash obtained by incineration at 1000 °C.

### 4.3.3 Structural Form Determination of the Extracted Silica.

The structure of the silica extracted was probed by powder X-ray diffraction (XRD). The diffractogram of silica obtained at 600 °C showed strong broad peaks at $2\theta$ = 22 ° (Figure 4.4). This confirms the formation of amorphous silica. These finding is in agreement with the work of Terzioğlu *et al*. (2013); who reported that silica found in husks incinerated at 400 °C to 600 °C has an almost completely amorphous structure. This naturally-inherited amorphous structure if retained meets the requirement of a stable anode to accommodate the volume change induced by lithium insertion and extraction. However, as temperature increases the transition to the crystalline form in the rice husks ash structure increases. The crystalline phase of the silica obtained at 1000 °C is evident from the sharp peaks observed at $2\theta$ = 22 ° (Figure 4.5). An XRD pattern showing a sharp peak at $2\theta$ = 22 ° corresponds to a cristobalite structure (Rafiee *et al*., 2012; Yuvakkumar *et al*., 2012). These findings are in agreement with the work of Ugheoke and Mamat, (2012), who studied the structural behaviour of silica over a temperature range of between 400 °C and 1500 $^{o}$C and reported that at a incineration temperature of over 900 °C, the silica obtained constituted mainly cristobalite and a small amount of tridymite. Terzioğlu *et al*., (2013) also noted that at 700 °C the cristobalite form begin to emerge, though slightly, along with the quartz structure; while at a temperature of between 800 °C to 900 °C, the cristobalite structure increased to a certain extent. The cristobalite is the more important crystalline phase in the ash obtained at 1000 °C.

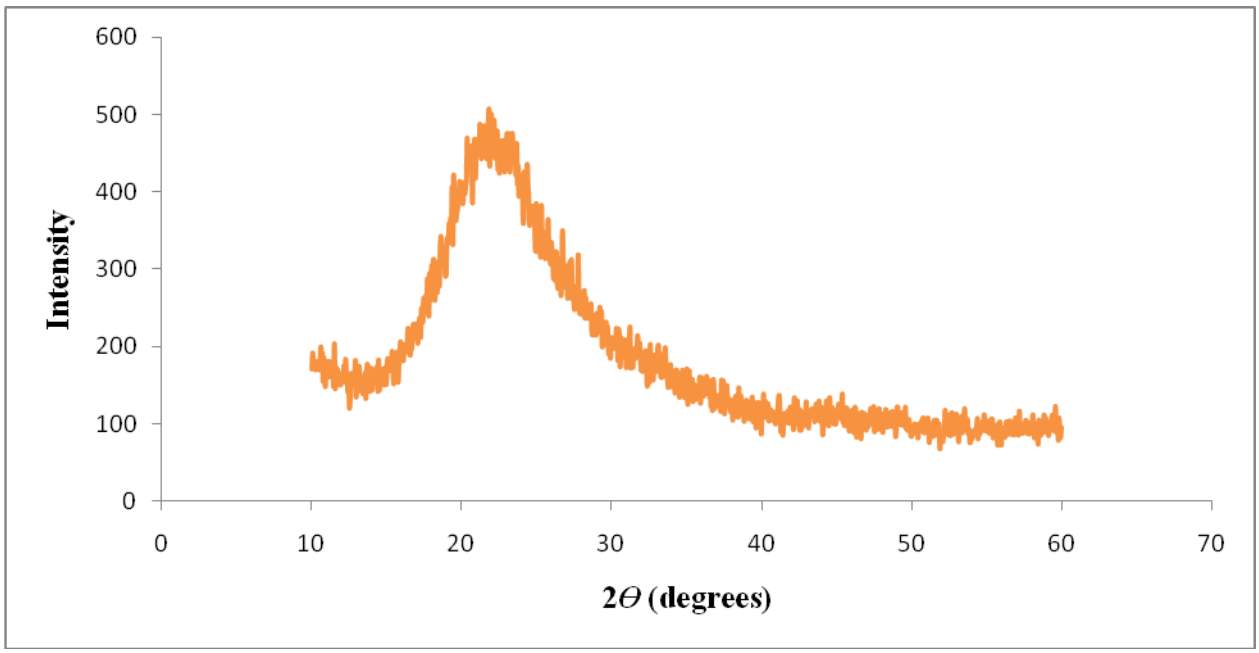


**Figure 4.4:** XRD diffractogram of silica prepared at 600 °C.

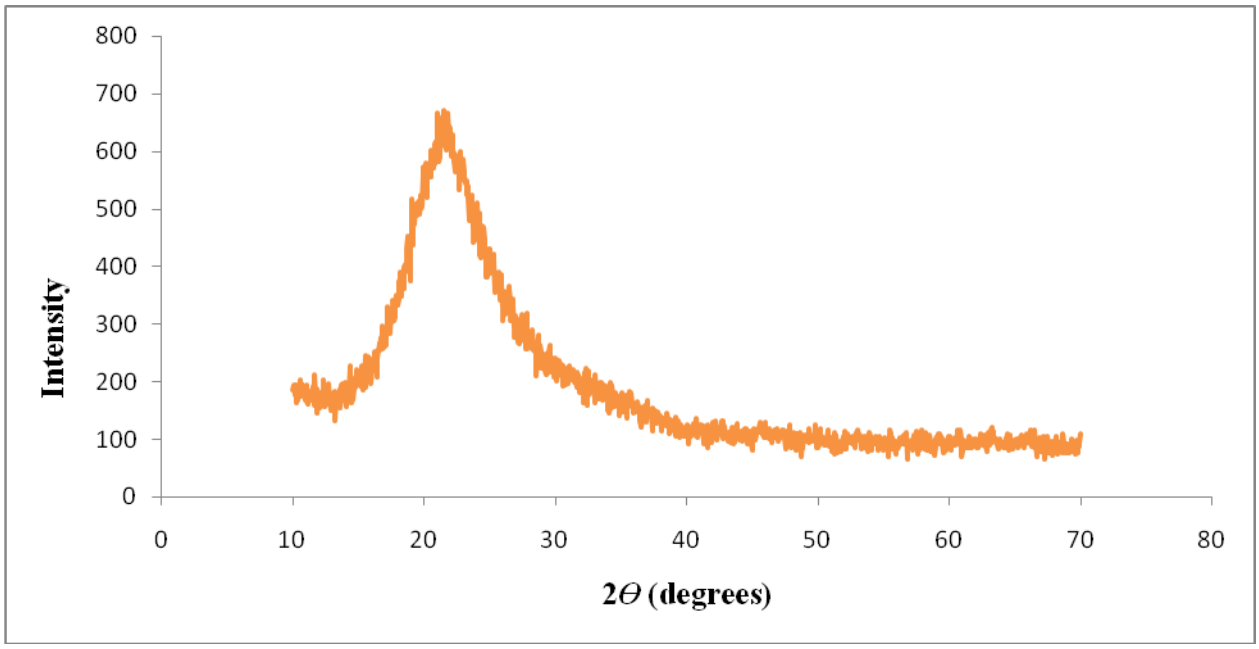


**Figure 4.5:** XRD diffractogram of silica prepared at 1000 °C.

### 4.3.4 Surface Morphology of the Extracted Silica.

Scanning Electron Microscopy (SEM) was used to investigate the morphology of the silica extracted. The SEM micrographs (Figure 4.6) show microstructure images of rice husks ash obtained at temperatures of between 600 °C to 1000 °C for 5 hours under varying magnification (56.28 kX to 75.55 kX). From the SEM micrograph of silica obtained at 600 °C and 800 °C (Figure 4.6: (a) and (b)), the silica obtained has spherical nanoparticles agglomerating into homogeneous porous structure. The presence of the nano-sized spherical particles leads to a highly porous structure due to aggregation of the particles (Hariharan and Sivakumar, (2013).

This naturally-inherited porous nanoparticle morphology if maintained during the synthesized of SiNPs meets the requirement of a stable anode to accommodate the large volume change induced by lithium insertion and extraction. From the SEM micrograph of pretreated rice husks ash samples prepared at 1000 °C, (Figure 4.6: (c)), most of the particles have merged resulting in a smooth surface of the silica obtained, thus, showing that an increase in incineration temperature causes the resultant silica coalesces resulting in collapsing of the porous nanoparticle morphology.

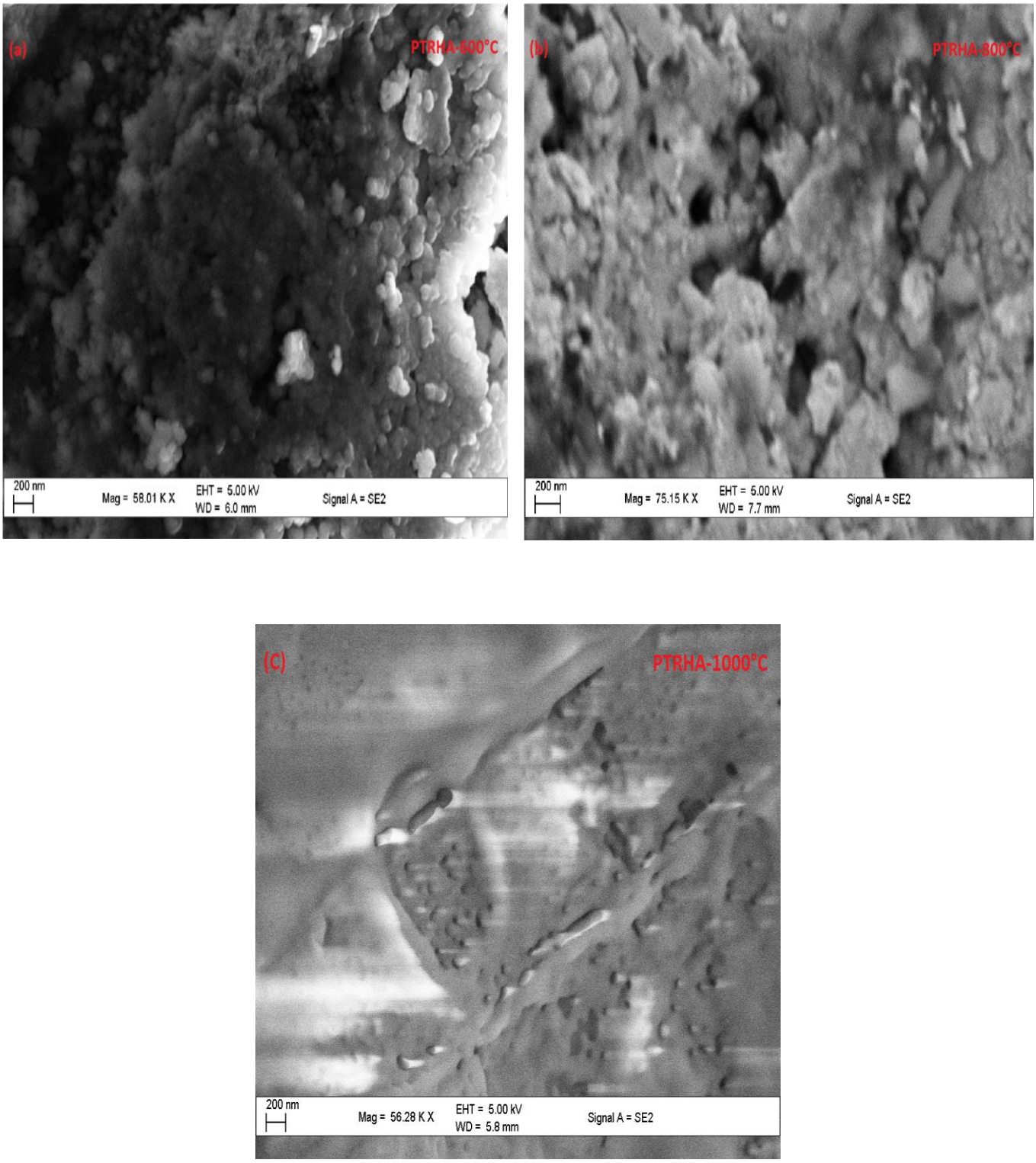


**Figure 4.6:** SEM microstructure images of pre-treated rice husks ash (PTRHA) samples prepared at: (a) 600 °C, (b) 800 °C and (c) 1000 °C.

To investigate the effect of different pretreatments of rice husks on the morphology of silica obtained, the morphological features of silica samples obtained from rice husks subjected to water washing (RRH) and acid pretreatment (PTRH), (Figure 4.7 (a) and (b) respectively), and incinerated at 600 °C for 5 hours, was studied. From the SEM microstructure image of PTRHA samples (Figure 4.7 (b)), the silica obtained has spherical nanoparticles agglomerating into homogeneous porous structure while in that of RRHA samples (Figure 4.7 (a)), majority of the particles have merged resulting in an almost smooth surface. This is mainly because of the effects of the metallic impurities present in the husks. The metallic impurities have a substantial effect on the quality of silica derived from rice husks, with potassium mainly causing surface melting, accelerating the crystallization of amorphous silica and resulting in carbon fixation in rice husks (RHA) (Rafiee *et al*., 2012).

Further acid leaching of pretreated rice husks ash (PTRHA) obtained 600 °C was to done to obtain leached rice husks ash (LRHA) in an effort to reduce the percentage of residual metals by the formation of water-soluble metal chlorides. This was critical in preserving the original porous nanostructure. In that there exists a strong interaction between oxides, especially those of K and Na contained in rice husks and the silica therein, such that it can result in the surface melting of silica particles and accelerate an early crystallisation of amorphous silica into cristobalite (Ugheoke and Mamat, 2012). From the SEM micrograph of LRHA samples (Figure 4.7 (c)), the silica obtained had uniform and highly porous structure. This highly porous structure is desirable for high performance Li-ion battery anodes.

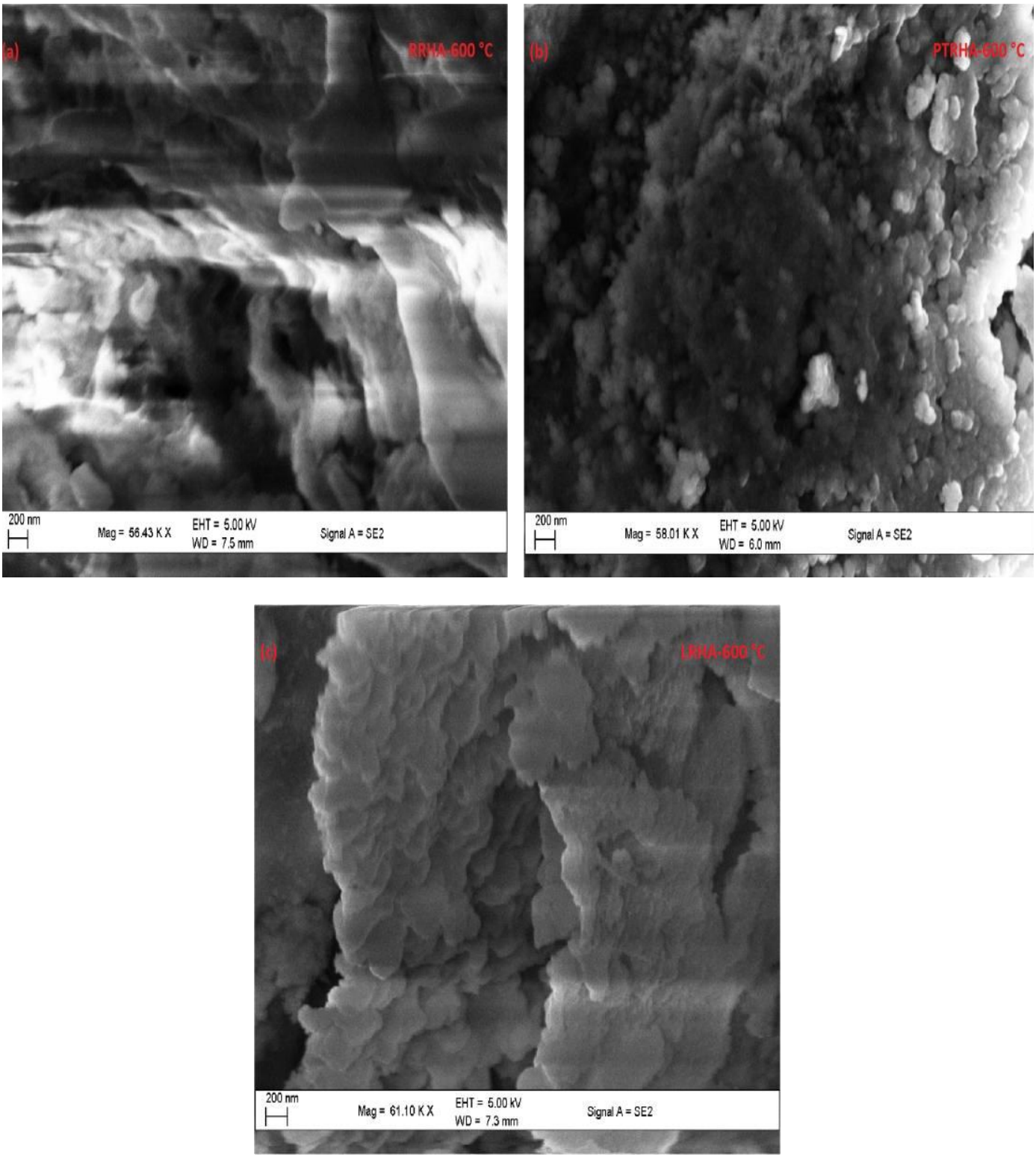


**Figure 4.7:** SEM micrograhs of Silica prepared at 600 °C: (a) Raw Rice Husks Ash (RRHA), (b) Pre-treated Rice Husks Ash (PTRHA) and (c) Leached Rice Husks Ash (LRHA).

Numerous SEM microstructural views of LRHA samples under varying magnification (9.16 kX to 131.89 kX) (Figure 4.8) were obtained. From these micrographs it is evident that the extracted silica samples exhibits a porous structure. The porous nanostructure was mainly because the resultant silica retained its original cellular skeleton structure in rice husks, which originates naturally from the loose aggregation of primary silica nanoparticles (Chen, *et al*., 2013). A Microscopic characterization of rice husks derived silica using SEM, done by Jung *et al*. (2013), similarly reported that rice husks derived silica exists in the form of nanoparticles that are interconnected to make up a porous nanostructure.

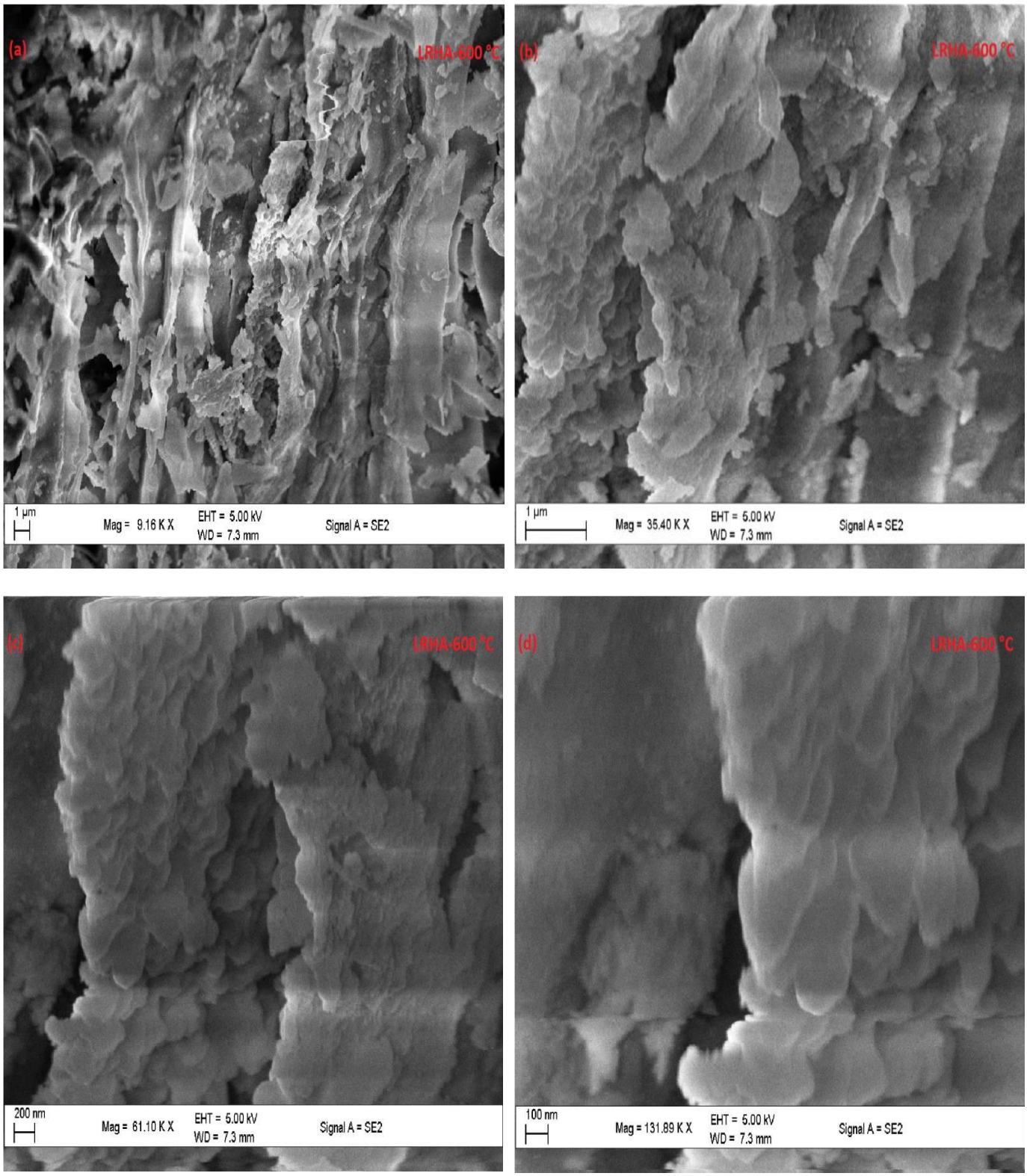


**Figure 4.8:** SEM micrographs of LRHA samples under different magnifications: (a) 9.16 kX, (b) 35.40 kX, (c) 61.10 kX, (d) 131.89 kX.

### 4.4 Synthesis of Silicon Nanoparticles (SiNPs)

In an effort to transfer the original porous structure exhibited by the rice husks originated silica to the synthesized silicon nanoparticles, heat scavenger assisted magnesiothermic reduction of silica (Figure 4.9) was carried out at a temperature of 650 °C for 5 hours in a modified closed reactor (Appendix vi).

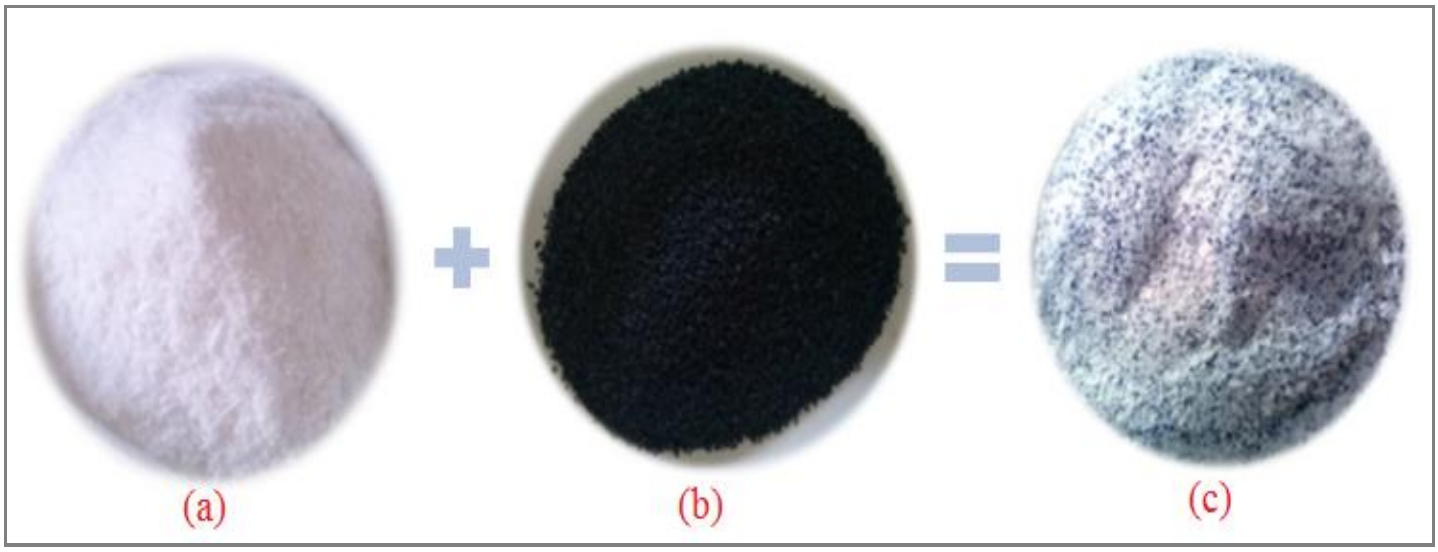


**Figure 4.9:** (a) Silica/NaCl Mixture (1:10 % wt), (b) Magnesium powder, (c) Silica/NaCl/Mg Mixture (1:10:1 % wt).

In this heat scavenger assisted magnesiothermic reduction process, silicon nanoparticles (Figure 4.10: (b)), were obtained through the reaction represented by equation (4.1):

$$Mg_{(g)} + SiO_{2\,(s)} \longrightarrow 2MgO_{(s)} + Si_{(s)} \qquad (4.1)$$

In magnesiothermic reduction process, solid magnesium whose boiling point is 650 °C, functions as a reducing agent that evaporates first and then diffuse into silica (Jung *et al*., 2013; Liu *et al*., 2013). The gaseous Mg is able to access to the surfaces deep inside silica samples because they possess a porous structure and subsequently a uniformly distributed MgO/Si mixture was obtained (Figure 4.10: (a)). After selective removal of MgO from the resultant MgO/Si mixture

by acid leaching, silicon nanoparticles (Figure 4.10: (b)) were obtained. The yield of the synthesized SiNPs was 2.370 g.


**Figure 4.10:** (a) Si/MgO mixture; (b) Synthesized Silicon nanoparticles.

### 4.5 Characterization of Silicon Nanoparticles (SiNPs) obtained Rice Husks

The chemical composition, structure and morphology of the synthesized SiNPs were determined using various analytical tools. The chemical composition was analysed by Energy-Dispersive X-ray (EDX) spectroscopy. Scanning Electron Microscopy (SEM) was used to determine the morphology whereas the crystal structure was probed using X-ray diffraction (XRD).

#### 4.5.1 Elemental Analysis by Energy-Dispersive X-ray (EDX) spectroscopy

The chemical composition of the synthesized SiNPs was analysed by Energy-Dispersive X-ray (EDX) spectroscopy. Six metals Fe, Ca, S, Co, Sc and Si were simultaneously detected by the Energy-Dispersive X-ray (EDX) spectrometer, the purity of the synthesized SiNPs was found to

be 98.794 %, further confirming the formation of pure phase Si (Table 4.4). The impurity with the highest concentration was Ca and whose peak overlapped with that of S to give a concentration of 0.435 % whereas Fe, Co and Sc were all under 0.234 (±0.006) %. Co and Sc which were not initially detected in the leached rice husks ash (LRHA) were probably introduced during the heat scavenger assisted magnesiothermic reduction, since the sodium chloride reagent and magneiusm powder used were not analytical grade. These impurities could be reduced or avoided by employing an analytical grade magnesium reagent and analytical grade sodium chloride (heat scavenger) coupled with additional acid leaching of the synthesized silicon Nanoparticles (SiNPs).

**Table 4.4: Chemical composition analysis of the synthesized Silicon nanoparticles by EDX.**

| Element | Percentage Weight (% wt) |
|---|---|
| **Si** | 98.794 (±0.335) |
| **K** | b.d |
| **Na** | b.d |
| **Mg** | b.d |
| **Fe** | 0.234 (±0.006) |
| **Mn** | b.d |
| **Ca** | 0.353 (±0.008) |
| **Al** | b.d |
| **Zn** | b.d |
| **S** | 0.435 (±0.026) |
| **Rb** | b.d |
| **Co** | 0.042 (±0.004) |
| **Sc** | 0.143 (±0.005) |

**Key:** b.d – below detection limit

From the EDX spectrum obtained (Figure 4.11); it can be clearly seen that the synthesized SiNPs were highly pure with minute traces of impurities. Even though this SiNPs were recovered

directly from rice husks, its purity of over 98 % is sufficient for its application in high performance Li-ion battery anodes. Impurities are at times added (doping) to improve the electrical conductivity of the nanostructured silicon (Liu *et al*., 2013). In other applications of this nanostructured silicon such as in solar cells, the impurity level must be much lower. This can possibly be realized by using an analytical grade Mg reagent together with additional acid pre-treatment and acid leaching of the RHs and the MgO/Si mixture respectively.

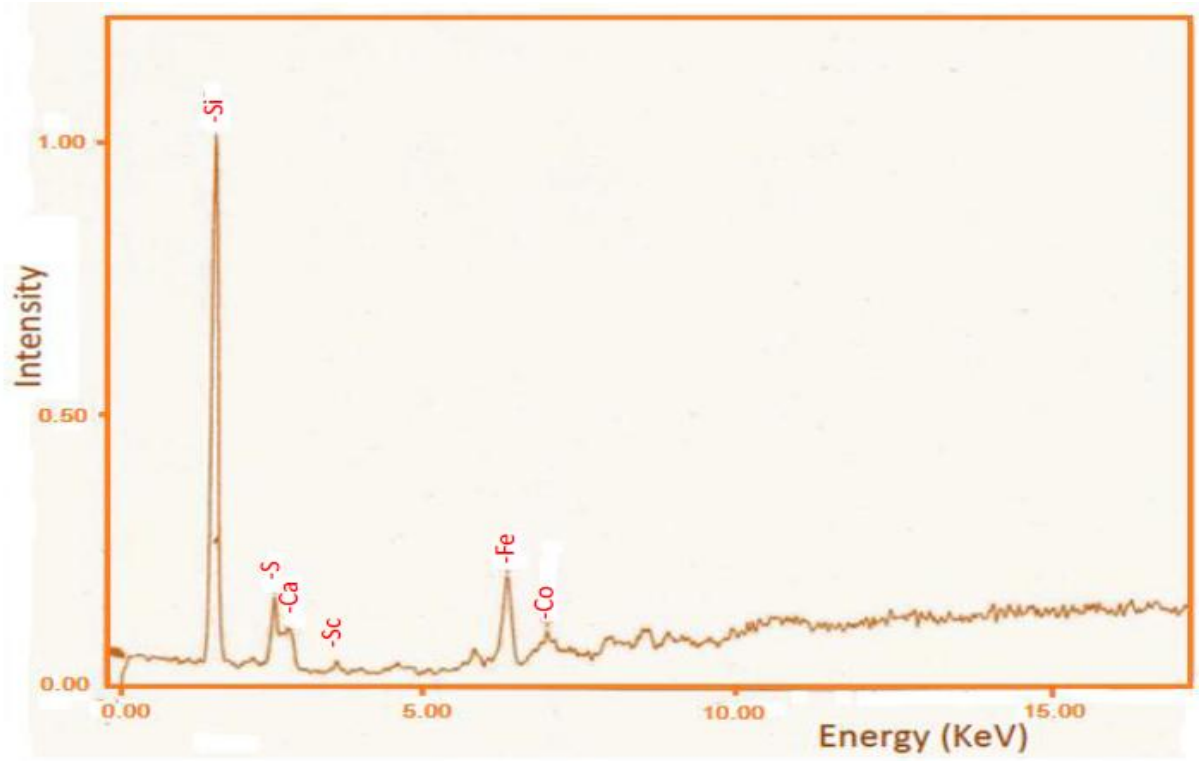


**Figure 4.11:** EDX spectrum of the synthesized Silicon nanoparticles.

### 4.5.2 XRD Analysis

The crystal structure and phase of the synthesized SiNPs was probed using X-ray diffraction (XRD) was used. The crystalline phase of the synthesized SiNPs is evident from the sharp diffraction peaks that are observed in the XRD diffractogram (Figure 4.12). These findings are in

agreement with the work of Yuvakkumar *et al*., (2012) who reported that sharp diffraction peaks observed at 2$\theta$ degree on an XRD diffractogram reveals the formation of cristobalite structures. A comparison of the XRD pattern obtained with the standard powder diffraction pattern of Silicon (JCPDS No. 27-1402) (Figure 4.13) and (ICDD File: 271402) (Figure 4.14), in the Joint Committee on Powder Diffraction Standards (JCPDS) file and the International Center for Diffraction Data file respectively, further proved that the synthesized product was that of pure silicon nanoparticles, since all the major lattice orientations of all the peaks marched that of pure silicon.

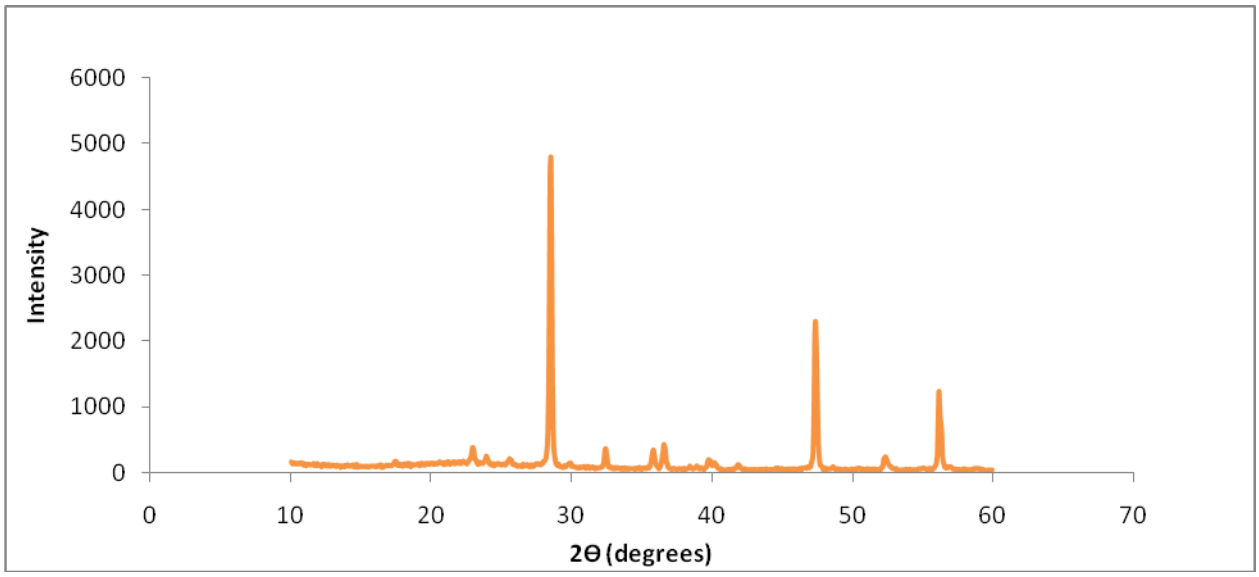


**Figure 4.12:** XRD diffractogram of the synthesized Silicon nanoparticles.

The Bragg's peaks of the synthesized SiNPs was indexed using both (JCPDS No. 27-1402) and (ICDD File: 271402), this readily indexed it to the cubic phase of silicon. The three pairs of diffraction peaks in the vicinity of 28 °, 47 ° and 55 ° in the XRD diffractogram of SiNPs in

figure 4.12; was thus assigned to the reflections of (111), (220) and (311) planes of Si (Luo *et al*., 2013).

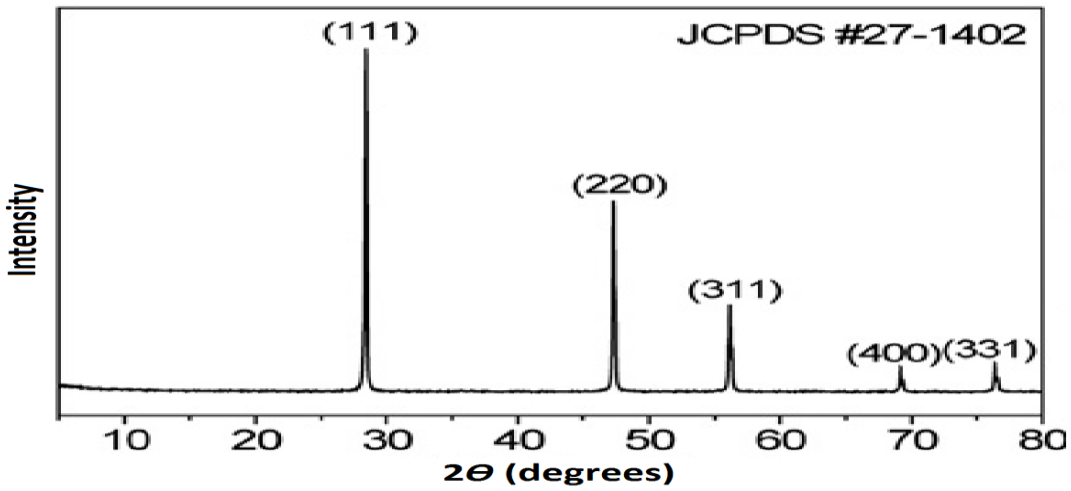


**Figure 4.13:** Standard XRD spectra of Si (JCPDS No. 27-1402), with the major lattice orientations denoted (Jung *et al*., 2013).

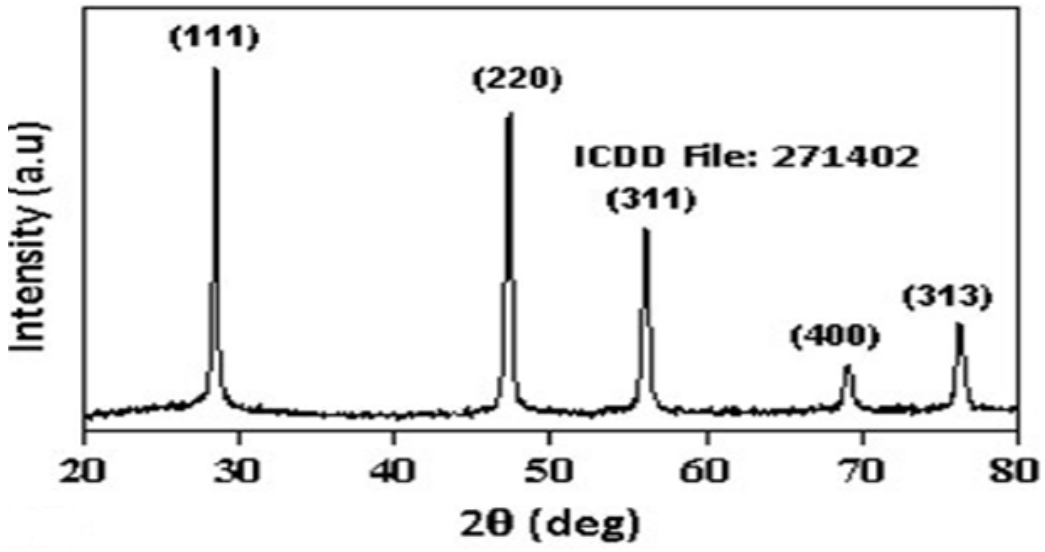


**Figure 4.14:** XRD pattern of Si nanopowder (ICDD File: 271402) (Kumar *et al*., 2012).

### 4.5.3 SEM Analysis

The morphology of the synthesized SiNPs samples was determined by Scanning Electron Microscopy (SEM). From the SEM micrographs (Figure 4.15) of the synthesized SiNPs exhibit a porous structure, confirming that this synthesized SiNPs retained similar morphology to that of rice husks originated silica. It also confirms that the heat scavenger (NaCl), in the magnesiothermic reaction effectively scavenges the heat released in the exothermic reaction, which effectively prevents the collapse of the nanostructure and further aggregation of the silicon domains. This naturally occurring nanoporous particle morphology readily meets the requirement of a stable silicon anode that can accommodate the volume changes induced by lithium insertion and extraction during charging and discharge respectively.

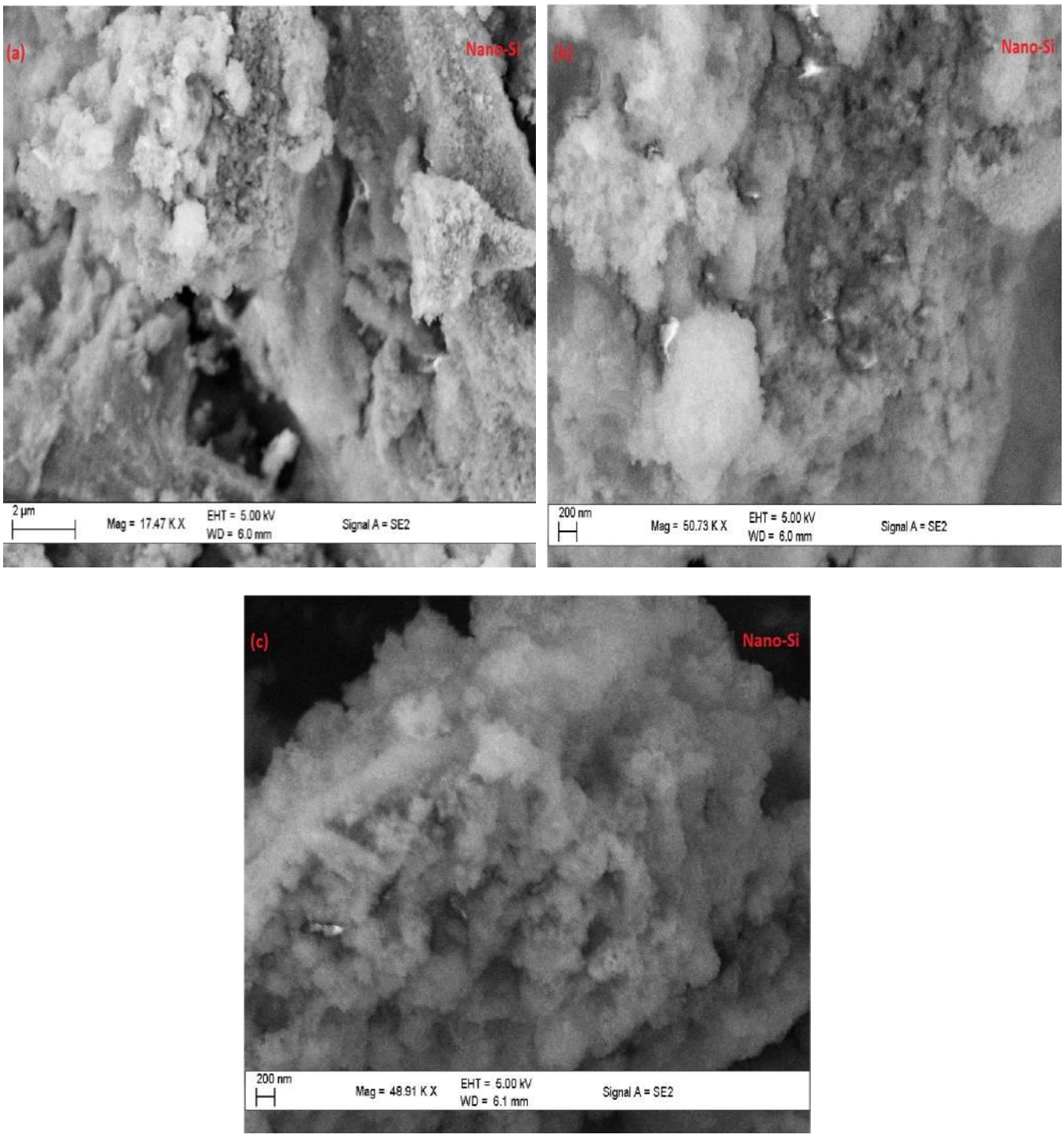


**Figure 4.15:** SEM micrographs of the synthesized Silicon nanoparticles under different magnifications: (a) 17.47 kX, (b) 50.73 kX, (c) 48.91 kX.

### 4.6 Electrochemical Performance and Cyclic Voltammetry Measurements

To test the electrochemical properties of the fabricated Li-ion battery anodes, 10 coin-type cells were assembled in an argon-filled glove box. The cells were assembled by sandwiching separators (polypropylene) with the SiNPs electrodes (working electrodes) and lithium Cobalt oxide ($LiCoO_2$) (counter electrode). The electrochemical testing of the fabricated electrode was conducted primarily by galvanostatic measurements using VMP3 Multichannel Potentiostat (Biologic) whereas cyclic voltammetry measurements was done using a multi-channel battery tester (appendix vii) in the potential range of 0.01 to 2.00 V at a scan rate of 0.5 mV $s^{-1}$.

#### 4.6.1 Cyclic Voltammetry Test

From the cyclic voltammogram obtained (Figure 4.16); it can be deduced that a number of reversible reactions occur during cycling. From the first half-cycle (Li-ion insertion), a peak was observed around 1.375V, this peak was attributed to the formation of Solid Electrolyte Interface (SEI) film. This peak was found to have disappeared in the subsequent cycles. This is in agreement with the work of Tocoglu *et al*. (2015) who noted that the peaks which belong to SEI formation disappear at following cycles because of its irreversible nature. SEI is an electronic insulator passive layer and lithium ion conductor (Tocoglu *et al*., 2015). This phenomenon thus accounts for the initial low coulombic efficiency (CE) in the galvanostatic charge and discharge tests. The one additional peak appearing near 0.15V in the subsequent cycles was assigned to the formation of Li-Si alloys.

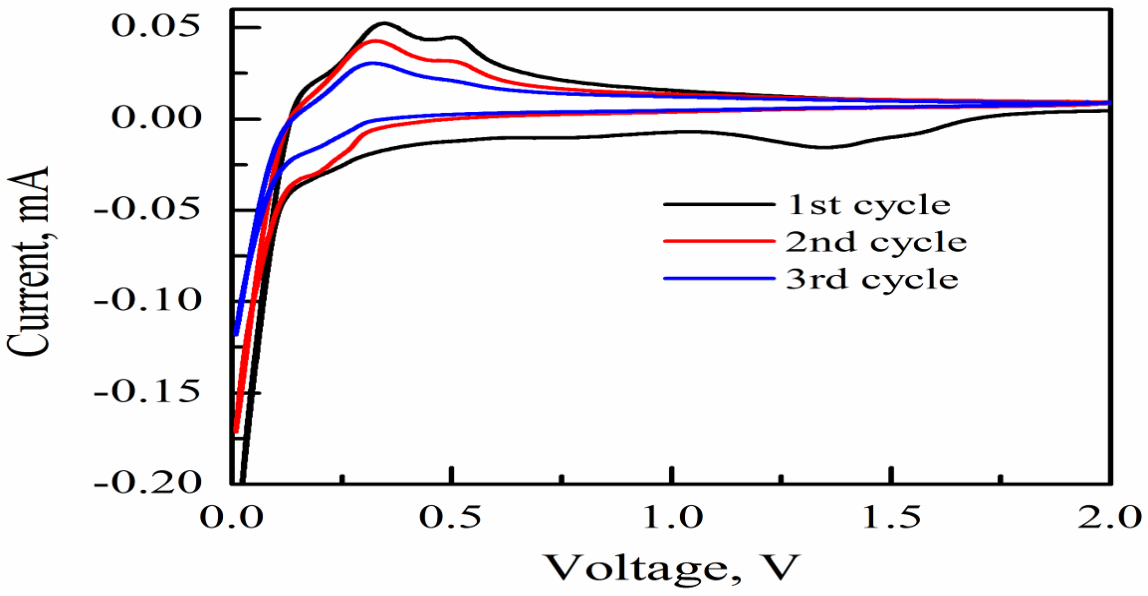


**Figure 4.16:** Cyclic voltammogram of Li-ion battery anode using nano-Si recovered from RHs cycled from 2.00 V to 0.01 V versus Li/Li+ at a scan rate of 0.5 mV $s^{-1}$.

The two broad anodic peaks occurring at around 0.35V and 0.55V corresponds to the phase transition between Li-Si alloys and Si. These findings are in agreement with the work of Tocoglu *et al*. (2015) who reported that the cathodic peak below the 0.30 V is as a result of reversible lithiation reactions whereas at anodic section of the voltammogram peaks at 0.30 - 0.40 V could be attributed to reversible decomposition reactions of lithium and silicon alloys. Chen *et al*. (2012) also reported that the two distinct peaks at 0.37 and 0.54 V which appears in the first reverse anodic scan, are attributable to the reaction between amorphous $Li_xSi$ and amorphous silicon. Thus, from the cyclic voltammogram (Figure 4.16) it can thus be concluded that lithiation and delithiation peaks occurred at potential ranges typical of the reaction of silicon since no other peaks were detected in the potential range scanned, this also indicates that the fabricated electrode was electrochemically inactive between 0.01 to 2.0.V.

### 4.6.2 Galvanostatic Charge and Discharge Cycling Tests

The specific charge capacity of the fabricated electrode was calculated based on the mass of SiNPs (typically 0.10 to 0.20 mg/cm$^2$) and the theoretical capacity of silicon taken to be 4,200 mA h g$^{-1}$. Upon deep galvanostatic cycling done between 0.01 V and 2.00V, the discharge (delithiation) capacity reached 2,732 mA hg$^{-1}$ for the first cycle and stabilized at around 1250 mA hg$^{-1}$ for the subsequent cycles (Figure 4.17). These values are approximately seven and three times respectively the theoretical specific charge capacity of graphite (372 mA hg$^{-1}$). After nine cyclic voltammetry (CV) cycles, the cyclic voltammetric profiles became stable (Figure 4.17), implying that the activation was complete and the electrode reacts fully. It was thus concluded that the synthesized SiNPs lithium ion battery anode exhibited excellent electrochemical behaviour without any further modification or coating.

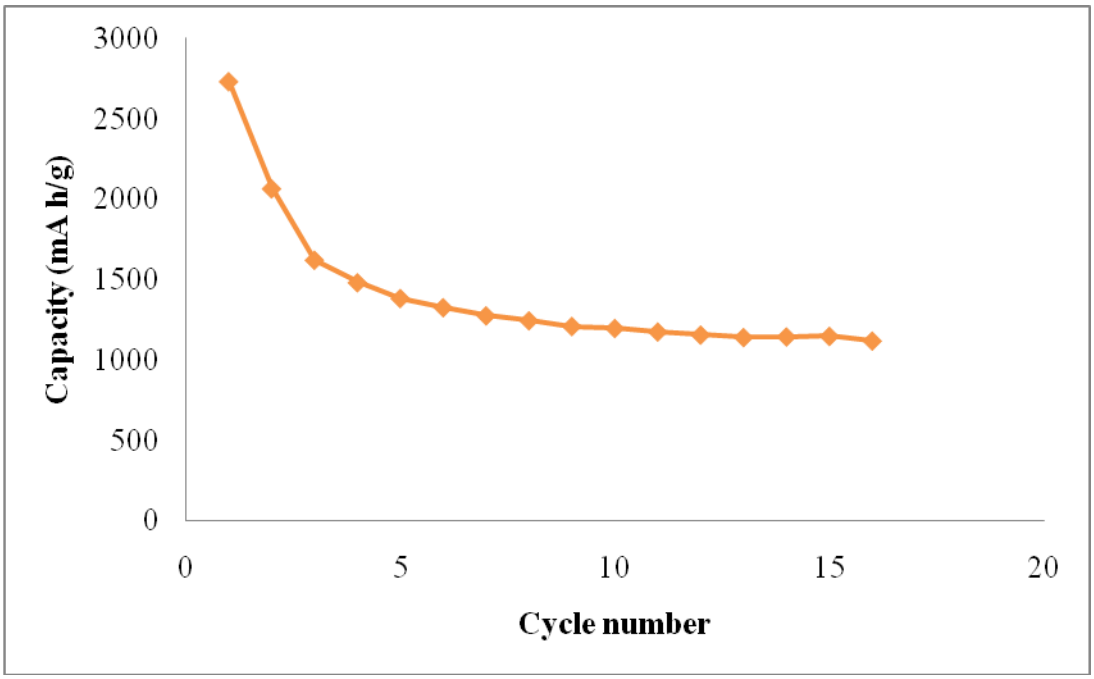


**Figure 4.17:** Specific capacity of Li-ion battery anode using SiNPs recovered from RHs.

The Coulombic efficiency (CE), which is an indicator of SEI formation and stability in anodes (Liu *et al*., 2013), was as high as 97.20 % when averaged from the 3$^{rd}$ to the 16$^{th}$ cycle (Figure 4.17). In the first cycle CE was 75.55 %, this was mainly because the lithiation of the native oxide and the initial SEI formation consumes some lithium. The coulombic efficiency of the first cycle can be increased by performing prelithiation (Liu *et al*., 2013). From the results it was also noted that the highly porous structure allowed room for volume expansion of Si without rupturing the solid-electrolyte interphase (SEI) at the outer surface. Thus, instead of repetitively breaking and reforming SEI during extended cycling, a thin and stable SEI conformally covered the surface of the nanostructured silicon electrode, resulting in its high reversibility and therefore good cycling stability (Liu *et al*., 2013). From cyclic voltammetry experiments and galvanostatic cycling measurements of these nanostructured silicon anodes (Figure 4.16 and Figure 4.17**)**, it was concluded that the fabricated anodes showed remarkable specific charge capacity values and exhibited a much higher charge capacity compared to that of the commercially available graphite anodes even after 16 charge and discharge cycles.

# CHAPTER FIVE

# CONCLUSIONS AND RECOMMENDATIONS

## 5.1 Conclusions

The findings of this study are useful for scientists pursuing new synthetic route for highly valuable and widely applicable silicon nanomaterials. It is very promising that continuous development of these and other strategies to obtain silicon nanomaterials will lead to the practical applications of nanostructured silicon anodes in commercial lithium ion battery technology. The results of this work indicate that rice husks derived nanostructured silicon is a promising anode material for high performance lithium ion battery anodes. From the results the following conclusions were made.

(i) It was feasible to synthesize silicon nanoparticles of high purity from rice husks. Rice husks contain sufficient amounts of highly valuable inorganic silica. The silica extracted from rice husks was highly pure (approximately 99%), existed in amorphous state and had a uniform and highly porous structure. Heat scavenger assisted magnesiothermic reduction of silica was highly effective in preserving the original porous nanostructure exhibited by silica in the SiNPs obtained.

(ii) The synthesized SiNPs exhibited a porous structure, existed in a crystalline state and had high purity of 98 %. The uniquely small crystallite size and porous nature of the SiNPs derived here gave it superior performance as a lithium-ion battery anode over commercially available graphite anodes.

(iii)The fabricated electrode showed superior electrochemical performance over commercially available graphite anodes, by exhibiting high specific charge capacity of 2732 mA h/g, which was seven times greater than the theoretical capacity of graphite anodes (372 mA $hg^{-1}$), with a high coulombic efficiency in first cycle and good cycle and rate performance (97.20 % capacity retention after 16 cycles). Thus, the results indicate that the prepared nanostructured silicon electrode is a promising anode material for high performance lithium-ion battery anode.

**5.2 Recommendations**

From the initial results the prepared nanostructured silicon electrode is a promising anode material for high performance lithium-ion batteries. Since the fabricated electrode showed good electrochemical performance by not only exhibiting high specific charge capacity with a high coulombic efficiency in first cycle but also good cycle and rate performance. However, to further enhance the specific charge capacity and improve the cycling stability more work should be done including:

(i) Optimizing the weight ratio of silica, sodium chloride and magnesium in the magnesiothermic reduction reaction, this would give the optimum weight ratio necessary to minimize the porous structure collapse in the synthesized silicon nanoparticles.

(ii) More work should be done in order to get the optimum weight ratio of silicon nanoparticles, carbon black (conductive addiditive) and polyvinylidene fluoride (binder). The different weight ratio of silicon nanoparticles and carbon black may show different effect on the

electrochemical performance of the fabricated anode by enhancing the specific charge capacity and overcoming the cycling stability issue.

(iii) The irreversible capacity loss of the fabricated battery anodes should be estimated from an evaluation of half cells and full cells using known cathode materials over a significantly larger number of cycles is necessary.

(iv) Finally the purity of silicon nanoparticles obtained here may not ordinarily meet solar grade requirement but is generally of much higher purity than that of metallurgical grade silicon, thus this SiNPs recovered may be used as a high quality feedstock in the processing of solar grade silicon by including some additional refining steps.

## REFERENCES

Berthomieu, C., and Hienerwadel, R. (2009). Fourier transform infrared (FTIR) spectroscopy. *Photosynthesis Research*, **101** (2–3): 157–170.

Bogner, A., Jouneau, P.-H., Thollet, G., Basset, D., and Gauthier, C. (2007). A history of scanning electron microscopy developments: towards "wet-STEM" imaging. *Micron*, **38** (4), 390–401.

Bruce, P. G., Scrosati, B., and Tarascon, J.-M. (2008). Nanomaterials for Rechargeable Lithium Batteries. *Angew. Chem. Int. Ed*, **47**, 2930 – 2946. DOI : 10.1002/anie.200702505.

Chan, C. K., Peng, H., Liu, G., McIlwrath, K., Zhang, X. F., Huggins, R. A., and Cui, Y. (2008). High-performance lithium battery anodes using silicon nanowires. *Nature Nanotechnology*, **3** (1), 31–35. https://doi.org/10.1038/nnano.2007.411.

Chauhan, A., and Chauhan, P. (2014). Powder XRD Technique and its Applications in Science and Technology. *Journal of Analytical and Bioanalytical Techniques*, **5** (6), 1. https://doi.org/10.4172/2155-9872.1000212.

Chen, D., Mei, X., Ji, G., Lu, M., Xie, J., Lu, J., and Lee, J. Y. (2012). Reversible Lithium-Ion Storage in Silver-Treated Nanoscale Hollow Porous Silicon Particles. *Angewandte Chemie International Edition*, **51** (10), 2409–2413.

Chen, H., Wang, F., Zhang, C., Shi, Y., Jin, G., and Yuan, S. (2010). Preparation of nano-silica materials: The concept from wheat straw. *Journal of Non-Crystalline Solids*, **356** (50), 2781–2785.

Chen, H., Wang, W., Martin, jarett C., Oliphant, A. J., Doerr, P. A., Xu, J. F., … Sun, L. (2013). Extraction of Lignocellulose and Synthesis of Porous Silica Nanoparticles from Rice Husks: A Comprehensive Utilization of Rice Husk Biomass - *ACS Sustainable Chemistry and Engineering (ACS Publications)* **1** (2), 254-259. http://pubs.acs.org/doi/full/10.1021/sc300115r.

Chen, J. (2013). Recent Progress in Advanced Materials for Lithium Ion Batteries. *Materials*, **6** (1), 156–183. http://doi.org/10.3390/ma6010156.

Chen, X., Gerasopoulos, K., Guo, J., Brown, A., Wang, C., Ghodssi, R., and Culver, J. N. (2011). A Patterned 3D Silicon Anode Fabricated by Electrodeposition on a Virus-Structured Current Collector. *Advanced Functional Materials*, **21** (2), 380–387. http://doi.org/10.1002/adfm.201001475.

Chen, Z. W., Gibson, W. M., and Huang, H. (2008). High Definition X-Ray Fluorescence: Principles and Techniques. *X-Ray Optics and Instrumentation*, *2008*, 1–10. http://doi.org/10.1155/2008/318171.

Cortadellas, N., Fernández, E., and Garcia, A. (2012). Biomedical and Biological Applications of Scanning Electron Microscopy. *Centres Científics I Tecnològics. Universitat de Barcelona*. http://hdl.handle.net/2445/31943.

Davis, R., and Mauer, L. J. (2010). Fourier transform infrared (FT-IR) spectroscopy: a rapid tool for detection and analysis of foodborne pathogenic bacteria. *Current Research, Technology and Education Topics in Applied Microbiology and Microbial Biotechnology*, **2**, 1582–1594.

Dinescu, L., Dinica, M., Miron, C., and Barna, E. S. (2013). The approach of teaching and learning scanning electron microscope in high school using virtual experiments. *Romanian Reports in Physics*, **65** (2), 578–590.

Djomgoue, P., and Njopwouo, D. (2013). FT-IR Spectroscopy Applied for Surface Clays Characterization. *Journal of Surface Engineered Materials and Advanced Technology*, **3** (4), 275–282. http://doi.org/10.4236/jsemat.2013.34037.

Dorofeev, G. A., Streletskii, A. N., Povstugar, I. V., Protasov, A. V., and Elsukov, E. P. (2012). Determination of nanoparticle sizes by X-ray diffraction. *Colloid Journal*, **74** (6), 675–685. http://doi.org/10.1134/S1061933X12060051.

Ghosh, R., and Bhattacherjee, S. (2013). A Review Study on Precipitated Silica and Activated Carbon from Rice Husk. *Journal of Chemical Engineering & Process Technology*, **04** (04). https://doi.org/10.4172/2157-7048.1000156.

Gu, S., Zhou, J., Luo, Z., Wang, Q., and Ni, M. (2013). A detailed study of the effects of pyrolysis temperature and feedstock particle size on the preparation of nanosilica from rice husk. *Industrial Crops and Products*, **50**, 540–549.

Guo, Y.-G., Hu, J.-S., and Wan, L.-J. (2008). Nanostructured Materials for Electrochemical Energy Conversion and Storage Devices. *Advanced Materials*, **20** (15), 2878–2887.

Han, G. S., Li, B., Ye, Z. Q., Cao, C. H., and Guan, S. Y. (2012). The Cooperative Effect of Vinylene Carbonate and 1, 3-Propane Sultone on the Elevated Temperature Performance of Lithium Ion Batteries. *Int. J. Electrochem. Sci*, **7**, 12963–12973.

Hariharan, V., and Sivakumar, G. (2013). Studies on synthesized nanosilica obtained from bagasse ash. *International Journal of Chemical Technology and Research*, **5** (2), 1263–1266.

Jenkins, R. (2006). X-Ray Techniques: Overview. *Encyclopedia of Analytical Chemistry*. http://onlinelibrary.wiley.com/doi/10.1002/9780470027318.a6801/full.

Jung, D. S., Ryou, M.-H., Sung, Y. J., Park, S. B., and Choi, J. W. (2013). Recycling rice husks for high-capacity lithium battery anodes. *Proceedings of the National Academy of Sciences*, **110** (30), 12229–12234. http://doi.org/10.1073/pnas.1305025110.

Kaech, A. (2013). An Introduction to Electron Microscopy Instrumentation, Imaging and Preparation. *Center for Microscopy and Image Analysis, University of Zurich*. http://www.zmb.uzh.ch/static/bio407/assets/Script_AK_2014.pdf.

Kasavajjula, U., Wang, C., and Appleby, A. J. (2007). Nano- and bulk- silicon-based insertion anodes for lithium-ion secondary cells. *Journal of Power Sources*, **163** (2), 1003–1039.

Khondker, A., and Lakhani, S. (2015). X-Ray Diffraction: A Comprehensive Explanation for Multipurpose Research. *International Journal of Interdisciplinary Research and Innovations*, **3** (1), 60–64.

Krumeick, F. (2011). Properties of electrons, their interactions with matter and applications in electron microscopy. *Laboratory of Inorganic Chemistry*. Http://www. Microscopy. Ethz. ch/downloads/Interactions. Pdf, Consultado Em, 3–8.

KS, T. R., and Pushpa, A. (2012). Studies on characterizations of agri-culture waste (rice husk) for the production of ethanol. *Journal of Environmental Research And Development*, **7** (2A). http://www.jerad.org/ppapers/dnload.php?vl=7andis=2Aandst=1076.

Kumar, S. M., Murugan, K., Chandrasekhar, S. B., Hebalkar, N., Krishna, M., Satyanarayana, B. S., and Madras, G. (2012). Synthesis and characterization of nano silicon and titanium nitride powders using atmospheric microwave plasma technique. *Journal of Chemical Sciences*, **124** (3), 557–563.

Landi, B. J., Ganter, M. J., Cress, C. D., DiLeo, R. A., and Raffaelle, R. P. (2009). Carbon nanotubes for lithium ion batteries. *Energy and Environmental Science* (RSC Publishing), **2** (6), 638-654. DOI:10.1039/B904116H.

Lavina, B., Dera, P., & Downs, R. T. (2014). Modern X-ray diffraction methods in mineralogy and geosciences. *Reviews in Mineralogy and Geochemistry*, **78** (1), 1–31.

Liou, T.-H., and Wu, S.-J. (2010). Kinetics Study and Characteristics of Silica Nanoparticles Produced from Biomass-Based Material. *Industrial and Engineering Chemistry Research* (ACS Publications), **49** (18), 8379-387. http://pubs.acs.org/doi/abs/10.1021/ie100050t.

Liu, N., Huo, K., McDowell, M. T., Zhao, J., and Cui, Y. (2013). Rice husks as a sustainable source of nanostructured silicon for high performance Li-ion battery anodes. *Scientific Reports*, **3**. http://doi.org/10.1038/srep01919.

Luo, W., Wang, X., Meyers, C., Wannenmacher, N., Sirisaksoontorn, W., M. Lerner, M., and Ji, X. (2013). Efficient fabrication of nanoporous Si and Si/Ge enabled by a heat scavenger in magnesiothermic reactions. *Scientific Reports*, **3**.

McDowell, M. T., Lee, S. W., Nix, W. D., and Cui, Y. (2013). 25th Anniversary Article: Understanding the Lithiation of Silicon and Other Alloying Anodes for Lithium-Ion Batteries. *Advanced Materials*, **25** (36), 4966–4985. http://doi.org/10.1002/adma.201301795.

Monshi, A., Foroughi, M. R., and Monshi, M. R. (2012). Modified Scherrer Equation to Estimate More Accurately Nano-Crystallite Size Using XRD. *World Journal of Nano Science and Engineering*, **2** (3), 154–160. http://doi.org/10.4236/wjnse.2012.23020.

Naqvi, H. J., Saeed, A., Umair, A., & Shah, F. H. (2011). Precipitated Silica from Wheat Husk. *Journal of the Pakistan Institute of Chemical Engineers*, **39** (1), 51–54.

Odo, E. A., Britton, D. T., Gonfa, G. G., and Harting, M. (2012). Structure and characterization of silicon nanoparticles produced using a vibratory disc mill. *The African Review of Physics*, **7**. http://forum.aphysrev.org/index.php/aphysrev/article/viewArticle/525.

Okoronkwo, E. A., Imoisili, P. E., and Olusunle, S. O. O. (2013). Extraction and characterization of amorphous silica from corn cob ash by sol-gel method. *Chemistry and Materials Research*, **3** (4), 68–72.

Park, M.-H., Kim, M. G., Joo, J., Kim, K., Kim, J., Ahn, S., … Cho, J. (2009). Silicon Nanotube Battery Anodes. *Nano Letters* (ACS Publications) **9** (11), 3844-3847. http://pubs.acs.org/doi/abs/10.1021/nl902058c.

Quercia, G., Lazaro, A., Geus, J. W., and Brouwers, H. J. H. (2013). Characterization of morphology and texture of several amorphous nano-silica particles used in concrete. *Cement and Concrete Composites*, **44**, 77–92. http://doi.org/10.1016/j.cemconcomp.2013.05.006.

Rafiee, E., Shahebrahimi, S., Feyzi, M., and Shaterzadeh, M. (2012). Optimization of synthesis and characterization of nanosilica produced from rice husk (a common waste material). *International Nano Letters*, **2** (1), 1–8. http://doi.org/10.1186/2228-5326-2-29.

Rao, C. N. R., and Biswas, K. (2009). Characterization of Nanomaterials by Physical Methods. *Annual Review of Analytical Chemistry*, **2** (1), 435–462. http://doi.org/10.1146/annurev-anchem-060908-155236.

Rasel Das, M., Ali, E., and Hamid, S. B. A. (2014). Current applications of x-ray powder diffraction - a review. *Rev. Adv. Mater. Sci*, **38**, 95–109.

Shaikh, I. R., and Shaikh, A. A. (2013). Utilization of Wheat Ash as Silica Source for the Synthesis of MCM-41 Type Mesoporous Silicates:A Sustainable Approach towards Valorization of the Agricultural Waste Stream. *Research Journal of Chemical Sciences*, **3** (11), 66-72. ISSN 2231-606X.

Singh, D., Kumar, R., Kumar, A., and Rai, K. N. (2008). Synthesis and characterization of rice husk silica, silica-carbon composite and $H_3PO_4$ activated silica. *Cerâmica*, **54** (330), 203-212.

Singh, L. P., Agarwal, S. K., Bhattacharyya, S. K., Sharma, U., and Ahalawat, S. (2011). Preparation of silica nanoparticles and its beneficial role in cementitious materials. *Nanomaterials and Nanotechnology*, **1** (1), 44–51.

Spolnik, Z., Belikov, K., Meel, K. V., Adriaenssens, E., Roeck, F. D., and Grieken, R. V. (2005). Optimization of Measurement Conditions of an Energy Dispersive X-ray Fluorescence Spectrometer with High-Energy Polarized Beam Excitation for Analysis of Aerosol Filters. *Applied Spectroscopy*, **59** (12), 1465–1469.

Stadtländer, C. (2007). Scanning electron microscopy and transmission electron microscopy of mollicutes: challenges and opportunities. *Modern Research and Educational Topics in Microscopy*, **1**, 122–131.

Stutzman, P. (2004). Scanning electron microscopy imaging of hydraulic cement microstructure. *Cement and Concrete Composites*, **26** (8), 957–966.

Suga, M., Asahina, S., Sakuda, Y., Kazumori, H., Nishiyama, H., Nokuo, T., … others. (2014). Recent progress in scanning electron microscopy for the characterization of fine structural details of nano materials. *Progress in Solid State Chemistry*, **42** (1), 1–21.

Szczech, J. R., and Jin, S. (2011). Nanostructured silicon for high capacity lithium battery anodes. *Energy and Environmental Science* (RSC Publishing), **4** (1), 56-72. http://pubs.rsc.org/en/content/articlelanding/2011/ee/c0ee00281j.

Tarascon, J.-M., and Armand, M. (2001). Issues and challenges facing rechargeable lithium batteries. *Nature*, **414** (6861), 359–367.

Teki, R., Datta, M. K., Krishnan, R., Parker, T. C., Lu, T.-M., Kumta, P. N., & Koratkar, N. (2009). Nanostructured silicon anodes for lithium ion rechargeable batteries. *Small*, **5** (20), 2236–2242.

Terzioğlu, P., Yucel, S., Rabagah, T. M., & Özçimen, D. (2013). Characterization of wheat hull and wheat hull ash as a potential source of $SiO_2$. *BioResources*, **8** (3), 4406–4420.

Theivasanthi, T., and Alagar, M. (2010). X-ray diffraction studies of copper nanopowder. *arXiv Preprint arXiv:1003.6068*. http://arxiv.org/abs/1003.6068.

Tocoglu, U., Cevher, O., and Akbulut, H. (2015). Cyclic Performance Tests of Si/MWCNT Composite Lithium Ion Battery Anodes at Different Temperatures. *Acta Physica Polonica A*, **127** (4), 1059–1061. http://doi.org/10.12693/APhysPolA.127.1059.

Ugheoke, I. B., and Mamat, O. thman. (2012). A Critical assessment and new research directions of rice husk silica processing methods and properties. *Maejo International Journal of Science and Technology*, **6** (03), 430-448. http://www.mijst.mju.ac.th/vol6/430-448.pdf.

Wang, W., and Kumta, P. N. (2010). Nanostructured Hybrid Silicon/Carbon Nanotube Heterostructures: Reversible High-Capacity Lithium-Ion Anodes. *ACS Nano*, **4** (4), 2233–2241.. http://pubs.acs.org/doi/abs/10.1021/nn901632g.

Wobrauschek, P., Streli, C., & Selin Lindgren, E. (2010). Energy Dispersive, X-Ray Fluorescence Analysis. *Encyclopedia of Analytical Chemistry*. http://onlinelibrary.wiley.com/doi/10.1002/9780470027318.a6806.pub2/full.

Wollman, D. A., Irwin, K. D., Hilton, G. C., Dulcie, L. L., Newbury, D. E., and Martinis, J. M. (1997). High-resolution, energy-dispersive microcalorimeter spectrometer for X-ray microanalysis. *Journal of Microscopy*, **188** (3), 196–223.

Wong, D. H. C., Thelen, J. L., Fu, Y., Devaux, D., Pandya, A. A., Battaglia, V. S., … DeSimone, J. M. (2014). Nonflammable perfluoropolyether-based electrolytes for lithium batteries. *Proceedings of the National Academy of Sciences*, **111** (9), 3327–3331. http://doi.org/10.1073/pnas.1314615111.

Wu, H., and Cui, Y. (2012). Designing nanostructured Si anodes for high energy lithium ion batteries. *Nano Today*, **7** (5), 414–429.

Wu, H., Zhuo, D., Kong, D., and Cui, Y. (2014). Improving battery safety by early detection of internal shorting with a bifunctional separator. *Nature Communications*, **5**, 5193. http://doi.org/10.1038/ncomms6193.

Yuvakkumar, R., Elango, V., Rajendran, V., and Kannan, V. (2012). High-purity nano silica powder from rice husk using a simple chemical method. *Journal of Experimental Nanoscience*, **9** (3), 272-281. DOI: 10.1080/17458080.2012.656709.

Zhang, Y., Ghaly, A. E., and Li, B. (2012). Physical properties of wheat straw varieties cultivated under different climatic and soil conditions in three continents. *American Journal of Engineering and Applied Sciences*, **5** (2), 98-106. ISSN: 1941-7020.

# APPENDICES

## APPENDIX I: FTIR SPECTRA

### Appendix IA: FTIR Spectrum of Raw Rice Husks Ash Prepared at 600 °C

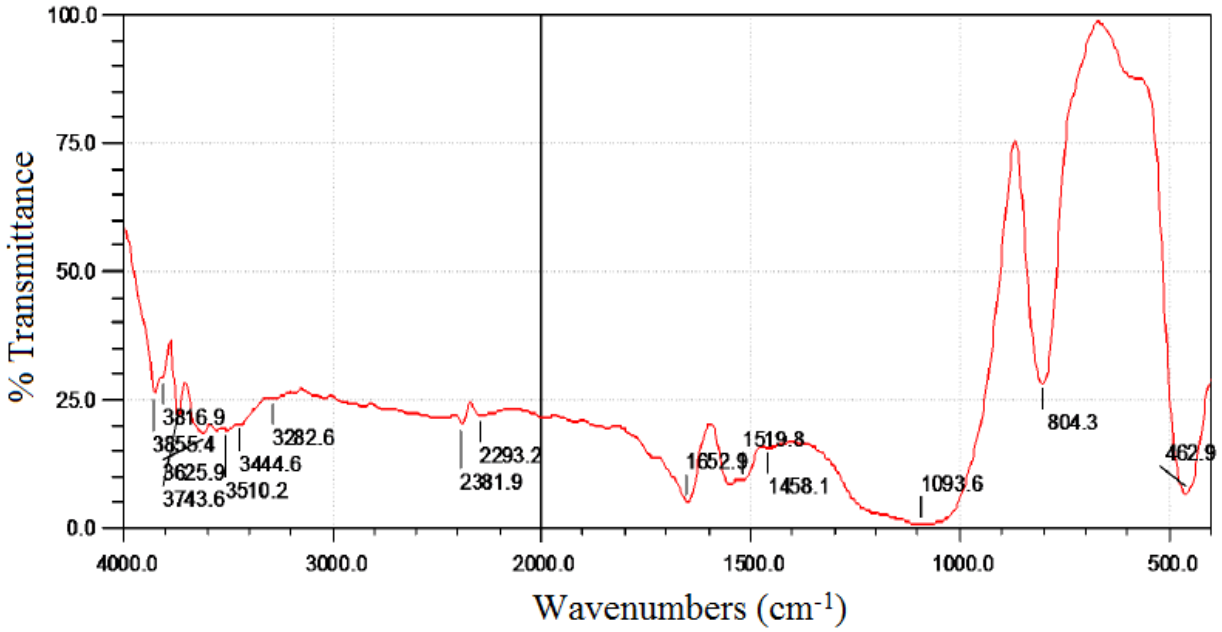


### Appendix IB: FTIR Spectrum of Pre-treated Rice Husks Ash Prepared at 600 °C

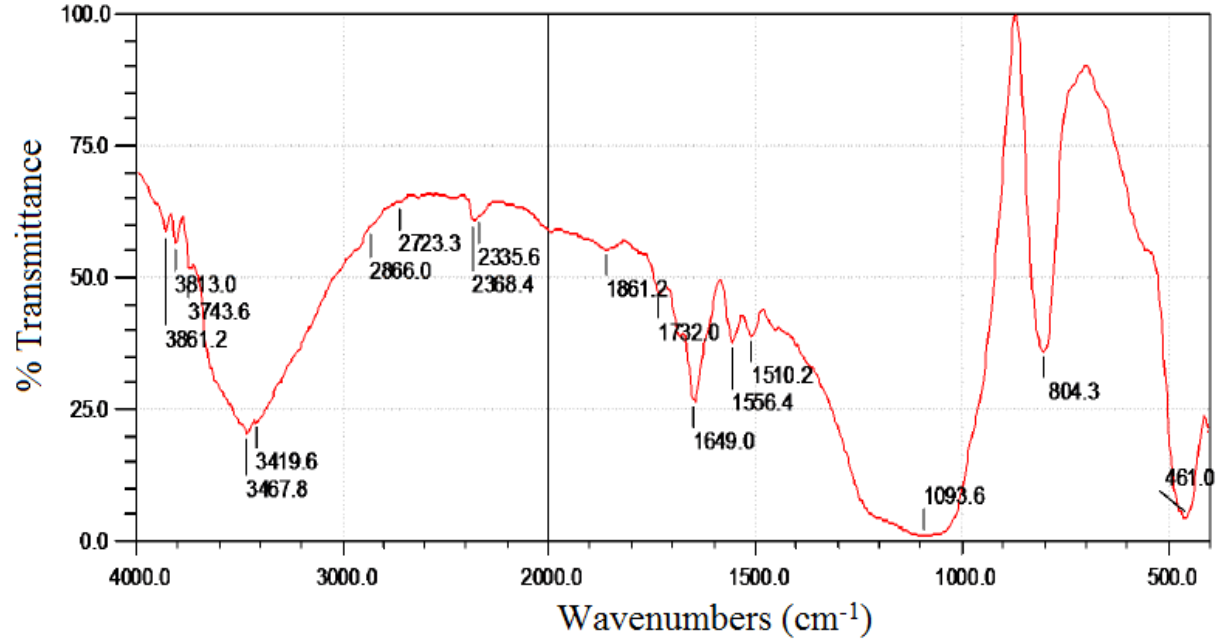

**Appendix IC: FTIR Spectrum of Pre-treated Rice Husks Ash Prepared at 700 °C**

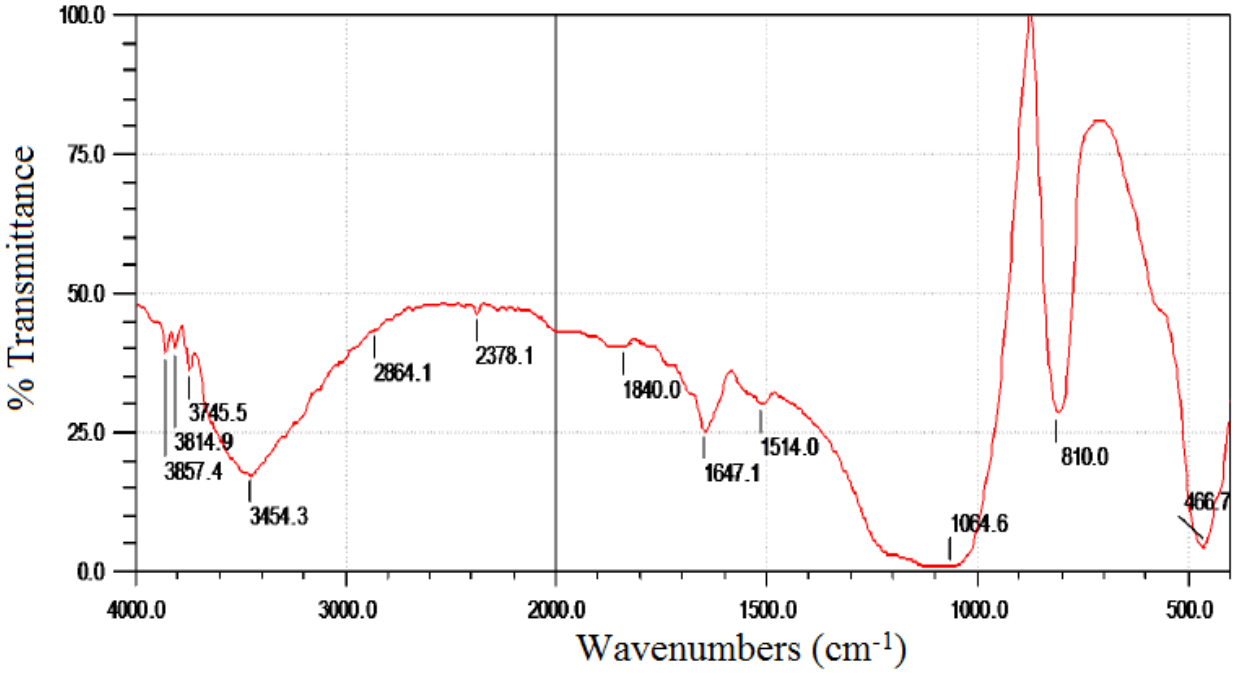


**Appendix ID: FTIR Spectrum of Pre-treated Rice Husks Ash Prepared at 800 °C**

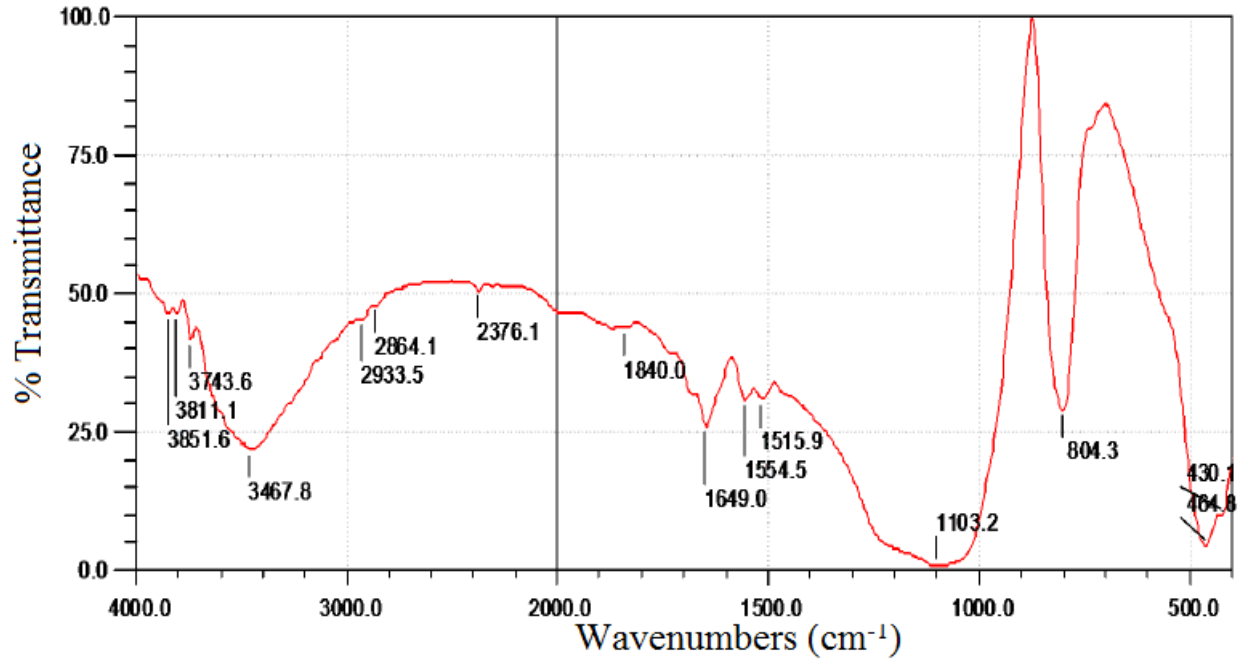

**Appendix IE: FTIR Spectrum of Pre-treated Rice Husks Ash Prepared at 900 °C**

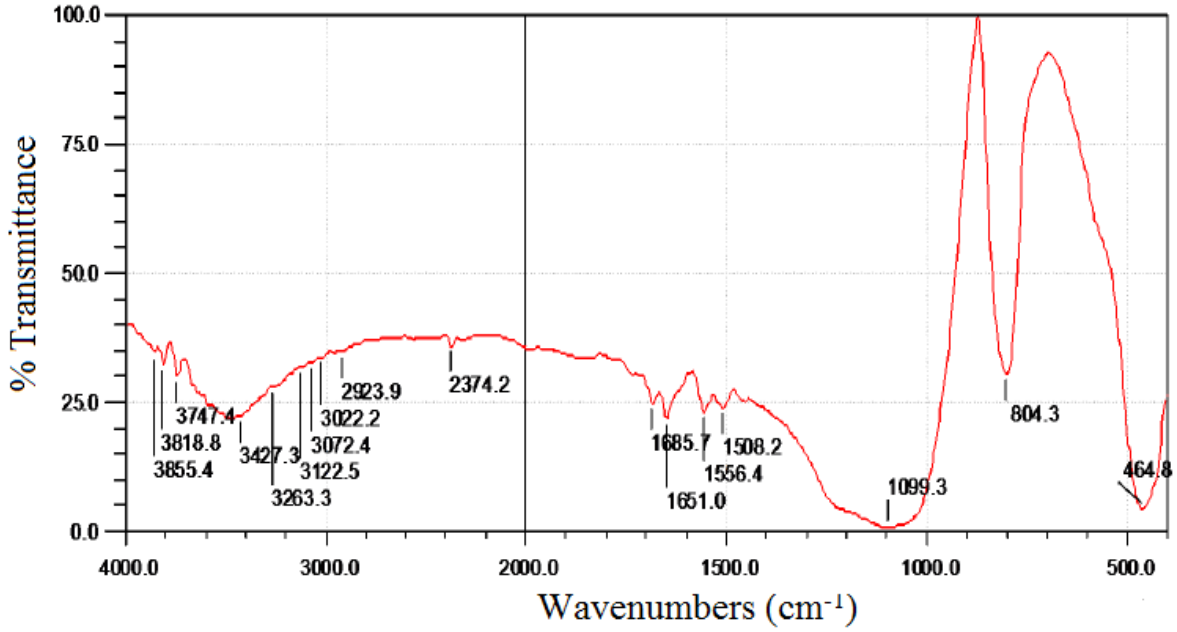


**Appendix IF: FTIR Spectrum of Pre-treated Rice Husks Ash Prepared at 1000 °C**

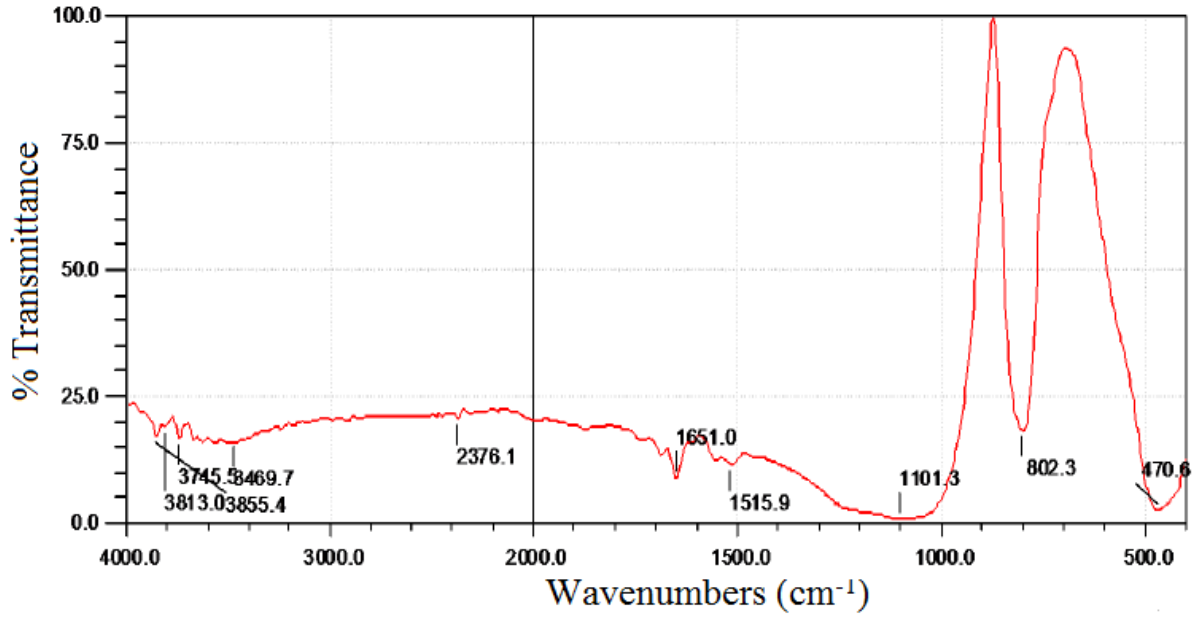

**APPENDIX II: E.D.X SPECTROMETER (SHIMADZU 800HS MODEL)**

**APPENDIX III: FOURIER TRANSFORM INFRARED SPECTROPHOTOMETER (SHIMADZU FTIR-8400S MODEL)**

**APPENDIX IV: X-RAY DIFFRACTOMETER (PHILIPS X'PERT (40kV, 30mA))**

**APPENDIX V: SCANNING ELECTRON MICROSCOPE (SHIMADZU SSX-550 MODEL)**


**APPENDIX VI: MODIFIED CLOSED REACTOR.**

## APPENDIX VII: NEWARE MULTI-CHANNEL BATTERY TESTER.

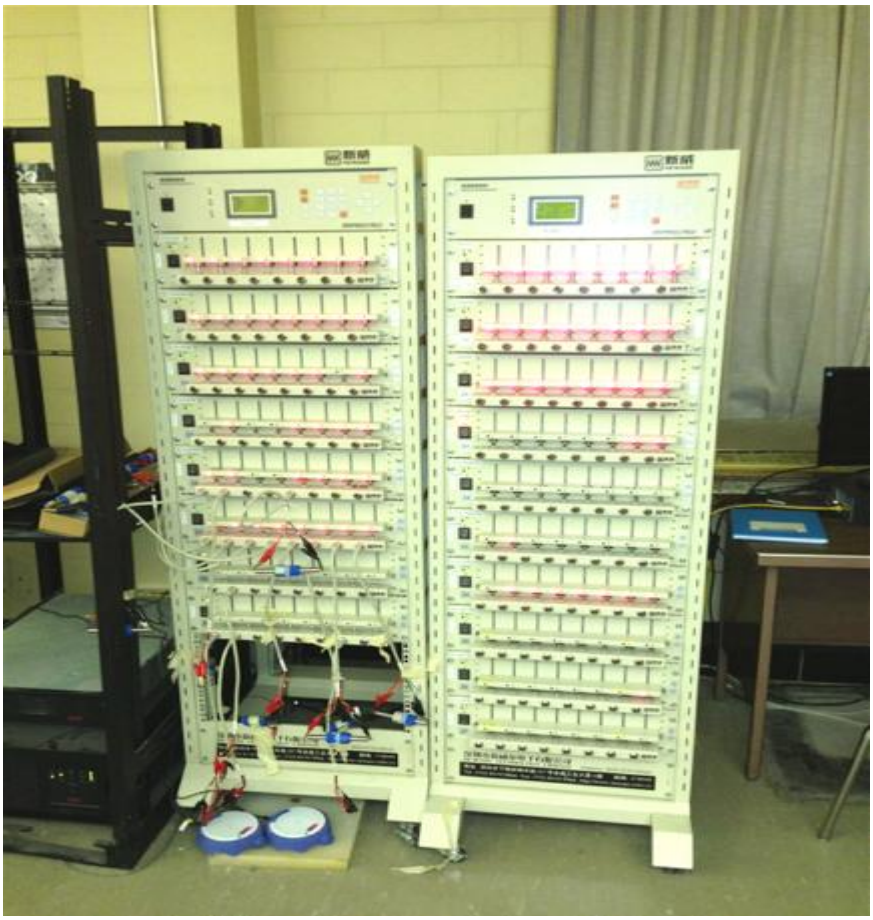

## APPENDIX VIII: BIOLOGIC VMP3 ELECTROCHEMISTRY WORKSTATION.